

# UC Santa Cruz

## UC Santa Cruz Electronic Theses and Dissertations

### Title

Investigation of the Role of Trap States in Solar Cell Reliability using Photothermal Deflection Spectroscopy

### Permalink

<https://escholarship.org/uc/item/1759m7mv>

### Author

Bezryadina, Anna Sergeevna

### Publication Date

2012

Peer reviewed|Thesis/dissertation

UNIVERSITY OF CALIFORNIA  
SANTA CRUZ

**INVESTIGATION OF THE ROLE OF THE TRAP STATES IN SOLAR  
CELL RELIABILITY USING PHOTOTHERMAL DEFLECTION  
SPECTROSCOPY**

A dissertation submitted in partial satisfaction  
of the requirements for the degree of

DOCTOR OF PHILOSOPHY

in

PHYSICS

by

**Anna Sergeyevna Bezryadina**

March 2012

The Dissertation of Anna Sergeyevna Bezryadina  
is approved:

---

Professor Sue A. Carter, Chair

---

Professor Glenn B. Alers

---

Professor Gey-Hong Gweon

---

Professor Zhigang Chen

---

Tyrus Miller  
Vice Provost and Dean of Graduate Studies

Copyright © by  
Anna S. Bezryadina  
2012

## TABLE OF CONTENTS

	Page
LIST OF FIGURES .....	vi
LIST OF TABLES .....	xi
ABSTRACT .....	xii
DEDICATION .....	xiii
ACKNOWLEDGMENTS .....	xiv
CHAPTER 1: INTRODUCTION TO PHOTOVOLTAICS.....	1
1.1. Motivation for Solar Energy .....	2
1.2. Advantages and Cost of Photovoltaics .....	3
1.3 Photovoltaics' Materials and Efficiency.....	6
1.4. Photovoltaic's Properties and Characterization.....	9
1.5. Degradation and Reliability of PV materials.....	15
1.6. References.....	20
CHAPTER 2: PHOTOTHERMAL DEFLECTION SPECTROSCOPY AND OPTICAL ABSORPTION.....	22
2.1. Photothermal Deflection Principle .....	23
2.2. Photothermal Deflection Spectrometer (PDS) Setup and Method .....	26

2.3. Optical Absorption in Thin Films.....	30
2.3.1. Band gap Absorption Region.....	32
2.3.2. Mid-gap Region .....	34
2.3.3. Band-tail Region .....	37
2.4. References.....	38
CHAPTER 3: SILICON SOLAR CELL .....	40
3.1. Background Information on Crystal Silicon, Amorphous Silicon, and Microcrystalline Silicon.....	41
3.2. Absorption of Silicon Films .....	45
3.3. Silicon Crystallinity Impact on Microcrystalline Silicone .....	52
3.4. Staebler-Wronski Effect in Amorphous Silicon Films.....	55
3.5. Staebler-Wronski effect in Different Types of Silicon Films.....	60
3.6. Impact of Al:Zn:O Layer .....	61
3.7. References.....	63
CHAPTER 4: NANOPARTICLES SOLAR CELLS .....	65
4.1. Introduction.....	66
4.2. Cadmium Telluride Nanoparticles Solar Cells .....	68
4.2.1. Background Information.....	68
4.2.2. Film Preparation .....	69
4.2.3. Sintering Effect on Absorption and Trap States of CdTe.....	70
4.2.4. CdTe Device Performance.....	73
4.2.5. Charge-Extraction Method to Find Trap States of CdTe.....	75

4.2.6. Ligands Effect to Prevent Light Induced Degradation .....	76
4.2.7. Conclusion .....	78
4.3. Lead Sulfide Nanoparticles Solar Cells .....	78
4.3.1. Background Information.....	78
4.3.2. Films Preparation.....	80
4.3.3. TiO <sub>2</sub> /PbS Device Photo-Oxidation and Degradation and EDT Ligands Effect.....	82
4.3.4. Annealing Effect.....	85
4.3.5. Conclusion .....	87
4.4. References.....	87
 CHAPTER 5: ORGANIC POLYMERS SOLAR CELLS .....	 90
5.1. Introduction to Organic Photovoltaics.....	91
5.2. Sample Preparation and Experimental Setup .....	92
5.3. Spectral Absorption Analysis of Three Polymers .....	94
5.4. P3HT Thermal and Photo-Degradation .....	97
5.5. Polyfluorene Red Degradation .....	103
5.6. Air Stability of MEH-PPV, P3HT, and Polyfluorene Red.....	106
5.7. Conclusion.....	108
5.8. References.....	109
 CHAPTER 6: CONCLUSION AND FINAL THOUGHTS .....	 112

## LIST OF FIGURES

Figure	Page
Figure 1.1: Map of world solar energy potential. ....	3
Figure 1.2: Solarbuzz retail module price index. ....	5
Figure 1.3: Plot of best research solar cell efficiencies for various photovoltaic technologies 1976-2011, compiled by the NREL National Center for Photovoltaics and last revised 9/1/2011. ....	8
Figure 1.4: Exciton splitting and resulting transport in polymer-based photovoltaics. ....	11
Figure 1.5: A simple equivalent circuit diagram for a photovoltaic device. ....	12
Figure 1.6: Current-voltage (I-V) characteristics of photovoltaic device. ....	13
Figure 2.1: Photothermal Deflection principle. ....	23
Figure 2.2: Setup of Photothermal Deflection Spectrometer. ....	27
Figure 2.3: Photos of experimental setup of photothermal deflection spectrometer. ....	29
Figure 2.4: Graph with three region of absorption: A) Band gap absorption region B) Mid-gap region C) Band-tail region. ....	31
Figure 2.5: Diagram of direct and indirect band gap for semiconductors. ....	33
Figure 2.6: The density of electronic states for idealized bulk semiconductor and realistic semiconductor (nanocrystal material). ....	35
Figure 3.1: Typical efficiency performance of a-Si modules as measured at the TISO in Switzerland. The amplitude of efficiency oscillates due to seasonal variation in	

temperature with steady decline in value through years. Blue crosses represent the average weekly operating efficiency. ....	43
Figure 3.2: Microcrystalline and amorphous silicon tandem solar cell from IMT (so-called “micromorph” solar cell). Scale bar is 2 $\mu\text{m}$ . ....	45
Figure 3.3: Absorption coefficient vs photon energy, of single crystalline silicon (c-Si), amorphous silicon (a-Si:H) and microcrystalline silicon ( $\mu\text{c-Si:H}$ ), as measured by PDS. ....	47
Figure 3.4: Absorption coefficient vs photon energy, of amorphous silicon (a-Si:H), microcrystalline silicon ( $\mu\text{c-Si:H}$ ) deposited on 50-200nm of a-Si seeding layer and with 50% crystalline fraction, and amorphous silicon (pa-Si:H) with Boron doping as measured by PDS. ....	48
Figure 3.5: Absorption coefficient of amorphous silicon vs energy. ....	49
Figure 3.6: Absorption coefficient for $\mu\text{c-Si}$ films with different crystallinity determined by photothermal deflection spectroscopy. Absorption coefficient of c-Si is added for comparison. ....	53
Figure 3.7: Determining fraction of crystalline Si for for micromorph films with different thickness with photothermal deflection spectroscopy. ....	55
Figure 3.8: PDS absorption coefficient for a-Si:H with different thickness before (a) and after (b) 12 hours of light induced degradation under $100\text{mW}/\text{cm}^2$ metal-halide lamp. ....	56
Figure 3.9: (a) Variation of low energy trap density $N_t$ (0.6-1.0eV) and high energy trap density vs thickness for a-Si:H measured by PDS (b) Variation of total trap states of a-Si:H vs thickness. (c) Variation of total trap states of a-Si:H vs thickness before and after 24 hours of light soaking. ....	58
Figure 3.10: (a) PDS absorption coefficient for a-Si:H, $\mu\text{c-Si:H}$ , and pa-Si films before and after 12 hours of light induced degradation. (b) Relative change in	

absorption coefficient before and after light soaking for for a-Si:H and $\mu$ c-Si:H films with 1000 nm thick. ....	61
Figure 3.11: PDS absorption coefficient for a-Si:H, $\mu$ c-Si:H, and pa-Si films before and after 12 hours of light induced degradation. ....	62
Figure 4.1: Typical dimension of QDs is located between discrete molecules and microorganisms, picture is done by K. Szendrei. ....	66
Figure 4.2: Device structure of CdTe solar cell. ....	70
Figure 4.3: (a) PDS linear graph of absorbtion vs. energy for unsintered, sintered 1 minute, 5 minutes, and 10 minutes CdTe films. (b) PDS logarithmic graph of absorption vs. energy for unsintered, sintered 1 minute, 5 minutes, and 10 minutes CdTe films. ....	71
Figure 4.4: SEM images of unsintered, 1min, 5 min, and 10 min sintered CdTe films. ....	73
Figure 4.5: J-V curves for ITO/CdTe/Al photovoltaics under AM1.5G, Solid green line is unsintered CdTe film, while dashed line is device sintered for 1 and 5 minutes at 400°C after CdCl <sub>2</sub> treatment. ....	74
Figure 4.6: Current transient response to charge extraction experiment for CdTe films with different sintering time. Total trapped charge is found by integrating transient over time. ....	76
Figure 4.7: PDS logarithmic graph of absorption vs. energy for different light soaking time of unsintered and 5 minute sintered CdTe films. ....	77
Figure 4.8: Absorption spectrum of PbS nanoparticles film with EDT ligands. It has an excitonic peak at 1030nm, the nanoparticle size ~4nm, and the band gap of 1.08eV. ....	80

Figure 4.9: (a) Schematic of the TiO <sub>2</sub> /PbS solar cell structure. (b) SEM image of the TiO <sub>2</sub> /PbS solar cell.....	81
Figure 4.10: (a) J-V characteristics for a TiO <sub>2</sub> /PbS (1.1 eV) device under 100 mW/cm <sup>2</sup> AM1.5 illumination before and after 24-h air exposure and subsequent 5 and 30-min of EDT soak. (b) EQE spectra for the corresponding device. Inset: the change in the exciton peak extracted from absorption data with air exposure time. ..	83
Figure 4.11: The photothermal deflection spectra of PbS QD film before air exposure and after 2 months air exposure, 30-min aggressive oxidation in air by light soaking in 100 mW/cm <sup>2</sup> of AM 1.5 light, followed by a subsequent 15 min of EDT soak.....	84
Figure 4.12: Absorption coefficient of PbS QDs film before and after annealing at 60°C, 120°C, and 180°C in glove box. ....	86
Figure 5.1: Molecular structure of P3HT, MEH-PPV, and PF Red (PSR) materials.	93
Figure 5.2: Absorption vs. energy of P3HT, MEH-PPV, and polyfluorene PF Red (solid line: PDS spectrum; dot line: Transmission spectrum). ....	95
Figure 5.3: PDS measurement of absorption vs. energy for P3HT thin film in the process of annealing. Not annealed fresh film (blue line), annealed for 25 minutes at 115C (dark blue dash line), additional annealing of the film for 10 min at 140C (violet double line). ....	99
Figure 5.4: Absorption vs. energy of annealed P3HT film in process of exposure to light and air. Fresh annealed film (light blue line), light soaked for 1 hour without air film (dark blue dot line), light soaked for 1 hour in air film (violet dash line), exposed to air for 360 hours in dark film (dark blue dot line). ....	101
Figure 5.5: Photo-oxidation mechanism according to Manceau paper.....	102
Figure 5.6: (a) Absorption vs. energy of PF Red in the process of exposure to air without light: initial state (red line), 2 hours in air (yellow dash line), 1 week in air (brown dot line). (b) Absorption vs. energy of PF Red in the process of light soaking	

under  $100\text{W}/\text{cm}^2$  from a metal-halide light with and without air exposure: initial state (red line), light soaked for 2 hours without air (claret dot line), light soaked for 24 hours without air (purple dash line), light soaked for 2 hours in air (orange double line). ..... 104

Figure 5.7: Proposed general degradation mechanism for fluorene containing polymers..... 105

Figure 5.8: Absorption vs. energy of P3HT (blue lines), MEH-PPV (green lines), and PF Red (red lines) in process of degradation in air without light exposure..... 107

Figure 6.1: Solar energy cartoon by HSB-Cartoon..... 112

## LIST OF TABLES

Table	Page
Table 3.1: Urbach energy of amorphous silicon (a-Si:H), microcrystalline silicon ( $\mu$ -Si: H), and amorphous silicon (pa-Si:H) with Boron doping, which are measured by PDS and have absorption graphs on Figure 3.4.....	50
Table 4.1: Summary of device performance parameters of CdTe solar cell devices discussed in this paper. ....	73

## **ABSTRACT**

Investigation of the Role of Trap States in Solar Cell Reliability using Photothermal

Deflection Spectroscopy

by

Anna Sergeevna Bezryadina

Stability and reliability of solar cells are crucial for utilizing them for solar energy technology. In this dissertation work photothermal deflection spectroscopy (PDS) technique was used to detect small absorption changes and to investigate trap density changes in three different types of solar cells in the process of light, air, and temperature induced degradation. The light-induced metastable changes in the properties of amorphous silicon and crystallinity effect in microcrystalline silicon were quantified by PDS. The effect of ligands and nanoparticle (NP) size on mid-gap trap states in NP thin films (CdTe and PbS) as it impacts on the performance during degradation were examined. Finally, several most common polymers (P3HT, MEH-PPV, and Polyfluorene Red) films absorption were compared and effect of photo-degradation and photo-oxidation on their trap states were analyzed. The PDS measurement technique is independent of scattering and permits the full band gap of the solar cells to be measured as well as the Urbach energy and the density of mid-gap trap states through analysis of the band gap and the band tail absorption. This work demonstrated that the higher amount of trap states in the material do not necessary limit the efficiency of a solar cell, since material structure, crystallinity, a particle deformation, and a polymer's decomposition may have much higher effect on the solar cells' stability and performance.

Dedicated to my dad Sergey  
to whom I finally can prove that  
a woman can be a good physicist, mom, and a woman altogether.

## ACKNOWLEDGMENTS

I want to thank the researchers in the Carter-Alers group and co-authors in my papers, who helped me with these projects. Especially, I want to recognize Chris France for providing CdTe films and their I-V measurements, Lily Yang for SEM images of CdTe film, Rebekah Graham for CdTe charge-extraction measurements, Guangmei Zhai for providing PbS films and their I-V measurements, Alison Breeze for providing PbS films, Tong Ju for helping setup PDS system, Josh Ford for helping run PDS measurements of a-Si 24 hours a day, 7 days a week, Jeremy Olson for helping me understand polymers, and others who helped me prepare films at UCSC and measure thickness with AFM. It has been an honor and a pleasure to work with all of you.

I have been lucky to meet many good colleagues during my PhD, who became my good friends. Thank you Chris France, Daryl Preece, Benjamin Balaban, and Jeremy Olson for being there for me when I needed it.

I owe my family big thanks for their support and belief in me throughout my entire life. I would not be who I am today without you. You taught me to love science from my childhood and aspirations. You have been there for me every step of the way providing me with all possible and sometimes impossible help to focus on pursuing my dream. Especially, I want to thank my mother Marina and my husband Dmitriy for taking care of my kid when I needed to stay long hours in the lab. I can always rely on you. I am really proud to be one more generation of physicists and mathematicians in our family.

I would also like to thank Dr. Zhigang Chen, my undergraduate adviser at San Francisco State University. You taught me how to be a researcher and in your laboratories I found my life passion for experimental optics.

I want to thank the Applied Materials company for financial support to build PDS system and for providing a-Si and  $\mu\text{c-Si}$  films.

More than anyone I owe thanks to my advisors, Dr. Sue Carter and Dr. Glenn Alers for the opportunity to do this research at ASL, NASA Ames Research center. You have guided me through the grad school and you did not allow me to give up when I had a kid and struggled. Thank you for being flexible when I needed it the most. Working with you has been a privilege for me.

# **CHAPTER 1:**

# **INTRODUCTION TO**

# **PHOTOVOLTAICS**



## **1.1. Motivation for Solar Energy**

The world demand for energy is growing rapidly with the increase of human population; however, the limited supply of today's main sources of energy (coal, gas, oil, nuclear) will force us to replace current power plants to alternative renewable energy sources. Currently oil and coal are still cheaper, available nearly anywhere, and are the dominant source of energy. However, fossil fuels have harmful effects on the natural balance of our planet. The CO<sub>2</sub> concentration in air is increasing faster than plants on the planet are able to absorb it, which raises levels of greenhouse gases in the atmosphere and leads to an increase in the global mean surface temperature. Worldwide, the oil price has been raised 5 times in a last decade from 20 \$/barrel to 100\$/barrel [1], favoring the introduction of various renewable energy sources, such as solar, wind-power, hydropower, biomass, and geothermal energy. These sources of energy will neither run out nor have any significant harmful effect on our environment.

The sun, arguably, has highest potential for satisfying a significant portion of worldwide energy demand as a source of renewable energy. Solar energy is more evenly distributed than many other renewable energy sources, free, and contains huge amount of energy. Blanketing just 4% of the earth desert areas with solar panels would provide enough power to meet the world's current electricity requirements [2]. However, the amount of sunlight solar panels receive varies greatly depending on geographical location, seasons, time of day, clouds, and air pollution. According to Figure 1.1 [2] Africa, Latin America, Southern North America, Australia, and

southern Asia have very high annual solar intensity. But people in Siberia in Russia or in Canada would not benefit much from this renewable energy source; no matter how efficient and low cost solar energy technology becomes. In the United States, the southwest is one of the best areas for introduction of solar technology due to the high radiant flux. According to a California Energy Commission report, if moderate efficiency (10%) solar panels were used just for commercial buildings, then at least one third of required for California energy would be generated annually [3].

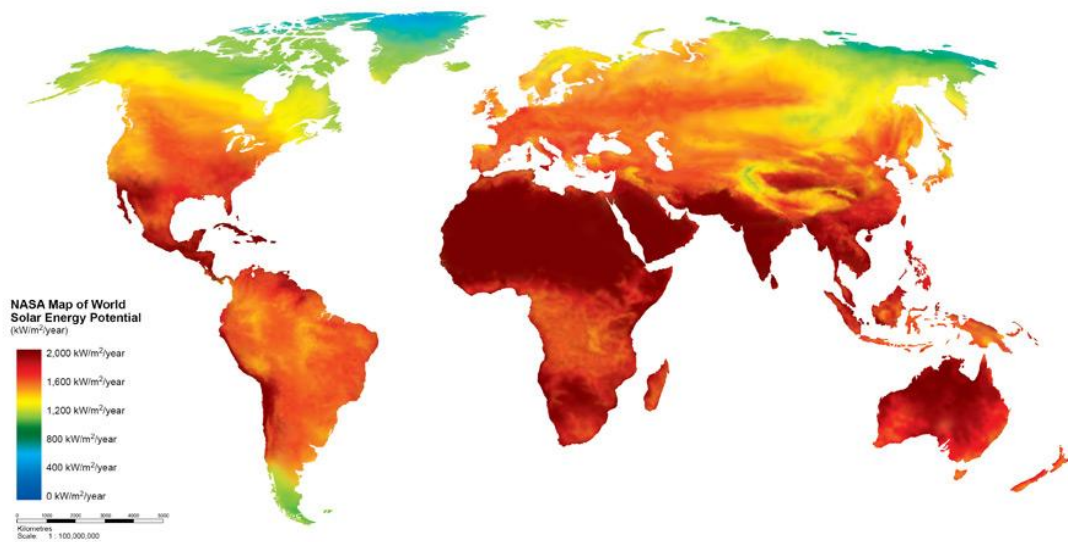


**Figure 1.1: Map of world solar energy potential.**

## **1.2. Advantages and Cost of Photovoltaics**

There are several advantages to photovoltaic solar power that makes it one of the most promising renewable energy sources in the world. First, from an environmental point of view, solar energy produces almost no carbon emissions or greenhouse gases and has no pollution. Photovoltaics don't produce toxic waste or burn oil, has no

moving parts that could break and result in an environmentally devastating accident. The only pollutants generated by solar power are created during construction and transportation of solar cells. Second, solar power can be easily mounted on the rooftop of any house as photovoltaic shingles, which saves a lot of space, protects the house, and allows maximum exposure to the sun. It requires little maintenance, no supervision, and has a life of 30 years with low costs. Isolated areas can easily produce their own supply of electricity by constructing small solar power systems. It has even advantage over wind power, hydropower since it does not necessary required turbines with moving parts, which make noise and require maintenance. Finally, sunlight will always shine upon the Earth and, as long as it does, solar power's energy supply will never run out in contrast to fossil fuels such as coal or oil. The photovoltaic cells which constitute most solar energy systems are made of silicon, one of the most common minerals found on Earth, and start to be made from other materials cheaper s to produce, or small dopants of more rare materials. That means that creating the components is relatively easy, and not material restricted, thus the overall effect on the ecosystem is reduced.

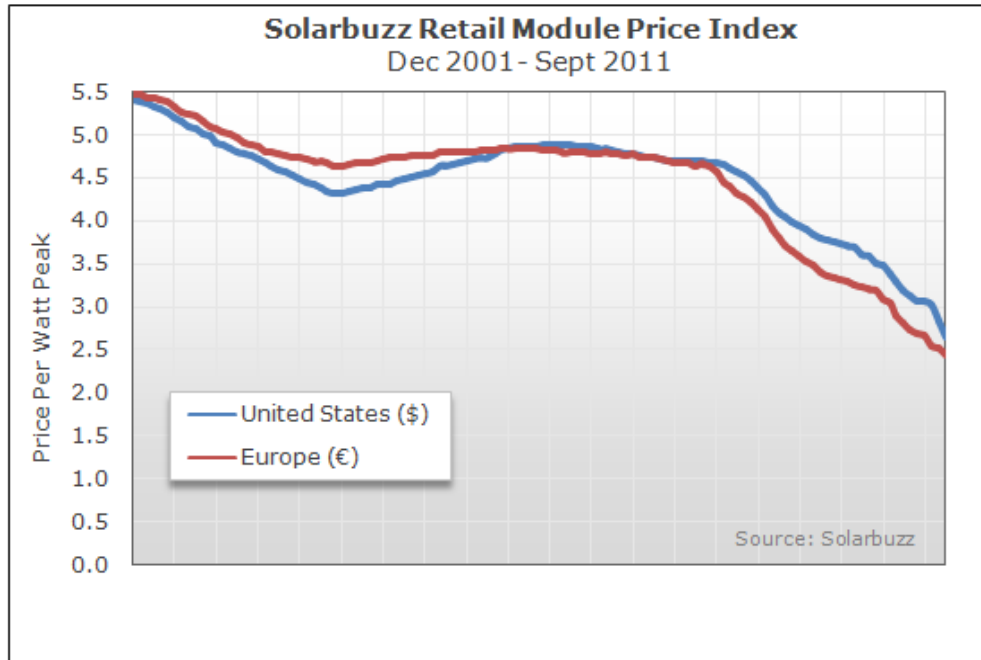


**Figure 1.2: Solarbuzz retail module price index.**

The trouble with solar energy is the cost. Currently, the average retail price of solar modules is around \$2.80/W, and factory-gate prices are in the \$1.20 - \$1.50/W range [4]. As shown in Figure 1.2 [4], retail average price dropped twice in a last decade. The efficiency of monocrystalline Si increased, new more cost efficient materials such CdTe, PbS, polymers and inorganic nanoparticles have been researched and implemented. In September 2011, the lowest retail price for a multicrystalline silicon solar module is \$1.61 per watt from a US retailer, \$1.48 per watt for monocrystalline silicon from an Asian retailer, and \$1.40 per watt for lowest thin film modules from a US-based retailer [4]. However, this price is still high and cannot compete with the cost of fossil fuel-generated electricity. The average cost per

kWh (Kilowatt Hour) of electric power in the US is \$0.12 per kWh, \$0.14 per kWh in California [5]. Photovoltaic solar panels which generate electricity directly currently cost around \$0.24 per kWh in Central and Northern California based on the cost to install the solar panels, financing the solar panels, 20 – 25 year lifespan, and an average peak sunlight hours of 4.5 hours per day [5]. After 2009 US federal and state governments have additional rebates for renewable energy, which lower the retail. With all the government rebates utility-scale solar power can now be delivered in California at prices well below \$0.10/kWh, which is lower than energy generated on low-cost natural gas. These government rebates help the solar industry to compete with the fossil fuel energy industry, and support development of new more efficient and less costly photovoltaics.

### **1.3 Photovoltaics' Materials and Efficiency**

Photovoltaics are usually categorized into three generation by their materials. First generation of solar cells (or traditional solar cells) are based on crystalline silicon (c-Si); they are usually flat-plates, have high efficiency, and currently account for more than 85% of global solar cell annual market [6,7]. The current efficiency of PV commercial wafer-based crystalline silicon models is 13-20% [6,7]. Second-generation solar cells are also called thin-film solar cells, which currently account for 10-15% of global PV model sales and subdivided in three main categories: 1) amorphous silicon (a-Si) and microcrystalline silicon ( $\mu$ c-Si) with commercial

modules efficiency 6-9%, 2) cadmium telluride (CdTe) with efficiency 9-12%, and 3) copper indium gallium selenide (CIGS) and copper indium selenide (CIS) with efficiency 10-12% [6]. Thin film solar cells are significantly cheaper, since they use few micrometers thick or less layers of semiconductor materials, but have lower efficiencies. Since their flexibility and lightweight, thin film solar cells can be rolled out onto roofs or other surfaces, or used for rooftop shingles and tiles, building facades, or the glazing for skylights.

Third-generation solar cells are cutting edge of solar technology, which generally include any extremely low-cost solar cells that do not necessary need the p-n junction as for traditional semiconductors (the Shockley-Queisser limit [8]). Currently third generation solar cells account for less than 1% of global market [6]. For simplicity of classification difference in second and third generation of solar cell largely depends on materials, which includes nanocrystals/nanoparticles solar cells, polymer-based solar cells, dye-sensitized solar cells, solar inks using conventional printing press technologies, and conductive plastics. These new PV materials are more expensive than silicon, but because less material is needed, these systems are becoming cost effective for use by industry. Also some new solar cells use luminescent solar concentrator technology to concentrate sunlight onto small area of material to increase the efficiency of photovoltaics.

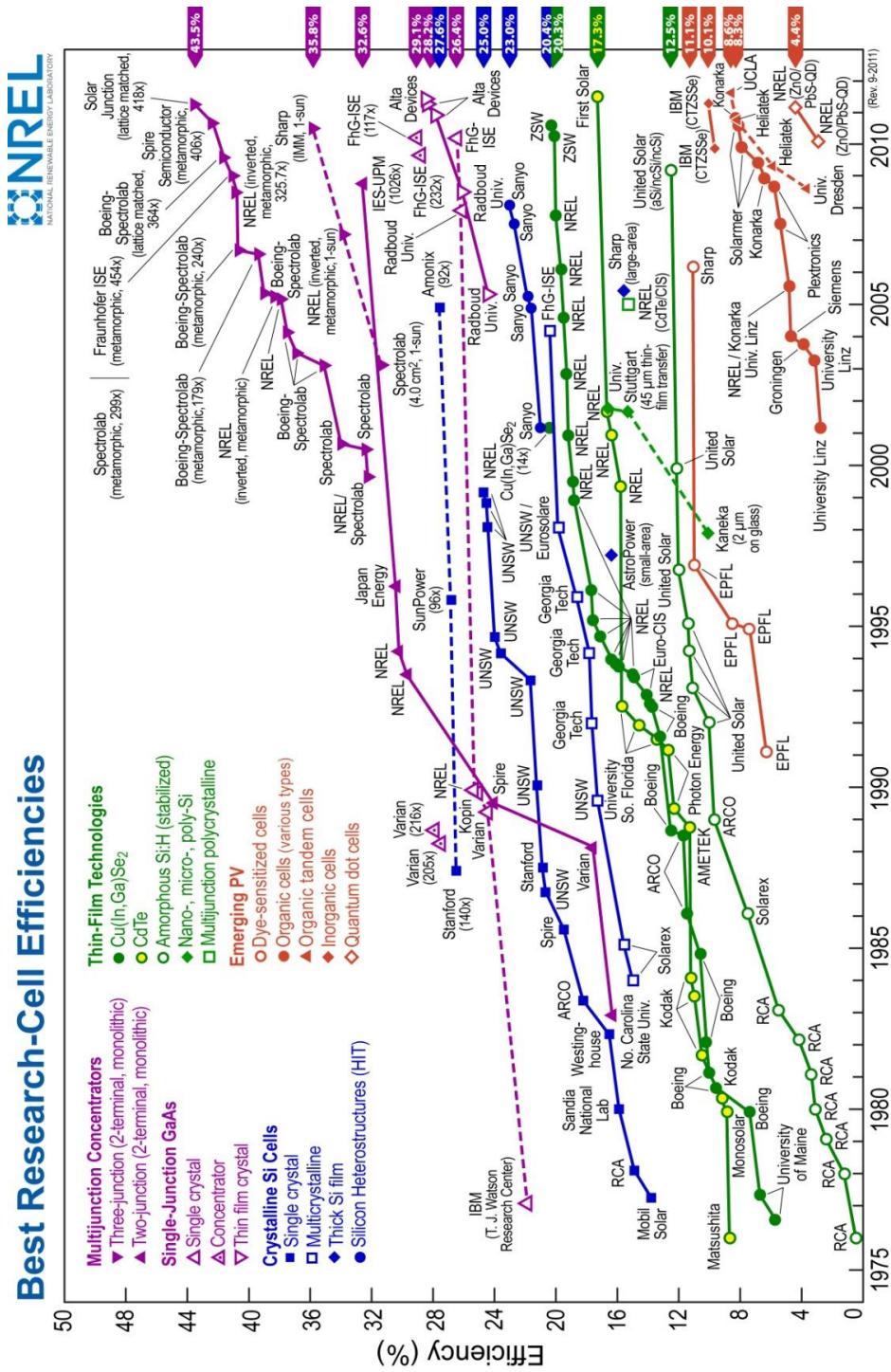


Figure 1.3: Plot of best research solar cell efficiencies for various photovoltaic technologies 1976-2011, compiled by the NREL National Center for Photovoltaics and last revised 9/1/2011.

For registration and verification of improvement of efficiency for each type of solar cells, new types of solar cells must be verified by official institutions, such as NIST or the National Renewable Energy Laboratory (NREL), among a few other qualified institutions. Variations in experimental setup for each laboratory can lead to different measurements of solar cell efficiency, so it is necessary to certify the sources of measurements for record-breaking solar cells and panels. A chart of the record efficiencies for many types of solar cells is included in Figure 1.3 [9]. The most efficient solar cell so far is a multi-junction concentrator solar cell with an efficiency of 43.5% produced by the National Renewable Energy Laboratory in April 2011. Maximum efficiencies achieved in solar cell manufacturing will always be lower than the champion efficiency because some laboratory production techniques are not reasonable on the larger scale required for mass production in the solar cell industry.

In this research, we study the optical properties of third-generation solar cells (polymer based solar cells and nanoparticles solar cells) and compare them to second generation a-Si solar cells.

#### **1.4. Photovoltaic's Properties and Characterization**

Photovoltaic (PV) cells convert solar energy (photons) into electrical energy (voltage) by PV effect. Light enters a PV cell and impart enough energy to electrons to free them; a built-in-potential barrier in the cell acts on these electrons to produce voltage, which can be used to drive a current through a circuit. The PV effect was

first reported in 1954 by Bell Lab, scientists discovered that silicon created an electric charge when exposed to sunlight [10].

The principle source of photo-voltage lies in the interface region where a built-in electrostatic field is created due to the difference in the work functions of two materials. Light incident upon the film is absorbed, promoting an electron from the valence band/HOMO (Highest Occupied Molecular Orbital) to the conduction band/LUMO (Lowest Unoccupied Molecular Orbital) and leaving a hole behind in HOMO, an attractive Coulombic interaction between the electron and hole ‘quasi-particles’ binds them into an exciton. In order to obtain charge separation – desirable in photovoltaic applications – the excitons that are formed readily by photoexcitation must reach an interface where it may be dissociated by two materials of differing electron affinity and ionization potential. This energy difference overcomes the exciton binding energy, making the charge-separated state energetically favorable. The physical size and shape of the material strongly influences the nature and dynamics of the electronic excitation. For nanoscale systems the dominant property of excitons is that the exciton size is dictated by the physical dimensions and structure of the material, but not by the electron–hole Coulomb interaction.

In a quantum confined system the exciton binding energy can be defined as a difference between the exciton transition energy (optical gap) and the electronic bandgap, where the electronic bandgap is the difference between the ionization potential and electron affinity, assuming no structural relaxation of the material or its surroundings. For inorganic bulk semiconductor materials, the polarizability and

dielectric constant are relatively large, so the electron binding energy is typically small: 27 meV for CdS, 15 meV for CdSe, 5.1 meV for InP and 4.9 meV for GaAs [11]. Since the binding energy is less than the available thermal energy, the exciton becomes unbound as soon as the photon is absorbed and free carriers result from this photon absorption. The exciton binding energy for semiconductor quantum dots (QDs), or nanocrystals of radius  $R \approx 1\text{--}2$  nm is in the range 200–50 meV, scaling approximately as  $1/R$ , according to the size dependence of the electron–hole Coulomb interaction [11]. However, polymers have a much stronger exciton binding energy of 0.2–0.6 eV, so when a photon is absorbed, the exciton remains bound [11, 12]. To overcome this binding energy, polymer-based photovoltaics need to contain more than one semiconducting materials, such as several blended polymers, as shown in Figure 1.4 [12]. Ideally, one of the blended material's LUMO and HOMO levels should be closer to vacuum than the others. With this electronic structure, charge separation occurs at the interface between the donor (the energy levels closest to vacuum) and acceptor materials.

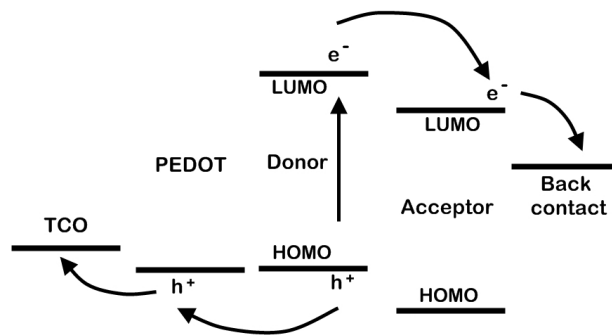


**Figure 1.4: Exciton splitting and resulting transport in polymer-based photovoltaics.**

For electrical characterization purpose, the photovoltaic device is considered as an equivalent circuit diagram as demonstrated in Figure 1.5 with a network of ideal electrical components such as diodes, current or voltage sources and resistors.

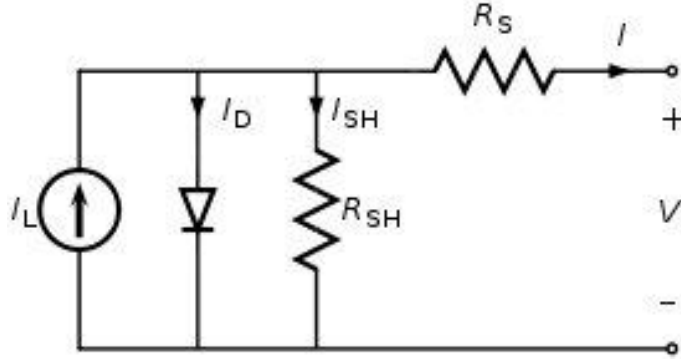


**Figure 1.5: A simple equivalent circuit diagram for a photovoltaic device.**

The current source generates current  $I_L$  upon illumination, where  $I_L$  represents number of dissociated excitons per second immediately after generation and before any recombination can take place.

The shunt resistor  $R_{sh}$  is due to recombination of charge carriers near the dissociation site (Donor/Acceptor interface).  $R_{sh}$  can be derived by taking the inverse slope around 0V:  $R_{sh} \sim (I/V)^{-1}$ , since at very small voltages the diode is not conducting and the current driven by the external voltage is only determined by  $R_{sh} + R_s$  with  $R_{sh}$  (typically) being larger at least by one order of magnitude.

The series resistor  $R_s$  considers conductivity, mobility of holes in a p-type conductor or electron in donor material. The mobility can be affected by space charges and traps or other barriers (hopping), thickness of transport layers.  $R_s$  can be estimated from the (inverse) slope at a positive voltage  $> V_{oc}$  where the I-V curves

becomes linear:  $R_s \sim (I/V)^{-1}$ , since at high positive external voltages  $V$  the diode becomes much more conducting than  $R_{sh}$  and  $R_s$  dominate the shape of the I-V curve in Figure 2.6.

The ideal diode takes into account the asymmetry of conductivity due to differences between the acceptor LUMO and the donor HOMO or the behavior of the semiconductor electrode interface in single layer cells. The diode is responsible for the nonlinear shape of the I-V curve. In ideal case, when  $R_s = 0\Omega$  and  $R_{sh} = \infty\Omega$ , the diode represents the nonlinear shape of the I-V characteristic curve of the entire cell.

On output the solar cell generates a voltage  $V$  between 0 and  $V_{oc}$  depending on the size of the load resistor. To obtain the characteristic I-V curve data in Figure 1.6 below 0V and above  $V_{oc}$ , an external voltage source is required.

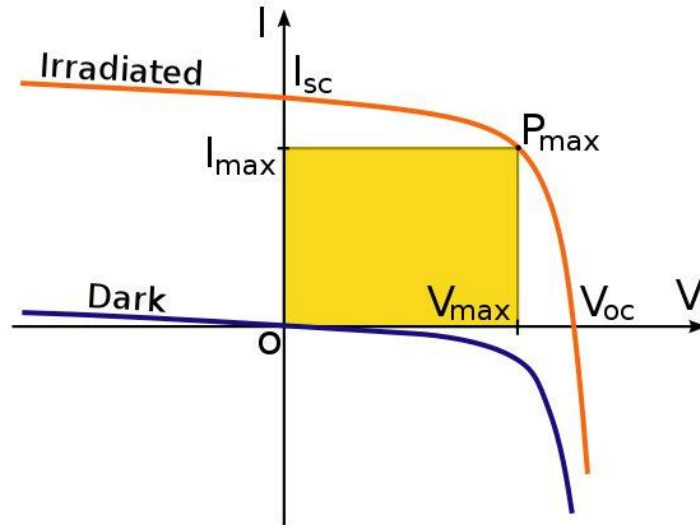


**Figure 1.6: Current-voltage (I-V) characteristics of photovoltaic device.**

A more complicated circuit diagram can be implemented to be a closer model of the current-voltage characteristics of the solar cells, but here we need only qualitative understanding for the I-V curve interpretations in Figure 1.6. The important parameters for photovoltaic performance are the open-circuit voltage ( $V_{oc}$ ) and short-circuit current ( $I_{sc}$ ), which are typically measured under a simulated Air Mass 1.5 solar spectrum (1 sun intensity, incident power density of  $100\text{mW}/\text{cm}^2$  at  $25^\circ\text{C}$ ). The maximum power of the solar cell  $P_{max}$  is the maximum product of  $J_M$  and  $V_M$ , which is a rectangular area under the curve in I-V curves in the Figure 1.6. This maximum area is larger the more the I-V curve resembles a rectangle with the area  $V_{oc} \times I_{sc}$ . The remaining photovoltaic parameter is fill-factor (FF), which is given as a percent, and corresponds to the quality of the square shape of I-V curve. Fill-factor defines the ratio of maximum available power  $P_{max}$  divided by short circuit current  $I_{sc}$  and open circuit voltage  $V_{oc}$ .

$$FF = (I_{max}V_{max}) / I_{sc}V_{oc} \quad (1.1)$$

The fill-factor is directly affected by the value of cell's series resistance  $R_s$  and shunt resistance  $R_{sh}$  in the equivalent circuit diagram. With known  $V_{oc}$ ,  $I_{sc}$ , and FF parameters, the power conversion efficiency  $\eta$  of a solar cell can be calculated as

$$\eta(\lambda) = V_{oc}(\lambda)I_{sc}(\lambda)FF(\lambda) / I_o \quad (1.2)$$

where  $I_o$  is the incident light intensity. A solar cell's energy conversion efficiency  $\eta$  represents the percentage of incident light energy that actually ends up as electric power. Increasing the shunt resistance  $R_{sh}$  and decreasing the series resistance  $R_s$  of the solar cell lead to a higher fill factor, therefore resulting in greater efficiency value,

and bringing the cell's output power closer to its theoretical maximum. In real cells power is dissipated through the resistance of the contacts and through leakage currents around the sides of the devices, which are represented by  $R_s$  and  $R_{sh}$ . Since power efficiency depends on wavelength and intensity, it is only meaningful for a given spectral distribution and intensity. So using a 1 sun intensity spectrum as illumination source is convenient.

### **1.5. Degradation and Reliability of PV materials**

Reliability of photovoltaic materials is crucial to the economic viability of photovoltaic (PV) technologies. PV reliability and degradation tests help to reduce cost of future solar cells by providing information to PV companies, which they need to improve PV product lifetime, long-term performance and decrease operation and maintenance costs of PV systems. For extensive studying broken and fresh cells are send to research centers such as NREL, NIST, or small internal laboratories. Broken cells are studied for hot-spot breakdown and parametric degradation. Fresh cells and PV materials are subjected to stressors such as thermal cycling, heat, moisture, and ultraviolet light to provide early indication of potential failure modes. By defining major degradation mechanism for different PV materials, the PV companies can eliminate degradation process and ensure stability.

Different solar cells must be protected from different type of degradations caused by stresses and effects such as:

- corrosion of materials, especially metals

- water-vapor intrusion
- delamination of encapsulate materials, especially polymers
- physical damage from wind, hail, and installation
- thermal excursions, including coefficient of thermal expansion mismatches
- ultraviolet (UV) radiation
- deterioration of or damage to external components such as junction boxes, wiring, and frames [13].

Good encapsulation of solar cells can fulfill lifetime achievement requirements for some market applications, but this encapsulation requires glass substrates or multilayer coating barrier. However, glass shield will reduce flexibility of new generation of solar cells and significantly increase fabrication costs and weight. Since minimizing PV module cost is essential, the degree of protection from degradation will be imperfect, and trade-off between cost and protection must be found. Typically, the costs of the materials used for protecting the internal solar cells (packaging costs) are roughly 50% of the total materials cost [13]. Consequently, understanding stability and reliability of photovoltaics is an important issue on which efforts should be focused. This work carries out understanding of light-induced and air-induced degradation of PV materials from fundamental knowledge and also for developing devices that are resistant to these degradation processes.

One of the first light-induced degradation effects for PV materials was reported and analyzed by Staebler and Wronski in 1977, shortly after the development of the first solar cells based on hydrogenated amorphous silicon (a-

Si:H) in 1976 [14]. By this Staebler–Wronski Effect (SWE) a-Si:H material undergoes light-induced metastable changes. Under light exposure the defect density of a-Si:H increases, which causes an increase in the recombination current and leads to drop off conversion efficiency. Also the photoconductivity and dark conductivity of hydrogenated amorphous silicon (a-Si:H) decreases up to 4 orders of magnitude under prolong intense light illumination. However, annealing a-Si:H sample above 150°C reverses effect and recovers it to original state [14, 15]. Many observations show that this induced degradation effect occurs in the bulk of the films, and is associated with changes in defect density or occupation of deep gap states, which act as recombination centers for photoexcited carriers and lead to a shift of the dark Fermi level toward mid gap.

The specific mechanism of Staebler–Wronski effect by which light can introduce gap states is still not well understood, but several models were proposed. The most common model has been the hydrogen bond switching model by Stutzmann [16], which proposes that photoexcited electrons and holes recombine at weak Si–Si bond locations, that concomitant non-radiative energy release is sufficient to break the bond, and that a back-bonded H atom prevents restoration of the broken bond by a bond switching event, leaving dangling bond. Another model is the charge transfer model by Adler[17], that suggests that preexisting at equilibrium spineless charged centers (positively and negatively charged dangling bonds) are transformed to neutral dangling bonds by capture of excess free carriers, thus reducing the current that can pass through. More recently, Branz suggested the hydrogen collision model of light-

induced metastability in aSi:H [18], which can explain many aspects of the Staebler–Wronski effect that the previous models could not. According to this model, nonradiative recombination of photogenerated carriers excite mobile hydrogen atoms from Si–H bonds leaving behind two dangling bonds. These mobile hydrogen atoms move around in the material and a metastable defect is formed when two mobile hydrogens collide and associate in a metastable two-hydrogen complex.

A similar effect of light induced degradation exists in other types of photovoltaic materials. In nanoparticle semiconductor materials quantum dots are bound with ligands to their surface, which determine the solubility or miscibility in a particular medium, and also mediate energy and charge transfer with the surrounding environment. The ligands are very effective in passivating surface defects and traps; however, the passivation effect is not stable to UV light exposure in air or to high temperature stress. The photo-oxidation and high temperature degradation of ligands result the gradual erosion of the nanoparticle-pyridine surface and the increase in trap states of the NPs, which causes performance degradation of semiconductor devices including optical efficiency and leakage current.

Organic or polymer photovoltaic devices have a broader range of degradations: chemical and physical degradation, during illumination and in the dark, with air and without air exposure. With physical degradation the morphology of the cell changes, since the structure of polymers is not static once it has been formed during production of the device [19]. For example, the donor and acceptor components in a bulk heterojunction structure segregate over time. These gradual

changes in the microstructure will lead to degradation in the performance of the cell. Chemical degradation of polymer photovoltaics mainly focuses on the role of oxygen, water and electrode material reactions with the active polymer layer with and without illumination. For organic photovoltaics photo-degradation usually occurs much faster in the presence of oxygen than in an oxygen-free environment. No-air light illumination, especially UV light, leads to the breaking of chemical bonds in a polymer with the removal of one or more electrons. During photo-oxidation traps are generated through the presence of oxygen in the polymer material and cause a slow down of recombination. As a result, the short-circuit current density ( $J_{SC}$ ) decreases due to a reduction in charge-carrier mobility, while the device open-circuit voltage ( $V_{OC}$ ) remains almost unchanged, which leads to the performance degradation of polymer based solar-cell [20]. Most polymers also experience a photobleaching effect, the photochemical destruction of the chromophores responsible for the color of the polymers, which results in reduction of the optical absorption. The magnitude of this photobleaching effect varies for different materials, but alone it is insufficient to explain the loss in the photocurrent and decreased efficiency of the device [20]. For conjugated polymers the generally accepted model of the photobleaching effect is a formation of a charge transfer complex of polymers in air, where the conjugated polymer acts as an electron donor and the oxygen acts as an electron acceptor [21].

All these different photovoltaic materials have similar mechanism of degradation: high density mid gap traps leads to higher recombination currents. Photodegradation is slowed down by encapsulation of solar cells: by operating them

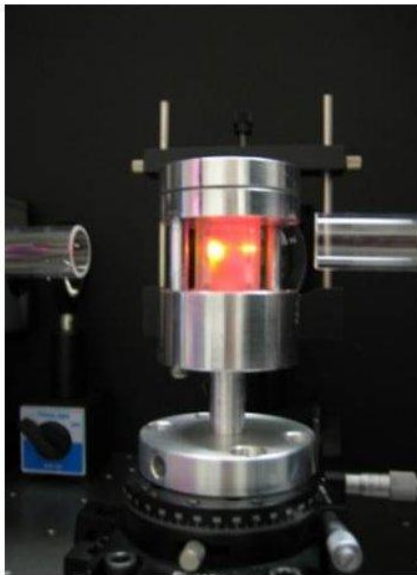
in inert atmospheres, or, for some materials, by covering them with aluminum top electrodes. By using the Photothermal deflection spectroscopy method, which is discussed in next chapters, we can measure very precisely changes in the mid-gap trap states and analyze and quantify the degradation mechanisms of solar cells.

## 1.6. References

- 1) B. Büyükşahin and M. A. Robe, “Does “Paper Oil” Matter? Energy Markets’ Financialization and Equity-Commodity Co-Movements,” U.S. Energy Information Administration (2011).
- 2) Clean Energy, “NASA World Map for Solar Potential,” <http://www.cleaner-energy.com.au/ce/solar-info/energy-from-the-sun>, accessed 10/10/2011.
- 3) G. Simons and J. McCabe, California solar resources. Technical Report CEC-500-2005-072-D, California Energy Commission, Sacramento, California (2005).
- 4) Solar Market Research and Analysis, “Module Price, Retail Price Summary - September 2011 Update,” <http://solarbuzz.com/facts-and-figures/retail-price-environment/module-prices>, accessed 10/11/2011.
- 5) Smart Energy Policy Blog, “Solar Energy Panels in the Home,” <http://smartenergypolicy.wordpress.com/2011/02/08/solar-energy-panels-in-the-home/>, accessed 10/11/2011.
- 6) P. Frankl, S. Nowak, M. Gutschner, S. Gnos, and T. Rinke, “Technology Roadmaps. Solar photovoltaic energy”, IEA, (Corlet, France, 2010), pp. 1-48.
- 7) A. Goetzberger, C. Hebling, *Sol. Energ. Mat. Sol. C.* **62**, 1 (2000).

- 8) W. Shockley and H. J. Queisser, *J. Appl. Phys.* **32(3)**, 6689 (1960).
- 9) National Renewable Energy Lab for Photovoltaics, “Best Research-Cell Efficiencies,” [http://en.wikipedia.org/wiki/Solar\\_cell\\_efficiency](http://en.wikipedia.org/wiki/Solar_cell_efficiency), accessed 10/11/2011.
- 10) J. Perlin, “The Silicon Solar Cell Turns 50”, National Renewable Energy Laboratory, (2004).
- 11) G. Scholes, G. Rumbles, *Nat. Mater.* **5**, 683 (2006).
- 12) J. Olson, “Novel photovoltaics: an introduction to basic characterization” (UC Santa Cruz, USA, 2009), pp. 1-27.
- 13) C. R. Osterwald and T. J. McMahon, *Prog. Photovolt: Res. Appl.* **17**, 11 (2009).
- 14) D. L. Staebler and C. R. Wronski, *Appl. Phys. Lett.* **31(4)**, 15 (1977).
- 15) D. L. Staebler and C. R. Wronski, *J. Appl. Phys.* **51**, 3262 (1980).
- 16) M. Stutzmarin, W. B. Jackson, and C. C. Tsai, *Phys. Rev. B* **32**, 23 (1985).
- 17) D. Adler, *Sol. Cells* **9**, 133 (1983).
- 18) H. M. Branz, *Phys. Rev. B* **60**, 7725 (1999).
- 19) M. Jørgensen, K. Norrman, F. C. Krebs, *Sol. Energ. Mat. Sol. C.* **92**, 686 (2008).
- 20) R. Pacios, A. J. Chatten, K. Kawano, J. R. Durrant, D. D. C. Bradley, and J. Nelson, *Adv. Funct. Mater.* **16**, 2117 (2006).
- 21) W. Lee, H. Park, and G. Kwak, *Chem. Commun.* **47**, 659 (2011).

# **CHAPTER 2: PHOTOTHERMAL DEFLECTION SPECTROSCOPY AND OPTICAL ABSORPTION**



## 2.1. Photothermal Deflection Principle

It is commonly known that with the absorption of electromagnetic radiation by a given medium, a fraction of or most of the excitation energy will be converted to thermal energy. The basic mechanism of Photothermal Deflection Spectroscopy (PDS) is the deflection of light beam when it passes through a refractive index gradient created due to a temperature gradient. A modulated monochromatic pump beam is sent into given medium (sample), the absorbed optical energy creates thermal diffusion wave inside the sample, as shown in Figure 2.1. This optically generated thermal oscillation penetrates the surrounding medium within a thermal diffusion length and causes a modulated change of the index of refraction right above the optically pumped region. A probe laser beam traveling parallel to the surface will be deflected harmonically due to the gradient of the refractive index and this phenomenon is known as the mirage effect or photothermal deflection. The amplitude and phase of the beam's deflection carry information about the optical and thermophysical properties of the absorption of the sample.

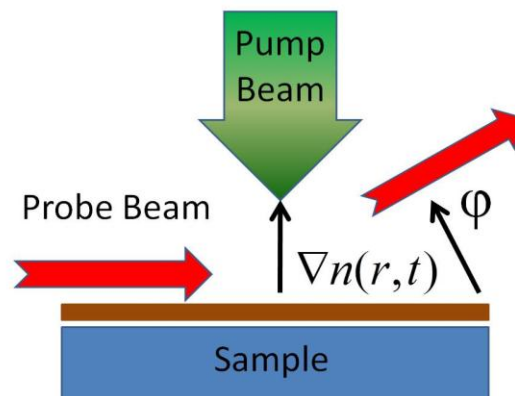


Figure 2.1: Photothermal Deflection principle.

The first time “mirage effect” was introduced in 1980 in a paper by Boccara [1], in which the absorption coefficient of the sample was deduced from the measurement of the thermal gradient in the gas layer adjacent to the sample surface. In this experiment a condensed phase sample was periodically irradiated by a beam of monochromatic light, which caused a periodic change of temperature on the surface of the sample. There was seen to be a quick change in temperature, going from surface to gas. This periodic temperature gradient gave rise to a refractive index gradient, and resulted in periodic deflection of a probe beam propagating along the surface of the solid sample [1].

Using diffraction theory, general expressions for the deflection of a laser beam by an absorbing medium on a given substrate was derived [2]. In this derivation the effects of the substrate are neglected and consider the case in which the thermal diffusion length of the medium is much smaller than the Gaussian pump-beam radius, then the deflection angle  $\varphi$  is

$$\varphi = \frac{dn}{dT} \frac{P}{pc\omega\pi^2 a^2} [1 - \exp(-\alpha l)] \times \left[ -2 \frac{x_0}{a^2} \exp\left(-\frac{x_0^2}{a^2}\right) \right] \quad (2.1)$$

where  $dn/dT$  is the temperature coefficient of the index of refraction of the medium,  $P$  is the incident monochromatic beam power,  $\omega$  is the modulation frequency of the pump beam,  $pc$  is the heat capacity per unit volume,  $a$  is the radius of the pump beam at  $1/e$  intensity,  $x_0$  is the separation between the intensity maxima of the pump and probe beams,  $\alpha$  is the optical absorption coefficient, and  $l$  is the optical path length in the absorbing medium. Thus, for small  $\alpha l$ , the deflection amplitude is proportional to the optical absorption and to the power while inversely proportional

to the modulation frequency. Furthermore,  $\varphi$  exhibits a maximum near  $x_0/a \sim 1$ , defining the optical separation between the pump and probe beams [2].

On the other hand, in the case in which the thermal diffusion length is much larger than the pump beam radius,  $\varphi$  is given by

$$\varphi = \frac{dn}{dT} \frac{P}{\kappa \pi^2 x_0} [1 - \exp(-\alpha l)] \times \left[ 1 - \exp\left(-\frac{x_0^2}{a^2}\right) \right] \quad (2.2)$$

where  $\kappa$  is the thermal conductivity of the medium. Note that in this regime,  $\varphi$  is independent of modulated frequency  $\omega$  [2]. In the experiment the deflection can be as small as  $10^{-9}$ - $10^{-10}$  rad and still be well within the detection levels of available position sensors. The amplitude of the deflection is related to the optical absorption in a straightforward manner.

PDS system becomes an important highly sensitive nondestructive tool for ultralow absorption study in both films and bulk semiconductor materials. This photothermal deflection principle can be used for surface, as well as transparent sample analysis. For surface analysis, the probe laser beam is used to detect a refractive index gradient formed in the media above the surface. In transparent samples, the refractive index is changed within the sample itself. To study these transparent samples excitation pump beam and probe laser beam need to propagate collinear through the sample. Then the deflection angle signal is basically the same as the pulsed laser photothermal lens inverse focal length [3, 4]. This photothermal deflection method for transparent samples is very similar to photothermal lens spectroscopy, where both methods rely on the generation of a refractive index

gradient in the sample itself. Collectively, they have become known as refractive index gradient detection or photothermal refraction spectroscopy methods.

## **2.2. Photothermal Deflection Spectrometer (PDS) Setup and Method**

The experimental apparatus used in PDS measurement is shown in the Figure 2.2 and 2.3 and discussed in several papers [5-8]. The pump beam, provided by 250 W halogen lamp, is chopped at 10Hz to produce a time-dependent signal and sent through monochromator. Before monochromator we have filter wheel with 5 high pass filters, which cut second harmonics (Figure 2.3(a)). Part of monochromatic beam is sent to pyroelectric detector for reference and normalization purpose. The second part of the beam is focused perpendicularly to the sample inside of container (Figure 2.3(b)).

The PDS measurements require films on glass with no Al contacts or ITO layer. Samples for PDS can be cut from regions of working devices that had no Al or ITO pattern or prepared separately for absorption measurements. The sample is immersed in a quartz container with an electrolyte liquid ( $\text{CCl}_4$  or  $\text{C}_6\text{F}_{14}$ ), a liquid with a highly temperature-dependant refractive index. To find the best suited electrolyte liquid for PDS measurements, we need to look on two parameters: it does not dissolve film material and it has the strongest dependence of refractive index temperature coefficient on the thermal expansivity, which can be found in a table of Murphy paper [9].

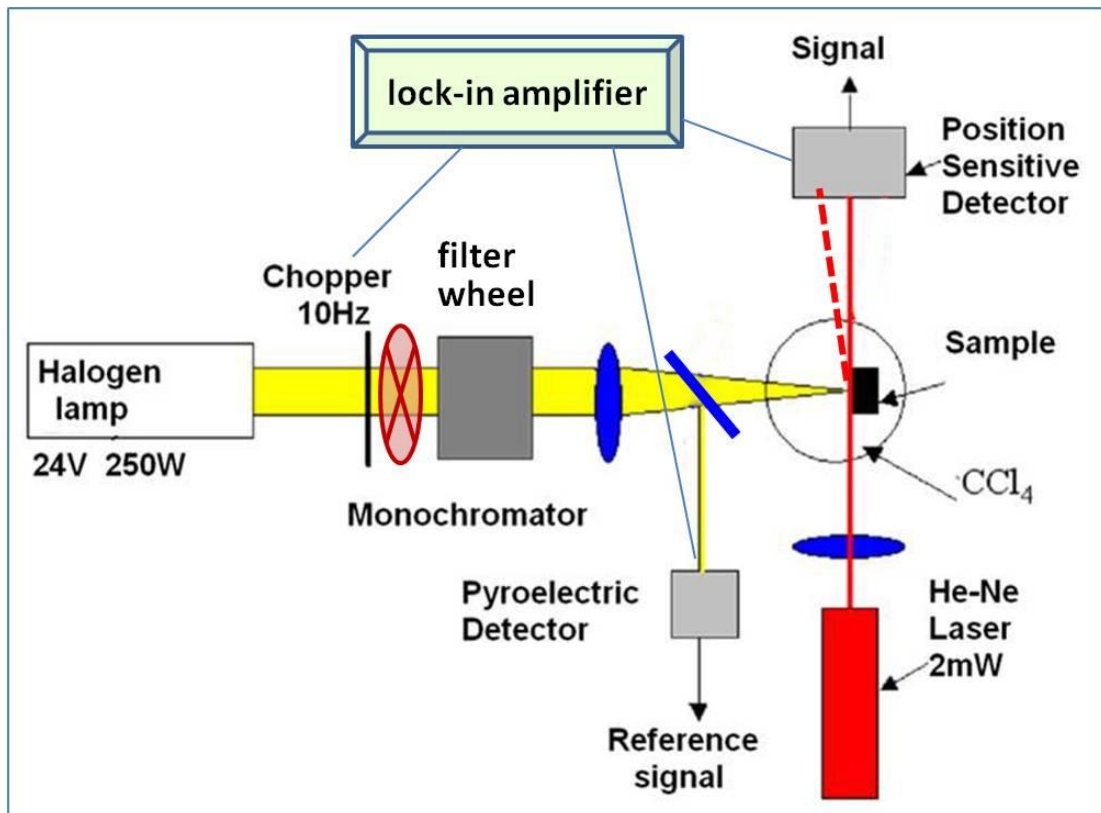


Figure 2.2: Setup of Photothermal Deflection Spectrometer.

As the sample absorbs incident radiation of a monochromatic beam, non-radiative recombination processes cause the sample to heat the adjoining electrolyte solution and generate a temperature gradient in the space close to the sample surface, which is accompanied by a gradient of the index of refraction. The probing beam from the 2mW He-Ne laser is focused nearby sample deflecting media and aligned parallel to the surface of the sample (Figure 2.3(c)). As a result, a monochromatic chopped pump beam produces a time-dependent refractive index variation profile in the direction normal to the sample surface, and the He-Ne probe deflects and oscillates in the tangential direction to the sample surface. For numerical calculation

the Boccard equation (2.1) can be simplified and the beam deflection can be written as

$$\varphi \propto a \frac{\Delta T}{\Delta x} \frac{dn}{dT} \quad (2.3)$$

where  $a$  is proportional to pump area,  $dn/dT$  is the thermal gradient of electrolyte liquid,  $\Delta T$  is the temperature difference between the sample surface and the bulk of the electrolyte, and  $\Delta x$  is approximately one thermal diffusion length in the electrolyte at the chosen modulation frequency [7].

This beam deflection is monitored by a position sensitive detector and normalized by the incident light intensity as measured by a pyroelectric detector (Figure 2.3(c)). The data from detectors passes through lock-in amplifiers to reduce noise. A lock-in amplifier is used to filter one specific frequency from an input signal, so it acts like a very accurate band pass filter. It overlays the signal with a sinusoidal reference signal from chopper wheel at the defined frequency and integrates signal over several periods. While all unwanted frequency components and background noise cancel out in the integration, the component at the frequency of the reference signal is amplified. Then the output voltage of the lock-in amplifier, which is proportional to the amplitude of the frequency oscillations, is collected and manipulated by a LabView program. To get exact values of absorptions the PDS signal is calibrated to the absorption coefficient measured by transmission spectroscopy in a band-gap region of the film. It can be determined by plotting both the PDS and the transmission/reflection data into one diagram and then adjusting the

scaling factor until both curves overlap for those energies where both methods provide accurate results.

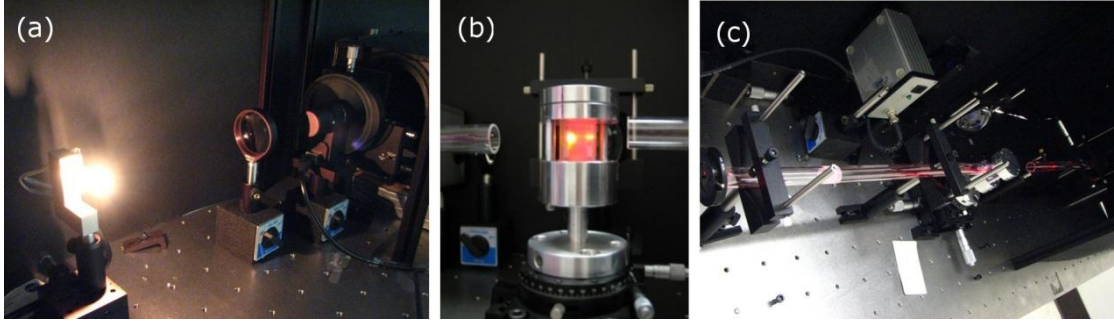


**Figure 2.3: Photos of experimental setup of photothermal deflection spectrometer.**

By Lambert and Beers laws, the intensity of light is attenuated exponentially with the propagation distance  $d$  in the absorbing material:

$$I = I_0 \exp(-\alpha d) \quad (2.4)$$

From this law we can derive absorption  $\alpha$  of a PDS sample for each frequency

$$\alpha = \frac{-1}{d} \ln\left(1 - \frac{V_{sig}}{V_{ref}} C_{norm}\right) \quad (2.5)$$

where  $d$  is a thickness of the film on a glass,  $V_{sig}$  is amplitude of signal oscillation from position sensitive detector determined by lock-in amplifier,  $V_{ref}$  is signal from pyroelectric detector, and  $C_{norm}$  is a constant for normalization absorption to transmission spectrometer.

The limiting sensitivity of a PDS measurement is typically of the order of  $\alpha d \sim 10^{-5} - 10^{-7}$  [2, 5]. Even for a very thin 10 nm sample, this sensitivity is more than sufficient to record an optical absorption signal with accuracy up to  $1 \text{ cm}^{-1}$ . The PDS system allows contactless measurements of absorption from less than  $1 \text{ cm}^{-1}$  to  $10^5$

$\text{cm}^{-1}$  over an energy range of 0.5eV to 3eV for 0.01 - 100 $\mu\text{m}$  thick films at room temperature. The PDS can measure the density of states in films, since it can detect optical absorption for photon energies less than mobility gap and can “catch” an electron lifting into and out of any level, whether it is at the surface or in the bulk of the media.

Although PDS is very accurate for low absorption, it becomes useless if  $\alpha$  gets too high. If too much light is absorbed in the sample, temperature gradients would become so steep that heat conduction can no more be neglected. This results in saturation effects on the output signal. Mandelis in his paper makes a comparison and analogy of photothermal deflection spectroscopy with more known photoacoustic spectroscopy [10]. He states that the PDS signal phase anticorrelates with the amplitude, which causes phase saturation for both very high and low values of absorption. The range of most precise absorption values within which phase exhibits sensitivity to changes in  $\alpha$  lies approximately between 10 and  $10^4 \text{ cm}^{-1}$ . So by theoretical predictions PDS can be used most successfully as a spectroscopic technique to measure absorption coefficients in the range  $10\text{cm}^{-1}$  to  $10^4\text{cm}^{-1}$  and on broader range of absorption PDS signal starts to have noise and saturation.

### **2.3. Optical Absorption in Thin Films**

Absorption of light is conversion of the energy contained in the incident photon to other form of energy, usually heat [11]. Some materials have just the right combination of properties to convert the energy of incident photons to electrical

energy. An absorbed photon interacts with an atom and gives off its energy to an electron in the material. This energy transfer is governed by the laws of the conservation of energy and momentum.

Absorption measurements are critical to understanding which portions of the optical spectrum are most important and what defect states could be limiting efficiency of devices. In common transmission spectroscopy measurements, light scattering can severely affect the absorption measurement because the absorption is usually derived indirectly from transmission (T), reflection (R), and scattering (S) which are related by energy conservation:  $1=T+R+S+A$ . For example, for polymer materials, the absorption A is usually very small, and therefore, light scattering S can make transmission measurements useless. In PDS, only the absorption A (the part which turns into heat) is directly measured and therefore, it has great sensitivity for polymer thin films and other low absorption materials.

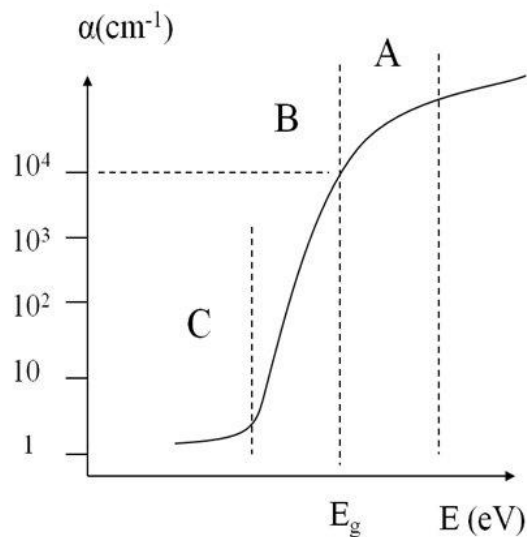


**Figure 2.4: Graph with three region of absorption: A) Band gap absorption region B) Mid-gap region C) Band-tail region.**

Photothermal deflection spectroscopy (PDS) allows investigation of the optical absorption spectrum over a range covering 4-5 decades of absorption coefficient including band gap absorption region, the mid-gap region and band-tail region of films, as shown in Figure 2.4.

### **2.3.1. Band gap Absorption Region**

For photovoltaic devices absorption above the band gap (the region A in Figure 2.4) determines the portions of solar spectrum that is converted photogenerated electrons and holes, which can either be collected or recombine internally by either radiative or non-radiative (Shockley-Read-Hall) processes. Only photons whose energy is equal to or greater than the band gap of the cell material can free an electron for an electric circuit.

From band gap absorption region of the graph one of most important absorption parameter, the band gap, can be determined. The band gap of a semiconductor material is the minimum energy needed to move an electron from its bound state within an atom to a free state, where the electron can be involved in conduction. The lower energy level of a semiconductor is called the valence band, and the higher energy level where an electron is free to ramble is called the conduction band. So the band gap (often symbolized by  $E_{gap}$  or  $E_g$ ) is defined as the energy difference between the conduction and valence bands.

In semiconductors there are two types of band gap: direct and indirect band gap, as demonstrated in Figure 2.5. In a direct band gap, the momentum of electrons

and holes is the same in the conduction and valence bands and an electron directly emits a photon. In an indirect band gap, a photon cannot be emitted, since electron cannot shift from the conduction band to the valence band without passing through an intermediate state and transferring momentum to the crystal lattice. Figure 2.5 shows that the allowed energies of a particle in the valence or conducting bands depend on particle momentum in these bands. Then the band transition of an electron requires sufficient momentum from a phonon to cause displacement along a momentum axis, which is difficult to provide due to the low photon momentum and the conservation laws of momentum and energy. So for direct band gap material, such as GaAs, CdTe, CIS, and a-Si, photons with energy near the material band gap energy are absorbed much more readily than in indirect materials, such as c-Si. As a result, the direct band gap materials can be several magnitudes thinner than indirect band gap materials and still absorb significant part of incident radiation [11].

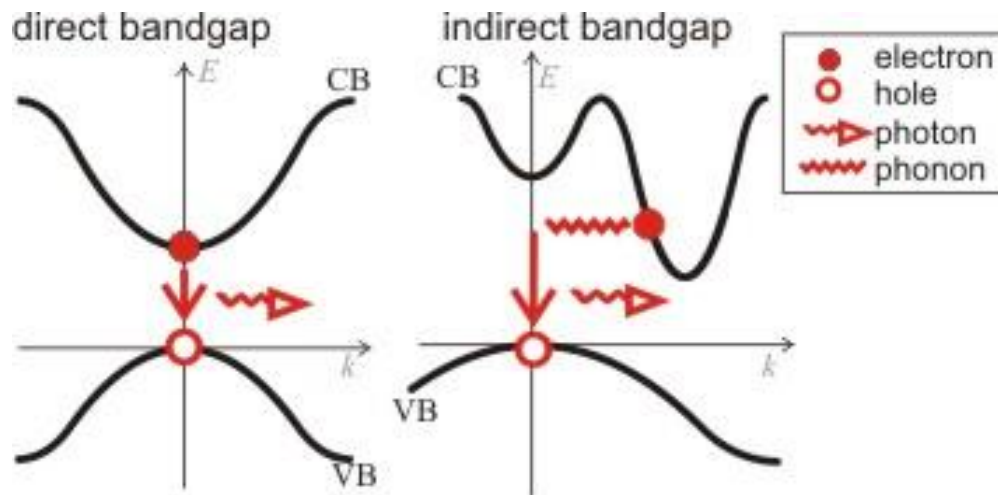


**Figure 2.5: Diagram of direct and indirect band gap for semiconductors.**

To determine exact value of band gap of material from the absorption graph, the data is needed to be replotted. For a direct semiconductor, around the band gap  $\alpha$  obeys the equation

$$\alpha(\hbar\omega) \propto \frac{\sqrt{\hbar\omega - E_{gap}}}{\hbar\omega} \quad (2.6)$$

Therefore by plotting the photon energy  $\hbar\omega$  over  $(\alpha \cdot \hbar\omega)^2$  and fitting a straight line to this plot, the precise value of  $E_{gap}$  can be find at intersection of graph with y-axis.

For the indirect semiconductor the theoretical expression for  $\alpha$  around the band gap is defined from Tauc expression [12]

$$\alpha(\hbar\omega) \propto \frac{(\hbar\omega - E_{gap})^2}{\hbar\omega}. \quad (2.7)$$

Therefore plotting  $\hbar\omega$  over  $\sqrt{\alpha \cdot \hbar\omega}$  will help to find  $E_{gap}$ .

However, for some materials, like amorphous silicon, the band gap is blurred because there exist many quantum mechanical energy levels outside the actual conduction and valence bands. In this case, one usually defines the band gap  $E_{04}$  as the energy at which the absorption coefficient reaches value  $10^4 \text{ cm}^{-1}$ . In my experimental measurements I will define band gap at value  $10^4 \text{ cm}^{-1}$ .

### 2.3.2. Mid-gap Region

In realistic semiconducting materials energy bands have soft edges, so sub-band transitions, the transitions between band-derived states, are possible (See Figure 2.6). Optical absorption spectra have long tails that fall off exponentially with long wavelengths (the region B in Figure 2.4). This absorption is governed by disorder

induced band tail states or 'trap' states within the band gap of the material. This allows optical transitions smaller than the band gap.

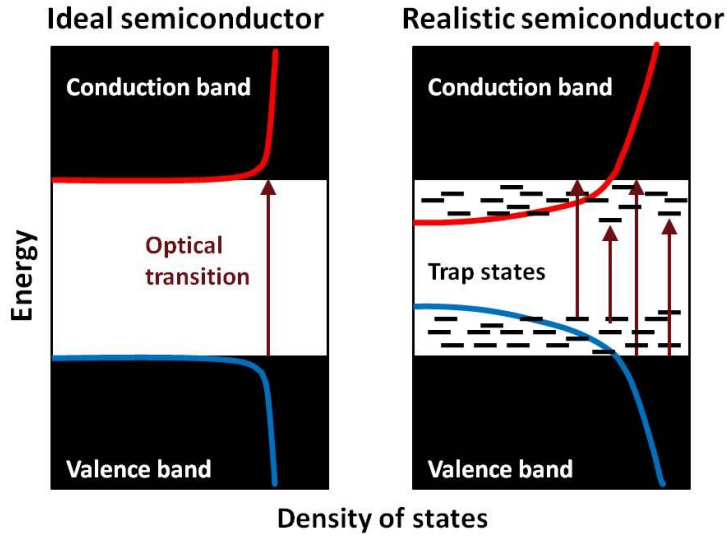


Figure 2.6: The density of electronic states for idealized bulk semiconductor and realistic semiconductor (nanocrystal material).

In 1986, Louis Brus has derived an analytical expression [13,14], which expresses how the band gap of spherical quantum dots changes with its radius R:

$$E^* = E_g^{bulk} + \frac{\hbar^2 \pi^2}{2er^2} \left( \frac{1}{m_e m_0} + \frac{1}{m_h m_0} \right) - \frac{1.8e}{4\pi\epsilon\epsilon_0 r} - \frac{0.124e^3}{\hbar^2 (4\pi\epsilon\epsilon_0)^2} \left( \frac{1}{m_e m_0} + \frac{1}{m_h m_0} \right)^{-1} \quad (2.8)$$

where  $E_g^{bulk}$  is the bandgap of the bulk semiconductor,  $\hbar$  is the Planck constant,  $m_0$  is free electron mass,  $m_e$  and  $m_h$  are the effective masses of electrons and holes,  $e$  is electron charge,  $r$  is particle size,  $\epsilon_0$  is the vacuum permittivity and  $\epsilon$  is the relative permittivity of the semiconductor material.

Equation 2.8 accurately illustrates the size-dependence of the energy bandgap, which has strong influence on the optical and electrical properties of nanoparticles material. The second term of Equation 2.8 is the quantum confinement energy, which is consistent with the particle in a box quantum confinement model:

$$E_n = \frac{n^2 \hbar^2 \pi^2}{2mL^2} \quad (2.9)$$

This term increases with decreasing nanoparticles' size and it is inversely proportional to  $r^2$ . The third term is related to the Coulomb attraction of the electron-hole pair:

$$\Delta E = \int \frac{e^2}{4\pi\epsilon\epsilon_0 r^2} dr = -\frac{e^2}{4\pi\epsilon\epsilon_0 r} \quad (2.10)$$

This term is enhanced with increasing quantum confinement and is inversely proportional to  $r$ . If the nanoparticles' size becomes sufficiently small the second term outweighs the third term resulting in broadening of the bandgap and blue shift in the optical absorption and emission spectra.

In mid-gap region, the region just below the optical band gap, the absorption is characterized by quasi-exponential decay and described by Urbach's rule

$$\alpha \sim \exp\left(\frac{\hbar\omega}{E_u}\right), \quad (2.11)$$

where  $\alpha$  is the absorption coefficient,  $\hbar\omega$  is the photon energy and  $E_u$  is Urbach energy, the slope of exponential decay in absorption. Urbach energy  $E_u$  characterizes the degree of disorder within the semiconductor material, which results in the presence of weak strained bonds. A large Urbach energy corresponds to a high level

of disorder within the material [15,16]. The slope of the Urbach energy is sensitive to all kinds of disorders and may serve as a unique parameter reflecting the collective disorder in the structure. In amorphous semiconductors like Si:H the Urbach energy varies from 30 – 100 meV.

### **2.3.3. Band-tail Region**

Optical absorption below the band-edge region within the band gap occurs from mid-gap states that can contribute to carrier recombination and reduced carrier lifetime. To investigate these tiny changes of sub-band gap absorption in semiconductor materials the PDS system has been used, where conventional Transmission and Reflection (T/R) spectroscopy fails to give accurate information. PDS helps to understand deep defect transition inside energy gap and behavior of trap states responsible for long-term photovoltaic degradation. This information about sub-band absorption of semiconductor materials helps improve the understanding of possible charge transfer processes, charge carrier generation mechanisms, and how they are influenced by the presence of defects that can act as possible trapping or recombination centers and lead to degradation of photovoltaic devices.

When one is using a PDS system to measure very small absorptions, one needs to take into consideration a couple weaknesses in the system which makes interpretation of the data sometimes harder. First, the PDS system measures all traps: surface and bulk traps together. Second, some PDS spectrums has a noise signal due an extra effect in the film — the presence of interference fringes due to the multiple-

reflections of photons within the thin film [16]. To overcome these possible difficulties, sample thickness should not be close to the wavelength of probe beam and more detailed analysis of trap density versus thickness should be made for a given material.

In our work, the photothermal deflection spectroscopy technique has successfully been applied to measurement of changes in absorption from mid-gap trap states for amorphous and microcrystalline Si to quantify light induced degradation (chapter 3), detect changes in mid-gap trap states of CdTe and PbS nanoparticle based films (chapter 4), and detect changes in mid-gap absorption of polymers films in process of degradation (chapter 5). The PDS measurement technique is independent of scattering and permits the full band gap of the semiconductor to be measured as well as the Urbach energy and the density of mid-gap trap states through analysis of the band gap and the band tail absorption.

## **2.4. References**

- 1) A. C. Boccara, D. Fournier, and J. Badoz, *Appl. Phys. Lett.* **36**, 130 (1980).
- 2) A. C. Boccara, D. Fournier, W. Jackson, and N. M. Amer, *Opt. Lett.* **5**, 377 (1980).
- 3) Y. Yang and T. Viet Ho, *Appl. Spectrosc.* **41**, 583 (1987).
- 4) R. Vyas and R. Gupta, *Appl. Opt.* **27**, 4701 (1988).

- 5) C. Wetzel, V. Petrova-Koch, F. Koch, and D. Grutzmachert, *Semicond. Sci. Tech.* **5**, 702 (1990).
- 6) W. B. Jackson, N. M. Amer, A. C. Boccara, and D. Fournier, *Appl. Opt.* **20**, 1333 (1981).
- 7) J. G. Mendoza-Alvarez, B. S. H. Royce, F. Sanchez-Sinencio, O. Zelaya-Angel, C. Menezes, and R. Triboulet, *Thin Solid Films* **102**, 259 (1983).
- 8) C. B. Davis, D. D. Allred, A. Reyes-Mena, J. González-Hernández, O. González, B. C. Hess, and W.P. Allred, *Phys. Rev. B* **47**, 13363 (1993).
- 9) C. G. Murphy and S. S. Alpert, *Am. J. Phys.* **39**, 834 (1971).
- 10) A. Mandeli, *J. Appl. Phys.* **54**, 3404 (1983).
- 11) R. A. Messenger, J. Ventre, "Photovoltaic systems engineering", 2<sup>nd</sup> edition, (CRC Press, Boca Raton, Florida, 2004), pg 335-338.
- 12) J. Tauc, "Optical Properties of Solids", (Plenum Press, New York, 1969), p. 551.
- 13) L. E. Brus, *J. Phys. Chem.* **90**, 2555 (1986).
- 14) L. E. Brus, *J. Phys. Chem.* **80**, 4403 (1984).
- 15) D. Gracin, J. Sancho-Paramon, K. Juraic', A. Gajovic', and M. C'eh, *Micron* **40**, 56 (2009).
- 16) Th. Nguyen-Tran, V. Suendo, and P. Roca i Cabarrocas, *Appl. Phys. Lett.* **87**, 011903 (2005).

# **CHAPTER 3:**

## **SILICON SOLAR CELL**



### **3.1. Background Information on Crystal Silicon, Amorphous Silicon, and Microcrystalline Silicon**

Silicon is one of the uniquely favorable photovoltaic materials. First, it is one of the most abundant elements on Earth. Second, it is an elemental semiconductor whose bandgap is nearly an ideal match to the solar spectrum. The first Si solar cell was invented by Bell Labs in 1954 and has efficiency 6% and shortly after that Si solar cells were commercialized. The most widely used material in solar panel technology today is single crystal silicon (c-Si), since it can achieve relatively high device efficiencies, but it is expensive to manufacture. It consists of silicon in which crystal lattice is continuous and does not have grain boundaries. Most silicon cells have been fabricated using thin wafers cut from large cylindrical monocrystalline ingots, which are grown by Czochralski process. Single crystal silicon is used to manufacture most Si-based microelectronic devices. Today, it appears that crystalline Si solar cells have not yet reached efficiency expectations with resulting record efficiencies of only 25% using high-quality bulk Si wafers and complex processing, as shown in Figure 1.3 [1]. Polycrystalline silicon (poly-Si), material consist of small silicon crystals, is less expensive to manufacture than c-Si, but it is also less efficient. The maximum efficiency of a poly-Si cell has reached 17% in laboratories [1]. The band gaps of c-Si and poly-Si are the same, 1.12 eV.

Amorphous silicon (a-Si) solar cell, the non-crystalline allotropic form of silicon, tend to have lower efficiency than those made from c-Si, but are widely used because they cost less and require less raw material. The bandgap of aSi is higher

than crystalline silicon 1.7 eV and collects light more strongly in the visible part of the sun's spectrum. Chemical bonding of a-Si atoms is nearly unchanged from crystals. Small, disorderly variation in the angles between the bonds eliminates regular lattice structure. Typically a-Si solar cell device has the electronic structure of a p-i-n junction, which includes front side glass, TCO, thin film silicon, back contact, polyvinyl butyral, and back side glass. The highest efficiency for a-Si solar cells to date is 12.5%, achieved by United Solar (see Figure 1.3).

Amorphous silicon is generally known as “hydrogenated amorphous silicon” or a-Si:H. In early studies of amorphous silicon, it was determined that plasma-deposited amorphous silicon contained a significant percentage of hydrogen atoms bonded into the amorphous silicon structure. These atoms were discovered to be essential to the improvement of the electronic properties of the material. Hydrogenated amorphous silicon (a-Si:H) solar cells have many advantages over c-Si cell. First, technology is relatively simple and inexpensive for a-Si:H. It can be deposited over large areas (up to 1 m<sup>2</sup> or more) by plasma-enhanced chemical vapor deposition (PECVD) process [2]. Second, for a given layer thickness, a-Si:H absorbs much more energy than c-Si (about 2.5 times). 1 μm thickness is enough to absorb all photons over 1.7 eV. As a result, much less material required for a-Si:H films preparation, which make final product lighter weight and less expensive. Third, a-Si:H can be deposited on a wide range of substrates, including flexible, curved, and roll-away types due to very low temperature deposition, as low as 75°C. This flexibility allows creating easy to install solar cell.

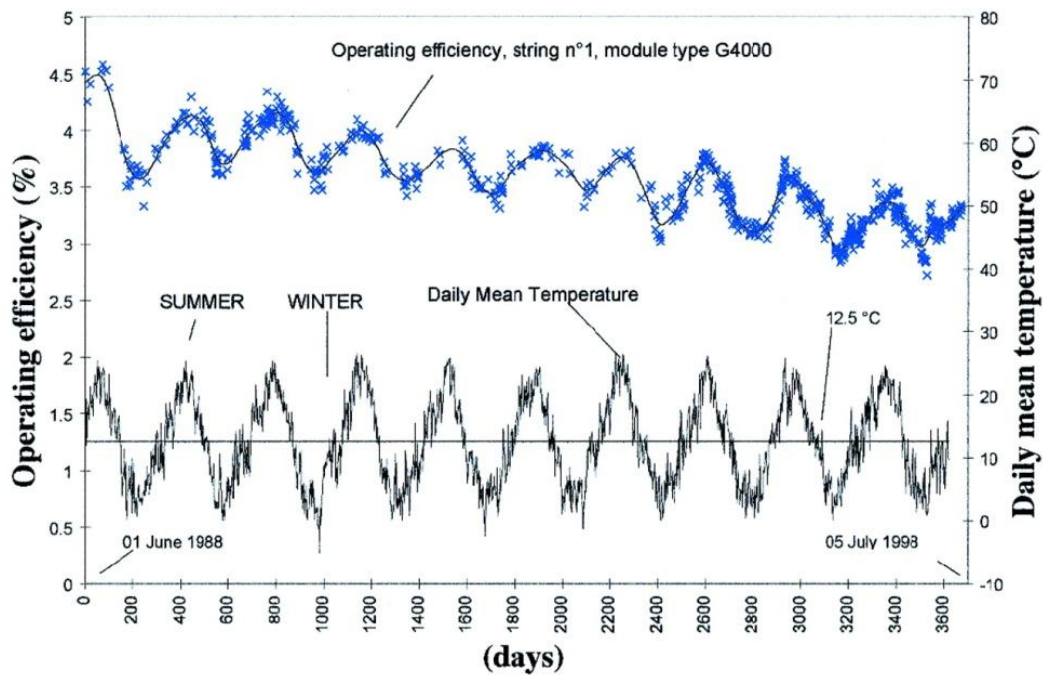


**Figure 3.1: Typical efficiency performance of a-Si modules as measured at the TISO in Switzerland. The amplitude of efficiency oscillates due to seasonal variation in temperature with steady decline in value through years. Blue crosses represent the average weekly operating efficiency.**

As main disadvantage for a-Si:H photovoltaics over c-Si is lower stabilized efficiency, which is between 4-10% for actual commercial modules and more than twice small than for crystalline silicon [2]. The main reason for the limitation in stabilized efficiency is the Staebler-Wronski effect (SWE) or light-induced degradation, in which the efficiency decreases to a stabilized but lower value after ~1000 hours of illumination and subsequent annealing at 100° to 250°C can restore the original efficiency, discussed in section 1.4. On Figure 3.1[2] typical efficiency performance of amorphous silicon modules is shown, which was measured at the TISO outdoor testing site near Lugano (Switzerland). Because of the SWE, the

efficiency of aSi first decreases during winter, but then recovers back to higher value during the warmer summer months. During these periodic oscillations through years the amplitude of these seasonal variations of efficiency steadily decreases toward the lower value [2].

Microcrystalline silicon ( $\mu\text{c-Si}$ ) or also known nanocrystalline silicon (nc-Si) has an allotropic form of silicon with paracrystalline structure and has a lot of potential in solar technology since it is easier to fabricate than poly-Si and has low bandgap  $\sim 1.12\text{eV}$ . Microcrystalline silicon has intermediate properties between a-Si and poly-Si: small crystalline grains (0.1-100  $\mu\text{m}$ ) embedded in an amorphous silicon matrix. On Figure 3.2 [2] the morphology structure of  $\mu\text{c-Si:H}$  grown on a-Si:H is shown.  $\mu\text{c-Si}$  has many useful advantages over a-Si:H for solar cell. First, if grown properly  $\mu\text{c-Si}$  can have higher electron mobility than a-Si, due to the presence of the silicon crystallites. Second, it has better stability and suffer less from the Staebler–Wronski effect than a-Si:H. Third, it has high absorption in the red and infrared wavelengths. And finally, deposition processes for  $\mu\text{c-Si}$  need lower temperatures similar to a-Si PECVD deposition technology with more sensitive contaminant requirements, as opposed to high temperature CVD processes and laser annealing, in the case of poly-Si [1].

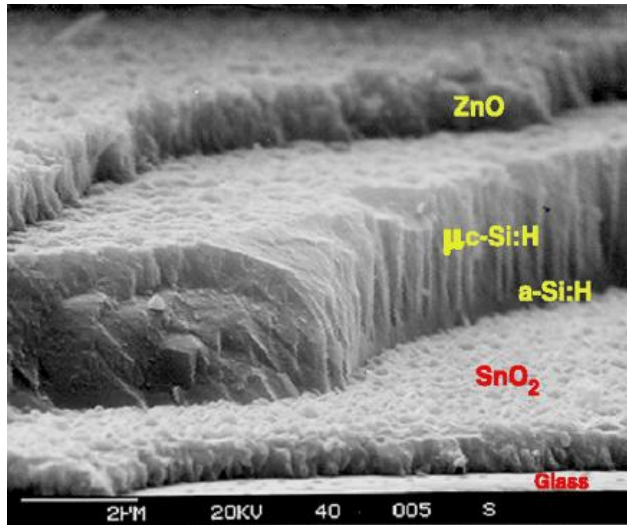


**Figure 3.2: Microcrystalline and amorphous silicon tandem solar cell from IMT (so-called “micromorph” solar cell). Scale bar is 2  $\mu\text{m}$ .**

All silicon films for my research were provided by the Applied Materials company, details of their fabrications and structure are confidential.

### **3.2. Absorption of Silicon Films**

In silicon films, the optical absorption of defects and impurities is most readily observed below the band edge since it is not obscured by the much larger band-to-band absorption. Consequently, the mid-gap absorption spectra should provide information about the number and energy level of defects in these materials. The films are typically 1  $\mu\text{m}$  or less thick and are not optically homogeneous, making conventional transmission measurements of absorption coefficients  $\alpha$  unreliable below 50—100  $\text{cm}^{-1}$ . By photothermal deflection spectroscopy (PDS), which directly measures the optical absorption and which is highly insensitive to scattering, we

measure an absorption tail extending down to 0.6eV. The source of this tail absorption for amorphous and microcrystalline silicon are silicon dangling-bonds defects which are located below the conduction band and doping introduced defects at the same energy level [3].

In previous research it was demonstrated that dangling bonds are the cause for the dominating electronic defect in the mobility gap in a-Si:H and this defect is to a large extent responsible for the charge carrier properties via recombination and trapping [4]. Typically the dangling bonds in a-Si:H are identified by electron spin resonance (ESR) measurements, a quantitative measure of the density of defects, which detect the dangling bond in a singly occupied, neutral charge state. In  $\mu\text{c-Si:H}$  the situation is more complicated as the dangling bond type of defect could be located in different local environments of the material, crystalline, and amorphous regions and grain boundaries. Nevertheless, in  $\mu\text{c-Si:H}$  there is a good correlation between spin density and the material quality, which has been successfully used for material and device development [5].

A typical optical absorption spectrum of  $\mu\text{c-Si:H}$ , a-Si:H, and c-Si is shown in Figure 3.3 [5]. Between photon energy of 1.1 and 1.6 eV the optical absorption of  $\mu\text{c-Si:H}$  is similar to crystalline silicon. At higher photon energies enhancement in  $\mu\text{c-Si:H}$  absorption is caused by amorphous material fractions in microcrystalline and scattering at the surface and at grain boundaries. At low photon energies near the crystalline band edge, the absorption of  $\mu\text{c-Si:H}$  is enhanced due to band tail states and defects due to dangling bonds.

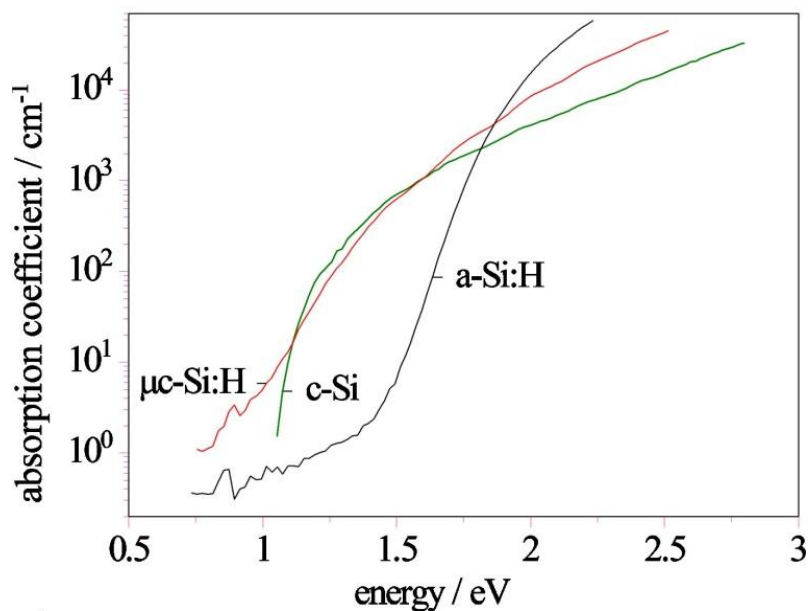


**Figure 3.3: Absorption coefficient vs photon energy, of single crystalline silicon (c-Si), amorphous silicon (a-Si:H) and microcrystalline silicon ( $\mu\text{c-Si:H}$ ), as measured by PDS.**

Figure 3.4 shows our measurement of PDS absorption coefficient of amorphous silicon (a-Si:H), microcrystalline silicon ( $\mu\text{c-Si:H}$ ) deposited on 50-200nm of a-Si seeding layer and with 50% crystalline fraction, and amorphous silicon (pa-Si:H) with Boron as a p type doping. For a PDS spectrum the absorption coefficient has the presence of interference fringes due to the multiple-reflections of photons within the thin film. This is particularly visible for the a-Si:H and  $\mu\text{c-Si:H}$  samples. In order to distinguish the features of silicon films that could be due to various bonding configurations rather than to interference effects, we tried to compare PDS spectra of samples having different thicknesses (700 nm and 1000 nm), since the period of interference fringes should strongly depend on this

parameter and wavelength of the laser. However, preparation of the samples has a limit due to with thickness, so we can not eliminate interference and the same interference shape is observed for both samples with slight change of periodicity.

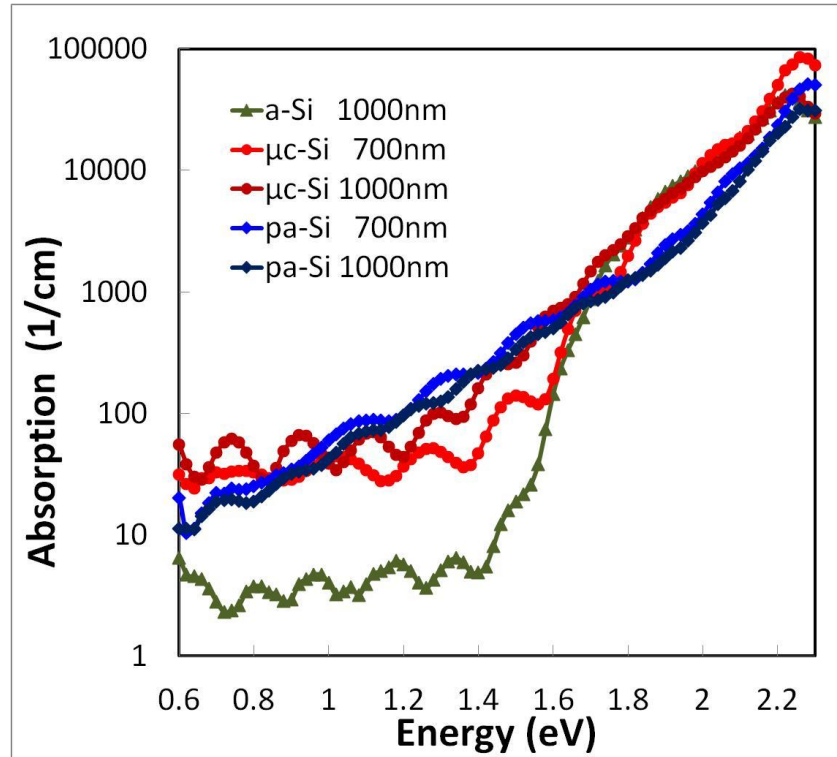


**Figure 3.4: Absorption coefficient vs photon energy, of amorphous silicon (a-Si:H), microcrystalline silicon ( $\mu\text{c-Si:H}$ ) deposited on 50-200nm of a-Si seeding layer and with 50% crystalline fraction, and amorphous silicon (pa-Si:H) with Boron doping as measured by PDS.**

In high quality a-Si:H, boron doping, which can be achieved by glow-discharge decomposition  $\text{SiH}_4 + \text{B}_2\text{H}_6$  mixtures, increases significantly the defects' absorption in the tail and modifies the optical band gap. The films absorption has light shifted to higher energies which may be due to B-induced heterogeneities or the disorder parameters [6]. The sub-gap absorption tail rises as the doping level is

increased, while the slope of the exponential edge decreases as the dopant concentration is increased [3]. Concurrently, there is a pronounced shift to lower energies and a broadening of the exponential region. According to Rebal paper [7], by using photomodulated infrared spectroscopy of a-Si:H, the maximum of the band is located around 0.6eV for boron doping, which is to be related to the fact that the valence band tail of a-Si:H is more spread out in the gap than the conduction band tail. So band tail region for a-Si b-doping is on a boarder of PDS photon energy measuring region.

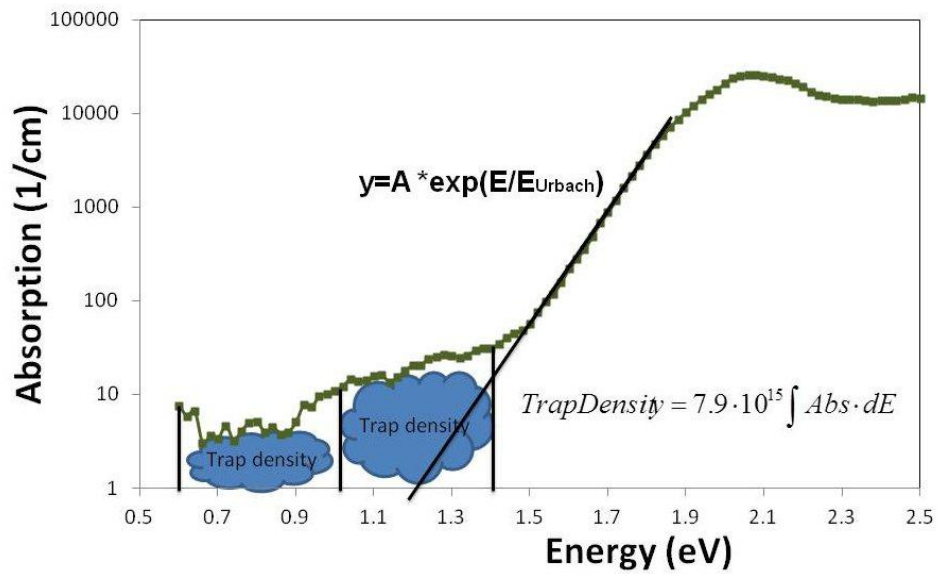


**Figure 3.5: Absorption coefficient of amorphous silicon vs energy.**

One of main characteristic quantities for a sample of amorphous silicon is the Urbach energy  $E_u$  which describes the “blurring” of the valence and conduction bands, which is defined by equation (2.11) and describes the quasi-exponential slope

of absorption around the band gap. In our semilogarithmic plots this slope becomes linear as shown by the black line in Figure 3.5. For our silicon samples from Figure 3.4, we obtained Urbach energy, which is present in Table 3.1. Typically, very good samples of amorphous silicon have an Urbach energy around 0.05 eV so our samples are good quality with respect to the blurring of the energy bands.

	<b>1000nm</b>	<b>700nm</b>
<b>μc-Si:H</b>	155meV	102meV
<b>pa-Si</b>	239meV	236meV
<b>a-Si:H</b>	53.8meV	

**Table 3.1: Urbach energy of amorphous silicon (a-Si:H), microcrystalline silicon (μc-Si: H), and amorphous silicon (pa-Si:H) with Boron doping, which are measured by PDS and have absorption graphs on Figure 3.4.**

By using PDS data, we can quantities defect effect and calculate the number of defects N (traps) for silicon films from:

$$N = \frac{cnm}{2\pi^2\hbar^2} \left[ \frac{(1+2n^2)^2}{e^2 f_{oj} 9n^2} \right] \int \alpha dE \quad (3.1)$$

where c is the speed of light, n is the index of refraction of the material, m is the electron mass, e is the electron charge, and  $f_{oj}$  is the oscillator strength of the absorption transition. The expression within the large parentheses is the inverse square of the effective charge of the defect when adjusted by the local-field corrections used in interpreting the infrared spectra of silicon [3].

The index of refraction of the silicon is  $n=3.8$ . Assuming  $f_{0j} = 1$  and recognizing that the local-field corrections have been empirically determined to overestimate the correct local field by a factor of 2 in a-Si:H, the numerical factor for a-Si:H defects in equation (3.1) is

$$N = 7.9 \times 10^{15} \text{cm}^{-2} \int \alpha(\text{cm}^{-1}) dE \quad (3.2)$$

Defects occur during film growth because, due to the lack of mobility of the species arriving at the surface and to the rigidity of the covalent bonding, a large proportion of atoms cannot fulfill complete tetrahedral coordination of silicon. The most common defect is a dangling bond at a 3-fold coordinated site, but strained or “weak” bonds can equally be considered as defects; 5-fold coordinated atoms have also been envisaged [6, 8]. I will talk more about microscopic process leading to the creation of metastable dangling bonds later in Section 3.4. Nature and concentration of defects are strongly dependent on the deposition processes, and they are intimately related to the disorder. All the defects are susceptible to introducing a large variety of localized states in the gap, depending on their charge state and their local configuration.

In comparison to PDS data the dangling bond density for a-Si:H calculated by constant photocurrent method (CPM) method [9] is defined as

$$N_{DB} = (1.9 \pm 0.3) \cdot 10^{16} \text{cm}^{-2} \int \alpha_{CPM}(\text{cm}^{-1}) dE \quad (3.3)$$

Then the prefactor difference between CPM dangling bond density and PDS defect density is 2.4. Neither of these equations (3.2) nor (3.3) requires that all deep defects be dangling bonds, merely that the total defect density be proportional to the dangling

bond density. So PDS sees approximately twice (2.4 times) as much absorption for the same defect density. This a factor of 2 comes from two main facts: 1) CPM sees only transitions from below mid-gap into the conduction band, while PDS sees transitions from the conduction band and the valence band into states above the mid-gap. 2) PDS measures bulk defect and surface states, while CPM does not see surface states. So according to Smith, to find bulk effect of materials, surface effects need to be subtract from the PDS data, which can be done by a linear relationship with a factor 2.4 between defect density and dangling bonds density in a-Si:H films. However, the correlation does not work for all samples, which suggests that other defects might participate in the optical absorption [6].

### **3.3. Silicon Crystallinity Impact on Microcrystalline Silicone**

One of the most important parameter in microcrystalline silicone, which has intermediate properties between crystalline and amorphous silicon, is its' crystallinity or crystalline fraction. The structural and optical properties of  $\mu\text{c-Si}$  films are strongly impacted by microcrystalline grains embedded in an amorphous silicon matrix. The band-gap of  $\mu\text{c-Si}$  films increases with the fraction of “small” crystals, which is attributed to a quantum size confinement effect.

Andreja Gajovic group in their papers [10,11] investigates changes in absorption coefficient for  $\mu\text{c-Si}$  films with different crystallinity, which is plotted on Figure 3.6 [11]. Urbach energy increases with the total crystalline fraction. This can be understood by considering the Urbach energy as a comprehensive measure of

deviations in a structure from the average material structure. At lower energies, a deviation from the Urbach expression is due to two main parameters: first, the presence of crystals with optical properties like c-Si, which has a significant absorption in this range, and, second, the presence of defects, typically dangling bonds, like in a-Si. Also, the density of defects increases with the crystalline fraction, which can be explained by taking into account the fact that the presence of defects is mainly located at the grain boundaries [11].

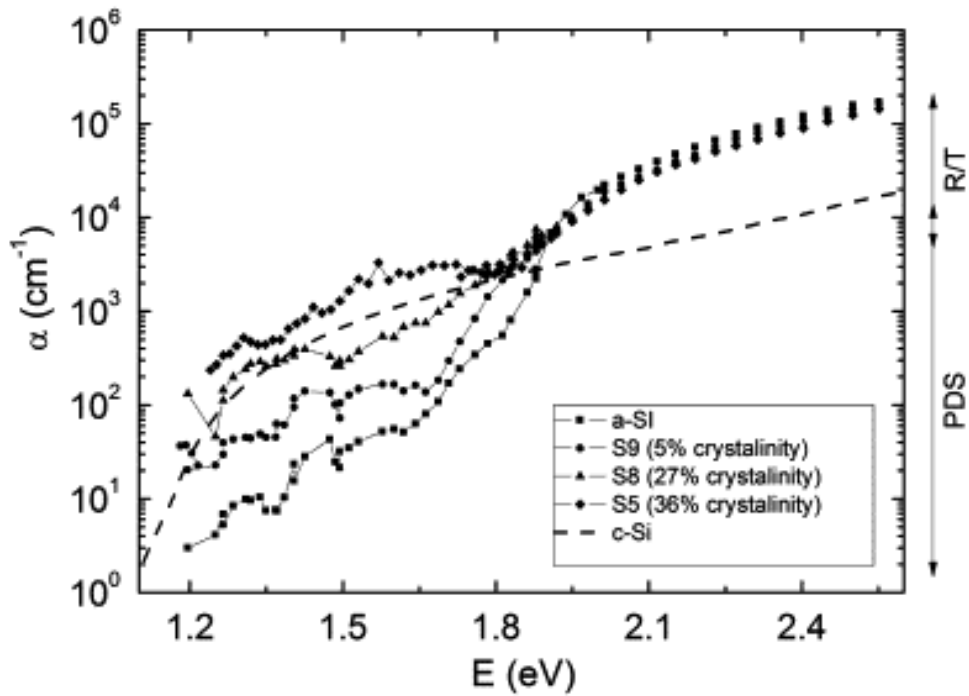


Figure 3.6: Absorption coefficient for  $\mu\text{-Si}$  films with different crystallinity determined by photothermal deflection spectroscopy. Absorption coefficient of c-Si is added for comparison.

The simplest model to explain and predict microcrystalline absorption  $\alpha(\mu\text{Si})$  response is sum of  $\alpha$ -amorphous  $\alpha(\text{aSi})$  with band gap at 1.7 eV and  $\alpha$ -pure crystalline

$\alpha(\text{cSi})$  with band gap at 1.12 eV layers multiplied with corresponding volume contributions [10]. The mathematical expression of the model is

$$\alpha(\mu\text{cSi}) = f \cdot \alpha(\text{cSi}) + (1 - f) \cdot \alpha(\text{aSi}) \quad (3.4)$$

where  $f$  is a crystalline fraction of microcrystalline silicon. Crystalline silicon has indirect band gap, so its absorption is defined by Tauc equation (2.7) with  $E_g = 1.12$  eV. This fit describes qualitatively well the spectra in all spectral range in Figure 3.7. In the high-energy part of spectra amorphous silicon properties dominate. At lower energy between 1.2 - 1.6 eV crystal phase of material brings additional absorption and shifts absorption of  $\mu\text{c-Si}$  to a higher value. However, below 1.2 eV the model starts to fail, since the contribution of crystal phase cannot be resolved from the defect level of amorphous.

This model can be applied to define how crystalline the bi-layer samples or micromorph films are. In Figure 3.7 absorption of  $\mu\text{c-Si}$  films deposited on 50-200 nm of a-Si seeding layer are plotted. By fitting equation (3.4) to PDS absorption graphs, 1000 nm thick  $\mu\text{c-Si}$  film contains ~45% crystalline Si and 700 nm thick  $\mu\text{c-Si}$  film contains ~15% crystalline Si. However, similar to microcrystalline films this model does not explain presence of a higher structural disorder and a higher number of defects at low energies.

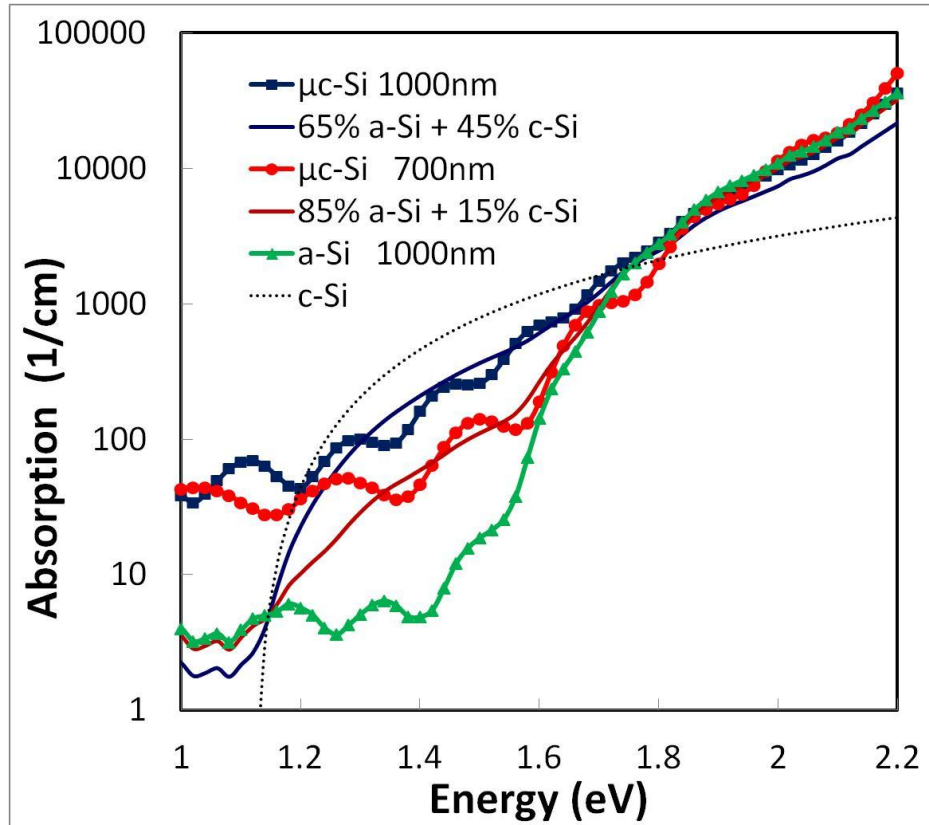
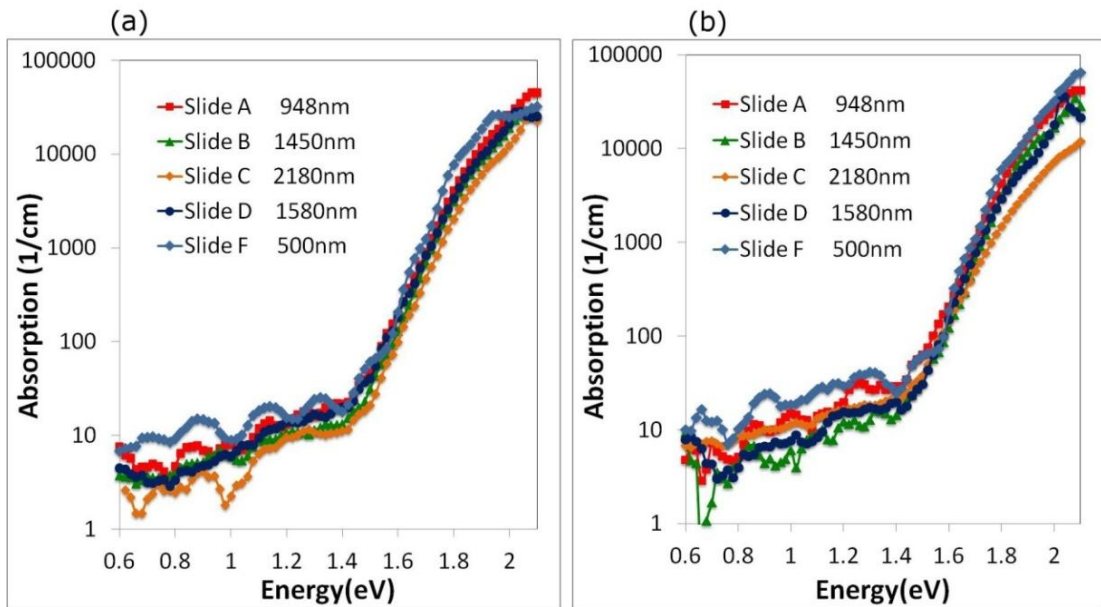


Figure 3.7: Determining fraction of crystalline Si for micromorph films with different thickness with photothermal deflection spectroscopy.

### 3.4. Staebler-Wronski Effect in Amorphous Silicon Films

Light-induced metastable changes in the properties of hydrogenated amorphous silicon, the Staebler-Wronski effect (SWE), have been studied intensively in a last several decades to understand the reversible changes in the density of localized gap states of a-Si:H as well as the resulting change in the electronic, optical, and magnetic properties of this material. A direct evidence for the creation of states in the mobility gap of a-Si:H by prolonged illumination comes from a variety of experiments: reversible changes in the field effect [12-13], the deep-level transient

spectroscopy response [14], the defect luminescence [15], the sub-gap absorption [16], and from an increase of the Si dangling-bond signal in the electron-spin resonance [17-18]. All these methods agree qualitatively that intense illumination leads to the creation of additional metastable states in the gap of amorphous silicon which influence its electronic and optical properties by decreasing the lifetime of excess carriers and shifting the position of the dark Fermi level in a reversible manner. However, these different experiments have discrepancies in quantitative values of the absolute density of the metastable defects, their position in the mobility gap, and whether one or more types of defects created by illumination [19].



**Figure 3.8: PDS absorption coefficient for a-Si:H with different thickness before (a) and after (b) 12 hours of light induced degradation under  $100\text{mW}/\text{cm}^2$  metal-halide lamp.**

In our research we used our PDS system to understand Staebler-Wronski effect on bulk and surface properties of a given a-Si:H sample. For this purpose, five

different thickness a-Si:H films were illuminated by a  $100\text{mW}/\text{cm}^2$  metal-halide light with high UVA content at  $35^\circ\text{C}$  and measured by the PDS system before and after illumination. PDS provides the extremely sensitive low-energy absorption for these samples, as demonstrated in the Figure 3.8. So changes in the band tail region can be detected and information about the defect densities can be calculated. However, to deduce the distribution of the defect states from PDS data, we will need to find a way to separate bulk and surface states, since PDS defect states represent a convolution of the initial and the final densities of states of all transitions occurring at a given photon energy [6].

The band gap tail of a-Si has two distinguish areas: below and above energy  $1.0\text{eV}$ . In the region below  $1.0\text{eV}$  the band absorption coefficient is significantly smaller than in the region above  $1.0\text{eV}$ , as shown on the Figure 3.5. So it is more convenient to find two types of defect density by using the formula (3.2): a low energy trap density  $N_t$  ( $0.6\text{-}1.0\text{eV}$ ) and a high energy trap density  $N_t(1.0\text{-}1.4\text{eV})$ , which are plotted in Figure 3.9(a). Surprisingly, the average difference between these two types of trap states is approximately 2.4, which is similar to the factor 2.5 between the defect density and the dangling bonds density in the a-Si:H films. This result could imply that the low energy traps density  $N_t$  ( $0.6\text{-}1.0\text{eV}$ ) may have correlation to the dangling bonds density of amorphous silicon and the different absorption regions in the tail corresponds to the different type of effects. To test this hypotheses, we investigate changes of the total traps of a-Si:H samples vs thickness, as shown on a Figure 3.9(b). The high energy traps increase linearly with the

thickness, which correspond to the bulk changes of the material. The low energy traps remain independent from the thickness, which correspond to the surface effect of the material. So the surface and the bulk contribution effects can be separated by the energy of the traps states.

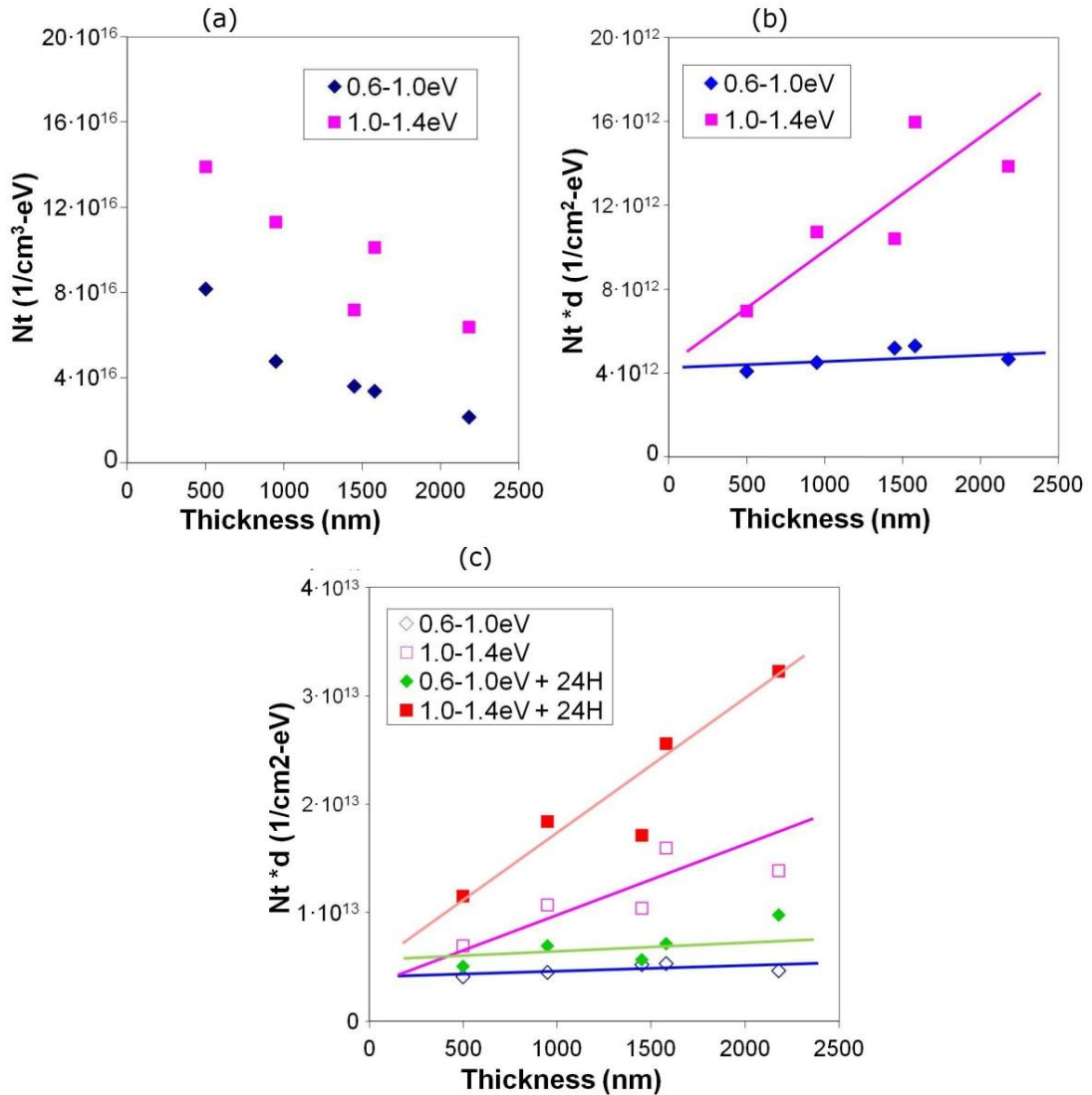


Figure 3.9: (a) Variation of low energy trap density  $N_t$  (0.6-1.0eV) and high energy trap density vs thickness for a-Si:H measured by PDS (b) Variation of total trap states of a-Si:H vs thickness. (c) Variation of total trap states of a-Si:H vs thickness before and after 24 hours of light soaking.

For a common a-Si film with thicknesses  $\sim 1\mu\text{m}$ , the surface defect density is in an order  $10^{12}\text{ cm}^{-2}$  [9]. So for the bulk deep defect density less than  $10^{16}\text{ cm}^{-3}$ , which qualify as high quality films, there is more optical absorption due to the surface states than the bulk. For the bulk deep defect density higher than  $10^{16}\text{ cm}^{-3}$ , there is more optical absorption due to the bulk states. In our case, from the Figure 3.9(a) the bulk defects trap states density is approximately  $10^{17}\text{ cm}^{-3}$ , which is several times higher than the surface trap states. After light soaking for 24 hours under 1 sun illumination both trap densities increased, where the high energy traps changed more dramatically than the low energy traps (see Figure 3.9 (c)) Hence, the bulk of the material is more susceptible to the metastable changes during light soaking. So a surface and a bulk contribution to the Staebler-Wronski effect can be separated and for our a-Si samples the Staebler-Wronski effect is predominantly the bulk effect of the material.

There are several microscopic processes have been proposed to explain the SWE. The first one involves the separation of weak Si—Si bonds into one or two Si dangling bonds and is, therefore, known as the "bond-breaking" model. This mechanism, together with a possible rearrangement of hydrogen atoms in a- Si:H, has been put forward by Staebler and Wronski [20], Pankove and Berkeyheiser[15], and, in more detail, by Dersch [18]. A different picture of the SWE involves reversible changes in the charge or hybridization state of already existing dangling bonds. This kind of mechanism has been proposed by Adler [21]. Finally, there has been some

experimental evidence that the magnitude of the SWE increases with the concentration of impurities like oxygen, nitrogen, or carbon in a-Si:H [22]. This observation has led to a model according to which the SWE is not intrinsic to a-Si:H, but rather linked to the presence of impurities in special microscopic configurations [19].

### **3.5. Staebler-Wronski effect in Different Types of Silicon Films**

For a-Si films SWE degradation is a major disadvantage to becoming a photovoltaic material, so we investigate light induced degradation of different variation of a-Si: doping of a-Si with Boron or microcrystalline silicon. For our experiment we compared PDS absorption coefficient for a-Si:H,  $\mu\text{c-Si:H}$ , and Boron doped a-Si films before and after 12 hours of light induced degradation under  $100\text{mW/cm}^2$  metal-halide lamp, as shown on a Figure 3.10(a). After light soaking a relative change in states below the band gap for  $\mu\text{c-Si}$  film increases by 50% with a broad peak around 1.1eV, while a relative change in states for a-Si film increases by 160% with a sharp peak around 1.0eV, as shown in a Figure 3.10(b). The microcrystalline silicon film suffers less from the Staebler–Wronski effect than the amorphous silicon film, suggesting that the disorder in the amorphous silicon network plays a major role in SWE. Other properties, such as a hydrogen concentration or a concentration of impurities, have smaller effect. The boron doped a-Si film shows stability against light soaking, which is consistent with previous research [19,23]. It is an interesting phenomenon, since a doped material has an increase of the induced

metastable states with increasing boron or phosphorus doping and has the occurrence of a "negative Staebler-Wronski effect" in lightly doped samples [19].

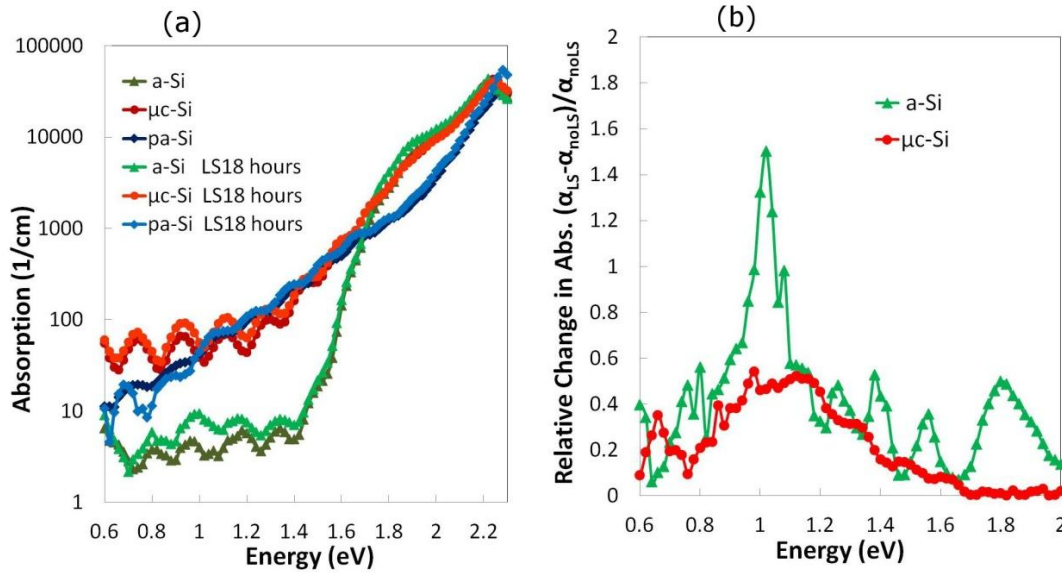


**Figure 3.10: (a) PDS absorption coefficient for a-Si:H,  $\mu\text{c-Si:H}$ , and pa-Si films before and after 12 hours of light induced degradation. (b) Relative change in absorption coefficient before and after light soaking for for a-Si:H and  $\mu\text{c-Si:H}$  films with 1000 nm thick.**

### 3.6. Impact of Al:Zn:O Layer

Doped amorphous silicon has a strong surface effect, which controls performance in thin silicon films and make it impossible to see bulk changes inside of the material in first stage of light degradation. To eliminate surface effects and leakage currents, passivation of surface states with very thin AZO coating was introduced [16,17]. We observed absorption coefficients of a-Si and boron doped a-Si (pa-Si) before and after AZO coating with the PDS system, as shown on Figure 3.11. However, AZO film has a strong trap level in IR region due to Al-doping in ZnO with

conduction band around 0.2eV and extended band tails into the region of interest. The concentration of these traps states was unusually high for a very thin layer of AZO. AZO traps dominate below the band gap in our passivated a-Si and boron doped a-Si films and make PDS absorption data useless. We conclude that the effect AZO films may serve as an excellent surface passivation layer and to improvements in the reverse and forward bias region [24], but it is not effective for measuring bulk states with PDS system.

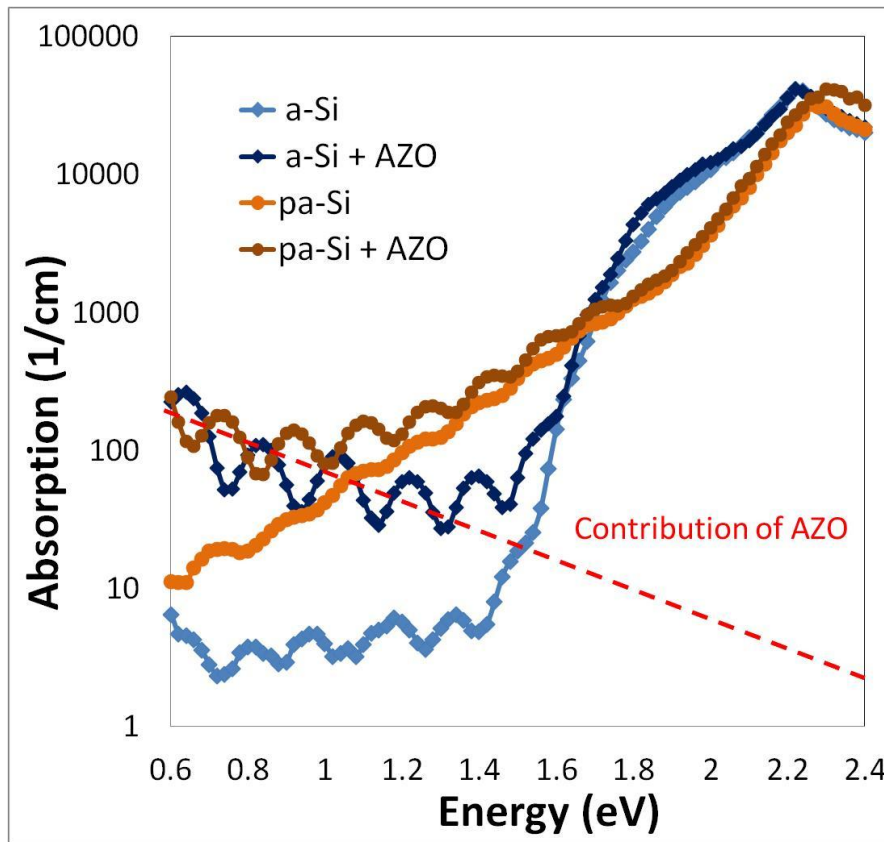


**Figure 3.11: PDS absorption coefficient for a-Si:H,  $\mu$ c-Si:H, and pa-Si films before and after 12 hours of light induced degradation.**

### 3.7. References

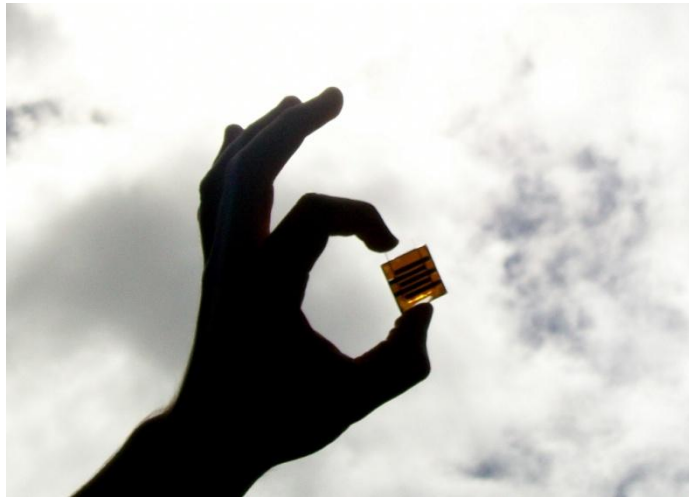
- 1) R. B. Bergmann, *Appl. Phys. A* **69**, 187 (1999).
- 2) A. Shah, P. Torres, R. Tscharnner, N. Wyrsh, H. Keppner, *Science* **285**, 692 (1999).
- 3) W. B. Jackson and N. M. Amer, *Phys. Rev. B* **25**, 5559 (1982).
- 4) R. A. Street, "Hydrogenated Amorphous Silicon", (Cambridge University Press, New York NY, 1991), pg 88-91.
- 5) S. Klein, F. Finger, R. Carius, T. Dylla, and J. Klomfass *J. Appl. Phys.* **102**, 103501 (2007).
- 6) M. L. Theye, *Phys. Scripta* **T29**, 157, (1989).
- 7) K. Rerbal, J. N. Chazalviel, F. Ozanam, I. Solomon, *J. Non-Cryst. Sol.*, **299–302**, 585 (2002).
- 8) Fritzsche, H., *J. Non-Cryst. Sol.* **97-98**, 95 (1987).
- 9) Z E. Smith, V. Chu, K. Shepard, S. Aljishi, D. Siobodin, J. Kolodzey, S. Wagner, and T. L. Chu, *Appl. Phys. Lett.* **50**, 1521 (1987).
- 10) D. Gracin, J. Sancho-Paramon, K. Juraic', A. Gajovic', M. C'eh, *Micron* **40**, 56 (2009).
- 11) J. Sancho-Parramon, D. Gracin, M. Modreanu, A. Gajovic', *Sol. Energ. Mat. Sol. C.* **93** 1768 (2009).
- 12) N. B. Goodman, *Philos. Mag. B* **45**, 407 (1982).

- 13) M. Grunewald, K. Weber, W. Fuhs, and P. Thomas, *J. Phys.(Paris) Colloq.* **42**, C4-523 (1981).
- 14) D. V. Lang, J. D. Cohen, J. P. Harbison, and A. M. Sergent, *Appl. Phys. Lett.* **40**, 474 (1982).
- 15) J. I. Pankove and J. E. Berkeyheiser, *Appl. Phys. Lett.* **37**, 705 (1980).
- 16) N. M. Amer, A. Skurnanich, and W. B. Jackson, *Physica B&C*, **117-118**,897 (1983).
- 17) I. Hirabayashi, K. Morigaki, and S. Nitta, *Jpn. J. Appl. Phys.***19**, L357 (1980).
- 18) H. Dersch, J. Stuke, and J. Beichler, *Appl. Phys. Lett.* **38**, 456 (1980).
- 19) M. Stutzmarin, W. B.Jackson, and C. C. Tsai, *Phys. Rev. B* **32**, 23 (1985).
- 20) D. L. Staebler and C.R. Wronski, *J. Appl. Phys* **51**, 3262 (1980).
- 21) D. Adler, M. E. Eberhart, K. H. Johnson, and S. A. Zygmunt, *J. Non-Cryst. Solids* **66**, 273 (1984).
- 22) R. S. Crandall, D. E. Carlson, A. Catalano, and H. A. Weakliem, *Appl. Phys. Lett.* **44**, 200 (1984).
- 23) J. Meier, F. L. Fliickiger, H. Keppner, and A. Shah, *Appl. Phys. Lett.* **65**, 15 (1994).
- 24) S. Baek, H. S. Jang, J. H. Kim, *Curr. Appl. Phys.* **11**, 530 (2011).

# **CHAPTER 4:**

## **NANOPARTICLES**

### **SOLAR CELLS**



## 4.1. Introduction

For almost 30 years, interest in inorganic colloidal semiconductor nanocrystals (NCs) or quantum dots (QDs) kept growing, as a new generation of semiconductor devices including solar cells, transistors, photodetectors, LEDs and biological labeling emerged. The typical dimensions of nanoparticles are around 1-10 nm which is generally smaller than the exciton Bohr-radius (the distance in an electron-hole pair) and in an order of a few hundred to ten thousands of atoms (Figure 4.1). So the electronic characteristics of become strongly size-dependent due to the quantum confinement. Consequently, nanoparticles show intermediate electronic properties between bulk semiconductor solids and discrete molecules.

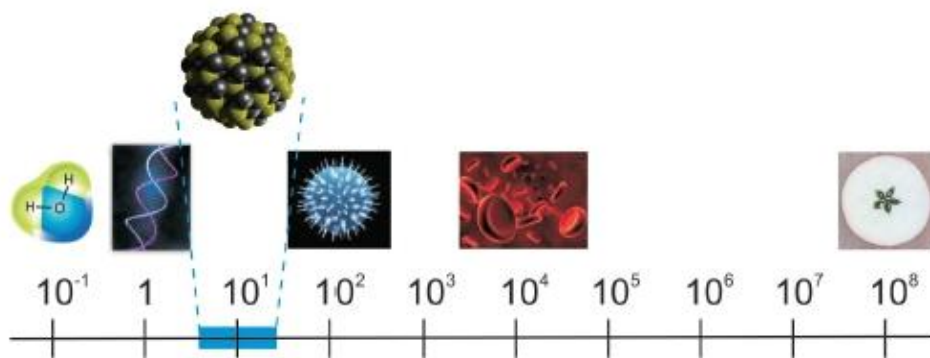


**Figure 4.1: Typical dimension of QDs is located between discrete molecules and microorganisms, picture is done by K. Szendrei.**

Quantum dots have attracted increasing attention mostly due to their exceptional optical properties. They can be synthesized from group II-VI, III-V or IV-VI semiconductors in solution via hot-injection approaches. Devices made with nanoparticles can be processed at room-temperature and atmospheric pressure similar

to organic materials. QDs have great potential for device active layers, since their absorption can be maximized to cover the solar spectrum with the near-infrared region, contrary to most of the organic polymers and many bulk semiconductors. Due to the quantum confinement effect, optical properties of the nanoparticles exhibit strong size dependence; therefore, their band gap and absorption properties can be tuned with particle size [1-4]. Equation (2.8) accurately demonstrates the size-dependence of the energy band gap, which defines the electrical and optical properties of nanoparticles. For very small nanoparticles the  $1/r^2$ -term of the equation outweighs the  $1/r$ -term and causes broadening of the band gap and blue shift in the optical absorption.

A key issue with nanocrystal semiconductors is to control surface chemistry in ligand shell. Since in QDs, incomplete surface passivation of nanocrystals causes the presence of trap states below the optical gap, which play a critical role in the performance of semiconductor devices including optical efficiency and leakage current. The high surface to volume ratio of nanoparticles in a thin film form can lead to a very high density of surface states that can trap electrons and ultimately limit a device performance. By using PDS and electrical device characterization, the role of trap states in solar cell devices made of both quantum confined and sintered nanoparticles is investigated in this section, as well as possible degradation mechanisms.

Two general areas of possible degradation may be defined:

- i. Within the film itself: Nanoparticles may lose passivation and/or develop mid-gap recombination centers. Labile ligands make the film particularly vulnerable to attack by oxygen and moisture.
- ii. At the film-metal interface: Shallow-work-function metals are known to be oxidized rapidly; they also may react with ligands in the film.

## **4.2. Cadmium Telluride Nanoparticles Solar Cells**

The majority of this material was published in the Applied Physics Letters in January 2012 [5].

### **4.2.1. Background Information**

One of the most commonly used materials for thin film solar cells is Cadmium Telluride (CdTe) because of its ideal bandgap and high absorption. CdTe is a semiconductor with a direct bandgap, which almost fully absorbs the visible light spectrum within 1  $\mu\text{m}$  thickness. The band gap energy for a bulk CdTe material is  $\sim 1.45\text{eV}$ , which is near the optimum value for single-junction solar cells applications. CdTe solar cells also can be used to make Schottky junction solar cells or can be combined with CdS or CdSe to make p-n heterojunction solar cells. The efficiency record for CdTe solar cells 17.3% was achieved by First Solar company in 2011 (Figure 1.3). However, CdTe solar cells have a down-side in massive long-term distribution: the global supply of Te is limited and Cd is a toxic metal which has been banned in the Europe due to its' formation of unstable compounds.

Thin-films of nanoparticles can be deposited from colloidal solutions and sintered at high temperatures to form a more bulk-like polycrystalline film [6]. In the process of sintering, organic ligands are removed and particles fuse together into clusters and ultimately grains, which change the properties of the material. Quantum confinement in the nanoparticles causes an increase in the band gap relative to the bulk materials and potentially can lead to enhanced impact ionization and multiple excitons [3]. Understanding the transition from quantum confined nanoparticles to polycrystalline film is critical to forming electronic devices with nanoparticles such as solar cells.

#### **4.2.2. Film Preparation**

In our experiment, nanoparticle based CdTe films and solar cells were formed from pyridine capped CdTe nanoparticles dispersed in pyridine. The nanoparticles had a nano-rod shape with initial dimensions of 2nm x 5nm [2]. Films were deposited by spin-casting on glass substrates with a patterned (ITO) transparent electrode, as shown in Figure 4.2. The films were annealed in nitrogen after spin-casting (<10ppm oxygen) at 200°C to remove residual solvents. Sintering was performed by annealing in air at 400°C for 1-10min after treatment with a saturated solution of CdCl<sub>2</sub> in methanol [1,6]. The sintered films were rinsed with 60°C deionized water and immediately dried with dry nitrogen. Solar cell devices were formed with 60nm of aluminum thermally evaporated on the CdTe to form a Schottky junction at the back contact. The Schottky barrier CdTe solar cells had power conversion efficiencies of

up to 5% [2]. An atomic force microscope (AFM) was used to check morphology and thickness of each layer in the device. After sintering for greater than 1 minute the thickness of the film decreases by 10-20% relative to unsintered films. The typical thickness of unsintered films was  $d=300-400$  nm, and the corresponding thickness of sintered films is  $d=250-350$  nm. To eliminate the effect of thickness change on absorption coefficient before and after sintering, all our graphs for CdTe are plotted as  $a*d$ .

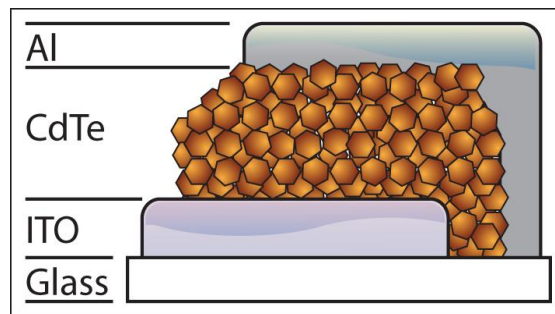


**Figure 4.2:** Device structure of CdTe solar cell.

#### **4.2.3. Sintering Effect on Absorption and Trap States of CdTe**

The density of electronic traps, the band edge and optical absorption all play a dominate roles in determining the device performance of an optical devices including solar cells. Prior to sintering, the nanoparticle film had a band gap of 1.7eV with a very broad band edge as shown on a linear scale in Figure 4.3(a) and a log scale in Figure 4.3(b). The increase in absolute absorption of the CdTe film above the band gap may be due in part to the increases density of the film due to grain growth [7]. After sintering the CdTe films lose their quantum confinement and become

polycrystalline with a bandgap of 1.5eV, consistent with bulk CdTe. The Urbach energy, which is associated with structural and electronic disorder, dramatically drops from 97meV for unsintered films to 30meV for sintered devices (Figure 4.3(b)) as shown in Table 4.1. The large Urbach energy in the unsintered state is more likely due to variations in particle size and shape instead of morphology because the bandgap of 1.7 eV corresponds to quantum confined nanoparticles and not the bulk CdTe bandgap of 1.5 eV.

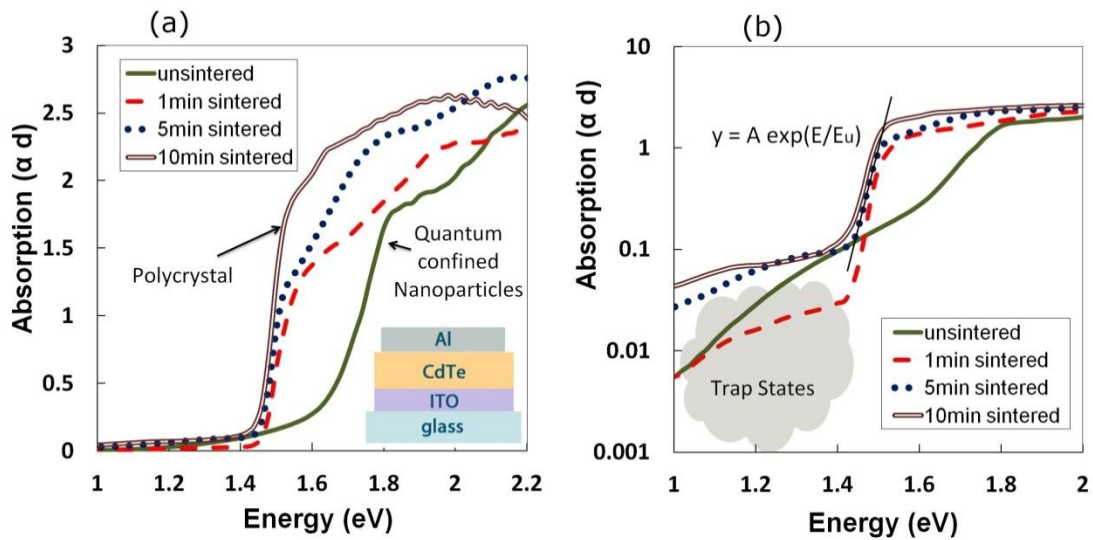


**Figure 4.3: (a) PDS linear graph of absorption vs. energy for unsintered, sintered 1 minute, 5 minutes, and 10 minutes CdTe films. (b) PDS logarithmic graph of absorption vs. energy for unsintered, sintered 1 minute, 5 minutes, and 10 minutes CdTe films.**

During the sintering process, the mid-gap trap density increases as is evident in the increased tail below 1.4eV in Figure 4.3(b) and summarized in Table 4.1 [6]. The low trap density in the nanoparticle films shows that the ligands are effective at electrically passivating the surface of the nanoparticles and the nanoparticles

themselves have a low mid gap trap density. The very large surface area of the porous unsintered nanoparticle films does not appear to introduce more trap states relative to larger, sintered particles [8]. The high temperature  $\text{CdCl}_2$  treatment is necessary to form functional solar cells, stimulate grain growth and doping the CdTe film with Cl [9]. The nanoparticles coalesce during sintering into clusters with random orientation and then form larger domains and grains [10-12]. The grain size in the film grows from less than 10 nm to more than 100 nm in diameter through sintering as shown in Figure 4.4 [13]. The decomposition of the organic ligands after 1min of annealing at 400C is sufficient to eliminate the quantum confinement and the band gap shifts from 1.7eV to 1.5eV with a sharper band edge. This short sintering time is sufficient to destroy quantum confinement but is not sufficient to remove the surface passivation of the nanoparticles or to cause coalescence of the nanoparticle. Therefore, the density of mid gap states remains small in this intermediate semi-sintered state that poses stronger electronic coupling but maintains residual chemical passivation (Figure 4.3(b)). As the sintering process continues, long range order sets in as the nanoparticles form grains with increased crystalline translational periodicity. The formation of the long range translational periodicity of the grain requires that the individual nanocrystallite orientation changes to adapt to the crystalline order of the grain. The transition from short range order (<10nm-crystallites) to longer range order (100nm grains) will induce long range disorder in the crystal lattice such as dislocations and grain boundaries. The long range order does not have the benefit of passivation from the nanoparticle ligands and can therefore form trap state. The

increase in density of unpassivated long-range crystalline defects results in an increase in the mid-gap trap density as reflected the increase in absorption after 5 min. and 10 min. of sintering. In addition, Cl doping during the sintering process will generate deep acceptor sites that increase mid-gap absorption.

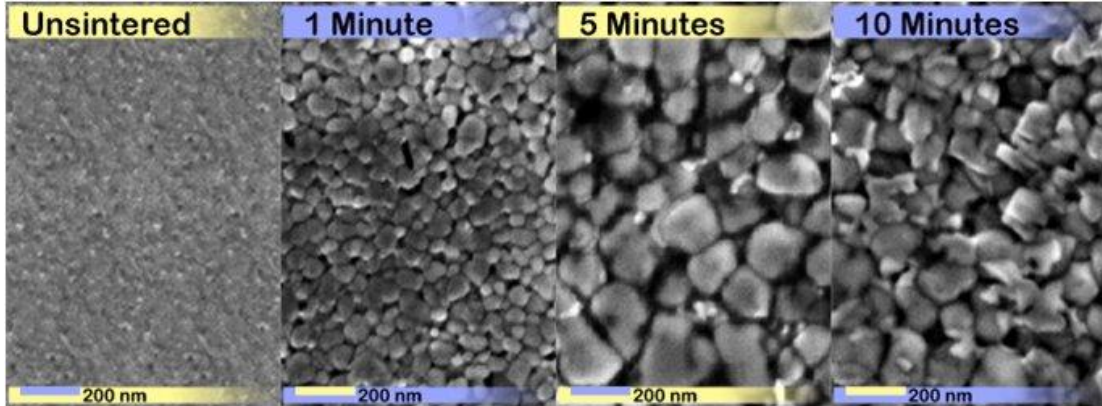


Figure 4.4: SEM images of unsintered, 1min, 5 min, and 10 min sintered CdTe films.

Sintering Time (min)	Band Gap (eV)	Urbach Energy (meV)	Thickness (nm)	Jsc (mA/cm <sup>2</sup> )	Voc (V)	FF (%)	PCE (%)	Jdk @ 0.4V (mA/cm <sup>2</sup> )
0	1.71	97	340	0.068	0.28	29	0.008	0.003
1	1.51	23	310	8.6	0.58	39	1.9	0.004
5	1.5	29	300	24	0.47	42	4.7	0.068
10	1.48	31	270	2	0	0	0	0.150

Table 4.1: Summary of device performance parameters of CdTe solar cell devices discussed in this paper.

#### 4.2.4. CdTe Device Performance

The device performance of Schottky solar cells formed with these films is shown in Figure 4.5 and is summarized in Table 4.1. Untreated and unsintered

nanoparticle films have a short-circuit current density ( $J_{sc}$ ) 400 times less than for the optimally sintered films, while over-sintered films produce high dark currents and no detectable photocurrent or open-circuit voltage ( $V_{oc}$ ).  $V_{oc}$  and fill factor (FF) are also both significantly increased during the sintering process [12,13]. Unsintered CdTe single layer solar cells had a  $J_{sc}=0.068 \text{ mA/cm}^2$ ,  $V_{oc}=0.28 \text{ V}$  and  $FF=29\%$ . After  $\text{CdCl}_2$  treatment and 5 minutes sintering at  $400 \text{ }^\circ\text{C}$  films had a  $J_{sc}=24 \text{ mA/cm}^2$ ,  $V_{oc}=0.47\text{V}$  and  $FF=42\%$ . The efficiency increased from 0.008% to 4.7% However, after 10 minutes of sintering the devices were shunted and no longer showed any photovoltaic energy conversion. With 1 minute of sintering, the band gap of the CdTe films shifts to lower values but optimal device performance is observed with a 5 minute anneal as shown in Figure 4.5 [2].

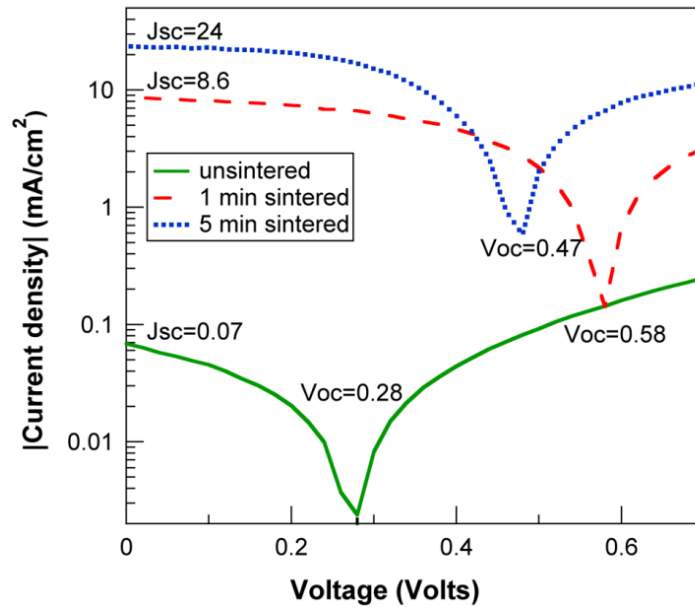


Figure 4.5: J-V curves for ITO/CdTe/Al photovoltaics under AM1.5G, Solid green line is unsintered CdTe film, while dashed line is device sintered for 1 and 5 minutes at  $400^\circ\text{C}$  after  $\text{CdCl}_2$  treatment.

#### **4.2.5. Charge-Extraction Method to Find Trap States of CdTe**

To confirm an increase in the number of trapped charges with sintering time in the device geometry, a simple charge-extraction method [14] was used to probe electronic trap states in the CdTe Schottky junction devices. A voltage near  $V_{oc}$  is applied to the device for several hours in the dark. The voltage is then quickly set to zero and the resulting current transient measured. The RC time constant for these small area devices was less than 1ms, so any current decay measured for times greater than 1ms is due to the discharge of deep level traps in the device. By integrating the transient current over time, an estimate of the total charge trapped in the defects of the cell can be obtained. Charge-extraction measurements yielded a deep level trap density of  $7.17 \times 10^{14} \text{ cm}^{-3}$  for unsintered films,  $1.24 \times 10^{15} \text{ cm}^{-3}$  after 1 minute of sintering, and  $1.84 \times 10^{15} \text{ cm}^{-3}$  after 5 minutes of sintering (Figure 4.6). It is important to note that the trap density measured with charge extraction only includes very deep level traps and not traps near the band edge that have a relaxation time less than 100ms, or less than the RC time constant of the device. Both the charge extraction and PDS methods show an increase in trap density associated with the removal of quantum confinement during sintering.

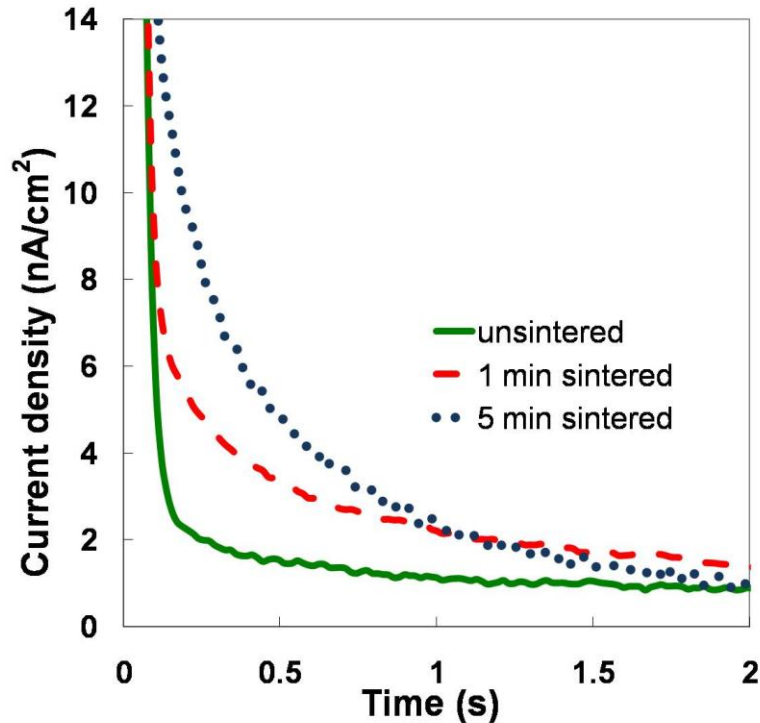


Figure 4.6: Current transient response to charge extraction experiment for CdTe films with different sintering time. Total trapped charge is found by integrating transient over time.

#### 4.2.6. Ligands Effect to Prevent Light Induced Degradation

To further demonstrate that ligands are effective in passivation of traps in nanoparticle films, CdTe films were light soaked using a  $100\text{mW}/\text{cm}^2$  metal-halide light with high UVA content for 1, 18, and 67 hours in air at  $35^\circ\text{C}$ . Changes in absorption and mid-gap trap density were measured before and after light exposure. The UV light destroys ligands in unsintered films but the temperature is low enough to prevent nanoparticle fusion into clusters. Films had minimal grain growth after light soaking as measured with AFM [15,16]. As light soaking time increased, the mid-gap trap density of the unsintered slides dramatically increased (Figure 4.7) due

to the photo-induced degradation of the ligands in the presence of oxygen. This photo-oxidation resulted in the gradual erosion of the nanoparticle-pyridine surface. However, sintered slides with no ligands do not exhibit this strong sensitivity to photo-induced degradation. The traps density was unchanged with 67 hours of light exposure. The ligands are very effective in passivating traps but the passivation effect is not very stable to UV light exposure in air and could represent a long term reliability concern for nanoparticle based solar cells that are not encapsulated [1,17]. The sintered samples have higher conversion efficiency and also a stable trap density with long time exposure to light.

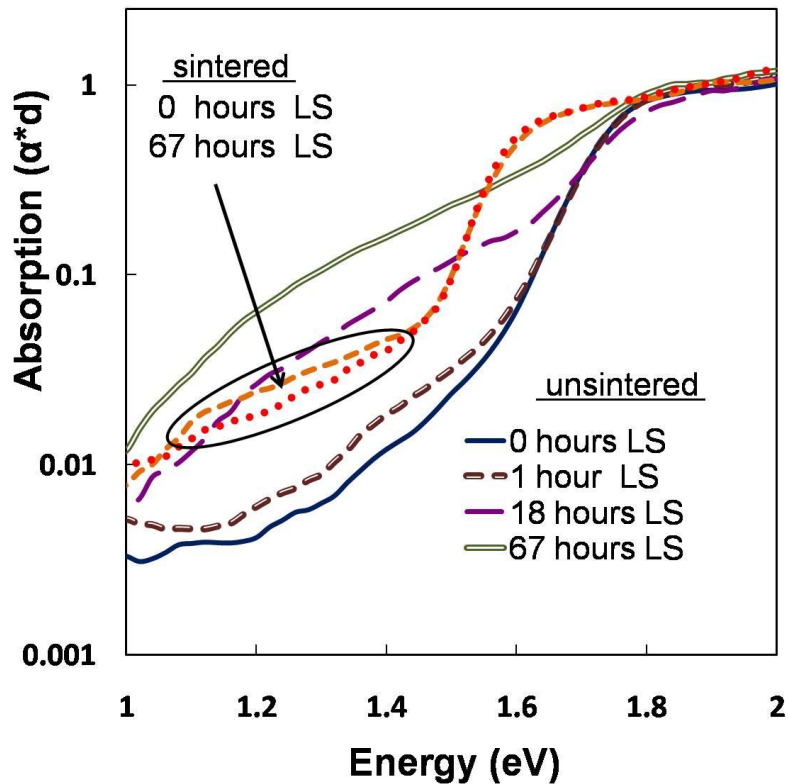


Figure 4.7: PDS logarithmic graph of absorption vs. energy for different light soaking time of unsintered and 5 minute sintered CdTe films.

#### **4.2.7. Conclusion**

We have demonstrated that the density of mid gap trap states is found to be lower in quantum confined CdTe nanoparticle films relative to the sintered polycrystalline films in spite of the higher surface to volume ratio of the nanoparticle films. Solar cell device performance improves substantially with sintering due to higher absorption and improved carrier transport in the sintered polycrystalline films and is not limited by the increase in mid-gap traps. Ligands in nanoparticle based films are very effective at reducing the number of mid-gap trap states in solar cells.

### **4.3. Lead Sulfide Nanoparticles Solar Cells**

The majority of this material was published in the Applied Physics Letters in August 2011 [18].

#### **4.3.1. Background Information**

The band gap of bulk PbS is only 0.4 eV, which is too small to be a good solar cell absorber. The relatively recent synthesis of quantum dots (QD), however, allow the production of PbS quantum dots with a band gap that can be tuned to be in the ideal range for solar cells with the optimal solar spectrum overlap. A position of the optical band gap can vary from 0.5eV up to 1.5eV. By controlling quantum dots size, an absorption wavelength of the first characteristic exciton peak of PbS can easily be tuned and extended over entire an infrared region. A Figure 4.8 shows the absorption spectrum of our PbS nanoparticles film with 4nm QDs size, the excitonic peak at

1030nm (1.205eV), and the band gap of 1.08eV. The smaller bandgap of PbS, as compared with the other absorber materials, makes it a good candidate for tandem solar cells [19].

The excitonic absorption peaks of semiconductor nanoparticles are strongly related with the surface-related charge separation and polarization effects in PbS NPs. The electron–hole pair generated by the light absorption can be easily trapped at the surface defect sites. However, chemically the surface defect sites for the nonradiation recombination of charge carriers can be destroyed by covering the surface with capping materials [20].

The PbS is a narrow gap semiconductor, with a bulk band gap of 0.41 eV, and a large exciton Bohr radius (18 nm). Therefore, the PbS quantum dots band gap  $E_0$  can be tuned over near infrared spectral range. Iwan Moreels [21] in his paper proposed numeric relation between position of band gap energy and quantum dots size:

$$E_0 = 0.41 + \frac{1}{(0.0252 d^2 + 0.283 d)} \quad (4.1)$$

where  $E_0$  is the band gap energy in unit of eV,  $d$  is the QDs size in units of nm and size range between 3.9 nm and 13.3 nm. Then our PbS QDs with average size ~4 nm corresponds to the band gap of 1.06eV. This calculated result is in almost perfect agreement with our measured band gap value with the PDS system in the Figure 4.8.

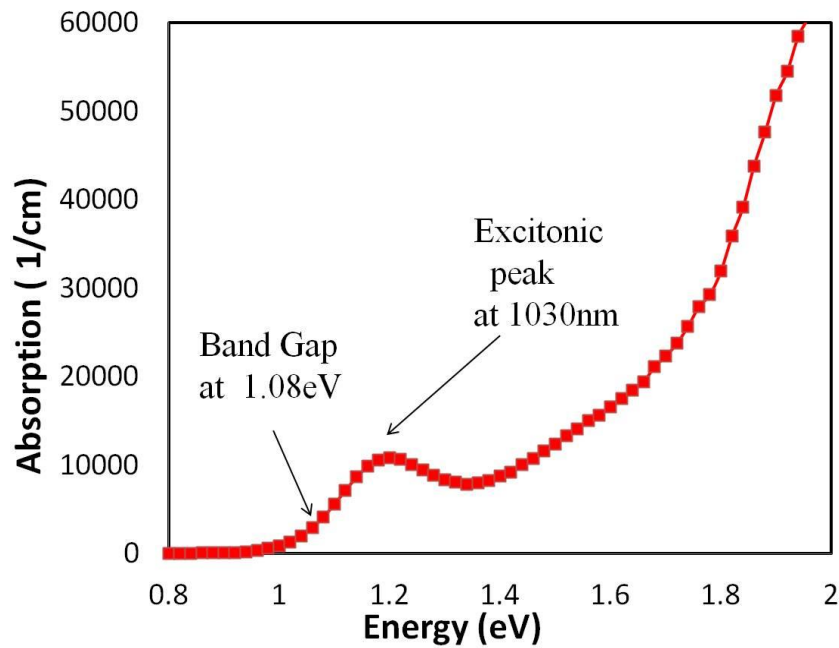


**Figure 4.8: Absorption spectrum of PbS nanoparticles film with EDT ligands. It has an excitonic peak at 1030nm, the nanoparticle size ~4nm, and the band gap of 1.08eV.**

The maximum efficiency of a PbS solar cell has not been verified by any qualified institution, in our lab PbS/TiO<sub>2</sub> solar cells with efficiencies above 4% at room temperature was observed [18]. Although it is still a new field, research on QD solar cells is gaining momentum. Here I will talk about the impact of air and heat exposure on TiO<sub>2</sub>/PbS QD solar cells.

#### **4.3.2. Films Preparation**

For our experiment, the colloidal PbS QDs were provided by Solexant, the TiO<sub>2</sub> sol-gel was made using the standard procedure described earlier [22], and the TiO<sub>2</sub> nanoparticles (NP) were purchased from Solaronix. An approximately 100 nm

layer of planar  $\text{TiO}_2$  was coated by the spun-cast technique on a glass substrate prepatterned with ITO to prevent shorting, followed by a spin-cast nanocrystalline anatase- $\text{TiO}_2$ -layer. Both planar and nanoparticle  $\text{TiO}_2$  layers were sintered at  $450\text{ }^\circ\text{C}$  for 20 min in air to improve conductivity. Next, a layer of PbS quantum dots was deposited on  $\text{TiO}_2$  under nitrogen atmosphere by dip coating between PbS solution in chloroform and hexane mixture and 1,2-ethanedithiol (EDT) in acetonitrile solution. Finally, 100 nm Au was thermally evaporated as the back contact [19]. The devices schematic structure and SEM image are shown in the Figure 4.9 (a) and (b).

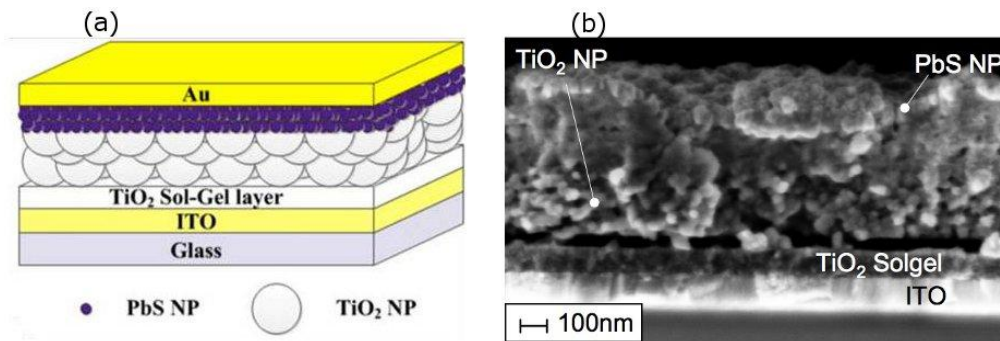


**Figure 4.9:** (a) Schematic of the  $\text{TiO}_2/\text{PbS}$  solar cell structure. (b) SEM image of the  $\text{TiO}_2/\text{PbS}$  solar cell.

In our preparation ethanedithiol (EDT) ligand-exchange treatment is used to cross-link colloidal PbS quantum dots into nanocrystalline film structure with distinct optoelectronic properties. The short EDT cross-linking agents have been used to exchange the long original oleic acids ligands around colloidal PbS nanocrystals, resulting in densely packed nanocrystalline solids with high conductivities. To keep the amount of material the same for both EDT and native ligand, all samples are

single layer. Samples spun from the same solution have the same spin conditions, but thickness and absorption slightly vary depending on whether it is the native ligand or EDT-exchanged.

### **4.3.3. TiO<sub>2</sub>/PbS Device Photo-Oxidation and Degradation and EDT Ligands**

#### **Effect**

Our group demonstrates in the recent paper [18] that five minutes of air exposure of TiO<sub>2</sub>/ PbS (band gap at 1.08 eV) device leads to improve the device efficiency to above 4%, with a substantial increase in Voc and FF; however, air exposure also results in a continuous decrease in Jsc. After 1 hour of air exposure the EQE at longer wavelengths gradually decreases while the peak EQE remains mostly constant, indicating the reduction in current is due to reduced charge collection at the PbS/Au interface. Returning air-exposed devices to the glove box resulted in a transition back to the original values over several hours to days, demonstrating that the short-term air-exposure effect is reversible [18].

Long term air exposure can result in substantial decrease in Jsc; nonetheless, this reduction in Jsc was shown to be partly reversible for all devices studied by soaking the device in EDT solution, the same solution used in the ligands exchange, as shown in the Figure 4.10. EDT in the solution improves conductivity, since the ligands exchange has the strong impact on the overall mobility [23]. However, no changes were observed in the Fourier transform infrared spectrum measured before

and after EDT and air exposure, suggesting that bulk changes in the EDT ligands are not occurring.

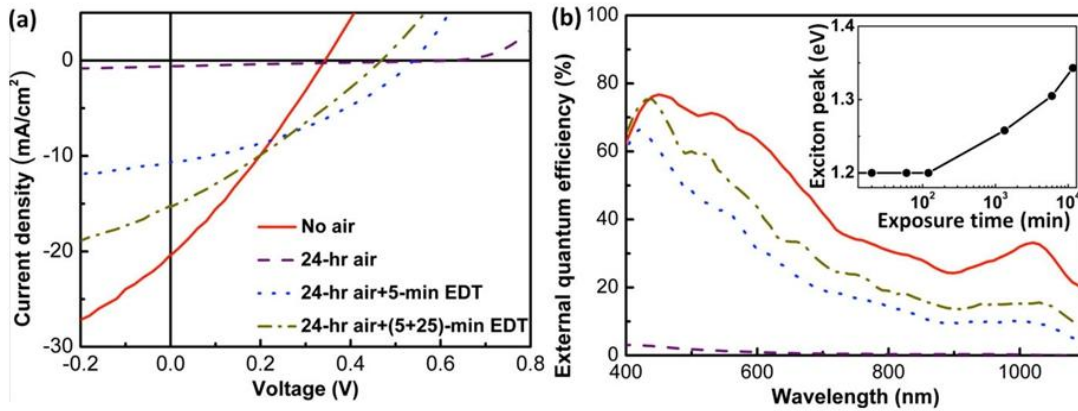


**Figure 4.10: (a) J-V characteristics for a TiO<sub>2</sub>/PbS (1.1 eV) device under 100 mW/cm<sup>2</sup> AM1.5 illumination before and after 24-h air exposure and subsequent 5 and 30-min of EDT soak. (b) EQE spectra for the corresponding device. Inset: the change in the exciton peak extracted from absorption data with air exposure time.**

Possible explain of this effect is that the oxygen in air mainly affects the PbS layer when the devices are exposed to air. Oxygen is expected to create acceptor states on the PbS QD films [24, 25]. The creation of these acceptor states results in the shifting of PbS's Fermi level towards the valence band, which causes bigger energy band bending and resulting improved rectification and Voc. This result is supported by the PDS data presented in Figure 4.11, where the sample's exposition to air for 2 months causes the expected blue shift of the band gap energy. However, acceptor doping is inconsistent with the rapid decrease in the dark current observed. An alternative explanation is that the air exposure reduces electron mobility as oxygen is a known electron trap. Since the red photons are absorbed much further

from the transparent electrode than the blue photons, the lower mobility electrons generated near the Au interface will not be as efficiently collected at the TiO<sub>2</sub> interface.

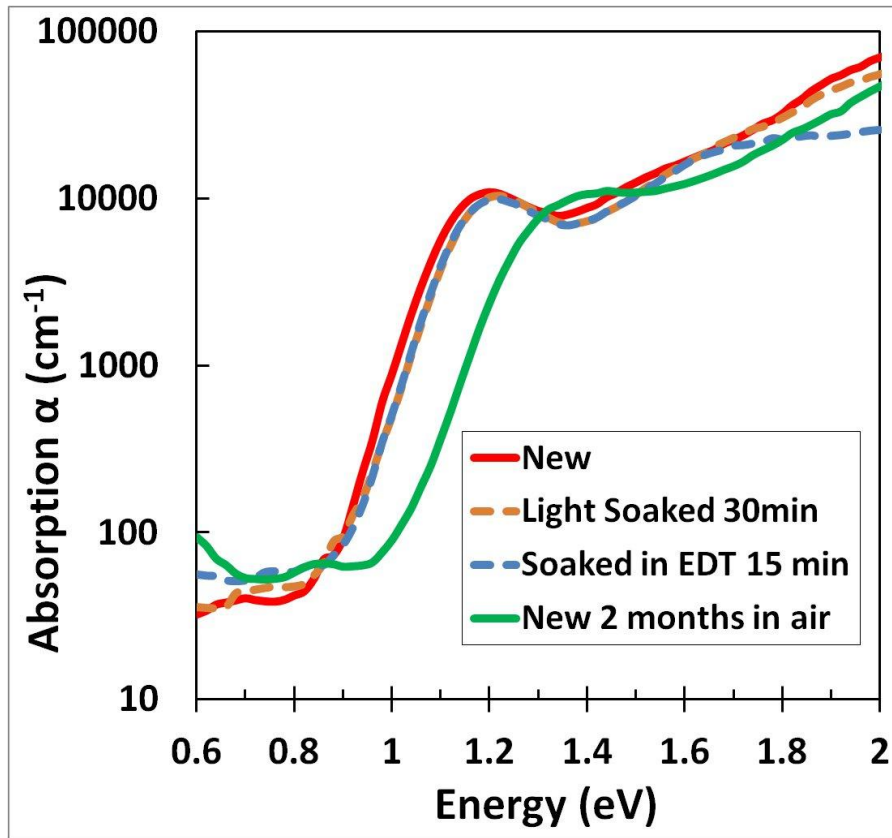


Figure 4.11: The photothermal deflection spectra of PbS QD film before air exposure and after 2 months air exposure, 30-min aggressive oxidation in air by light soaking in 100 mW/cm<sup>2</sup> of AM 1.5 light, followed by a subsequent 15 min of EDT soak.

Zhao and Klem suggest [23, 26] that EDT can remove and/or transform the formed insulating layer on the PbS surface which can explain the EDT soaking effect that we observed; however, the removal of this oxide does not result in the recovery of the QD size, i.e., the QDs become increasingly smaller and less conductive. These

results are supported by the PDS data presented in Figure 4.11. For the PDS measurements, the sample was soaked in air for 30 min under a more aggressive AM1.5 illumination, instead of the indoor fluorescent light, to accelerate the degradation process. The aggressive exposure of the device to light soaking in air causes the expected increase in the band gap energy, resulting in excitonic blue shifts in absorption and emission spectra [27]. However, subsequent exposure to EDT does not affect the bandgap energy, indicating that the EDT only dissolves away the insulating shell and does not rebuild the QD size to its pre-oxidation state. Subsequent exposures to oxygen and EDT will lead to increasingly smaller QDs and eventually device failure, as is observed. The PDS data taken within the bandgap also reveal that the mid-gap states, and therefore the doping, are not substantially impacted by air exposure or EDT treatment.

#### **4.3.4. Annealing Effect**

Commercial photovoltaic modules must pass demanding environmental stability tests, so-called 85/85 damp heat tests, which including 1000 hours soaks at 85°C and 85% relative humidity. For our purpose, we stress PbS devices stability and degradation over broad range of elevated temperatures (60°C, 120°C, and 180°C) in air free environment. It is evident from the Figure 4.12 that higher temperatures dramatically change properties of the films.

After annealing at 60°C the total absorption of PbS film reduces, the trap density increases, but the excitonic peak of QDs does not shift or change shape.

Therefore the lower temperature annealing does not change QDs size and does not affect on the total confinement of the system. The possible explanation of the changes in the trap states may come from EDT ligands relaxation or desorption of EDT molecules [27]. The EDT ligands are effective at electrically passivating the surface and contribute to the low trap density in the nanoparticle films. However, at high temperatures the decomposition is impacted by EDT ligands' attachment to PbS nanoparticles, which causes the trap density increase and drop of the total absorption of the PbS film. Surprisingly, the performance of PbS devices is not affected much by heating below 100°C:  $J_{sc}$  increases,  $V_{oc}$  decreases, and overall fill factor stays almost the same.

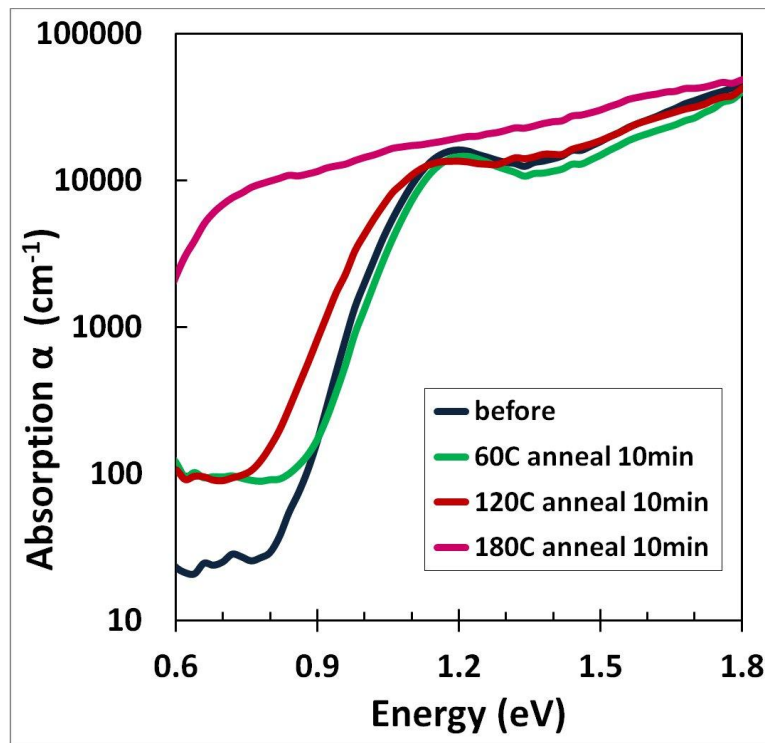


Figure 4.12: Absorption coefficient of PbS QDs film before and after annealing at 60°C, 120°C, and 180°C in glove box.

Annealing at temperatures higher than 100°C immediately degrades devices, and nanoparticles films start to behave more like a bulk material, as expected. After annealing a PbS nanoparticles film at temperatures higher than 120°C the excitonic peak disappears, the band gap shifts to lower energies, and the trap states increases radically, as shown in the Figure 4.12. At high temperature PbS nanoparticles start to melt into bulk state, which band gap is ~0.4eV. The observed temperature dependence of band gap energy is consistent with previously seen band gap position dependence from NPs crystallite size [21].

#### **4.3.5. Conclusion**

Our results confirm that there is a strong relationship between the structural and optical properties of PbS NP films. We show that using 5 min of air exposure improves the PbS/TiO<sub>2</sub> device efficiency to above 4% and small changes in environmental conditions can cause significant impact in the conclusions drawn, calling into question the helpfulness of reporting results without careful consideration of the environmental conditions.

#### **4.4. References**

- 1) I. Gur, N. A. Fromer, M. L. Geier, and A. P. Alivisatos, *Science* **310**, 462 (2005).
- 2) J. D. Olson, Y. W. Rodriguez, L. D. Yang, G. B. Alers, and S. A. Carter, *Appl. Phys. Lett.* **96**, 42103 (2010).

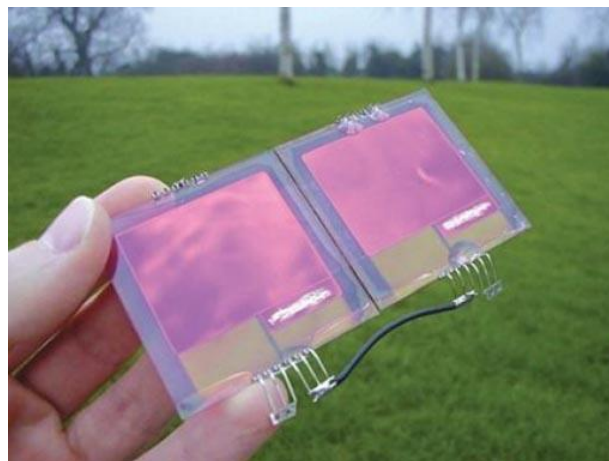
- 3) J. Luther, M. Law, M. Beard, Q. Song, M. Reese, R. Ellingson, and A. Nozik, *Nano Lett.* **8**, 3488 (2008).
- 4) J. Clifford, K. Johnston, L. Levina, and E. Sargent, *Appl. Phys. Lett.* **91**, 253117 (2007).
- 5) A. Bezryadina, C. France, R. Graham, L. Yang, S. A. Carter, and G. B. Alers *Appl. Phys. Lett.* **100**, 013508 (2012).
- 6) I. E. Anderson, A. J. Breeze, J. D. Olson, L. Yang, Y. Sahoo, and S. A. Carter, *Appl. Phys. Lett.* **94**, 063101 (2009).
- 7) S Ringel, A. Smith, M. MacDougal, A. Rohatgi, *J. Appl. Phys.* **70**, 881 (1991).
- 8) C. B. Davis, D. D. Allred, A. Reyes-Mena, J. González-Hernández, O. González, B. C. Hess, W.P. Allred, *Phys. Rev. B* **47**, 13363 (1993).
- 9) V. Komin, B. Tetali, V. Viswanathan, S. Yu, D. Morel, C. Ferekides, *Thin Solid Films* **431-432**, 143 (2003).
- 10) N. Baier, A. Brambilla, G. Feuillet, S. Renet, *Nucl. Instrum. Meth. A* **563**, 155 (2006).
- 11) B. McCandless, L. Moulton, and R. Birkmire, *Prog. Photovoltaics* **5**, 249 (1997).
- 12) L. Yang, to be published.
- 13) S. Lalitha, R. Sathyamoorthy, S. Senthilarasu, A. Subbarayan, *Sol. Energ. Mat. Sol. C.* **90**, 694 (2006).
- 14) B. O'Regan and J. Durrant, *J. Phys. Chem. B* **110**, 8544 (2006).
- 15) M. Crisp and N. Kotov, *Nano Lett.* **3**, 173 (2003).

- 16) F. Aldeek, L. Balan, G. Medjahdi, T. Roques-Carmes, J. Malval, C. Mustin, J. Ghanbaja, R. Schneider, *J. Phys. Chem. C* **113**, 19458 (2009).
- 17) Y. Zhang, L. Mi, J. Chen, and P. Wang, *Biomed. Mater* **4**, 012001 (2009).
- 18) G. Zhai, A. Bezryadina, A. J. Breeze, D. Zhang, G. B. Alers, and S. A. Carter *Appl. Phys. Lett.* **99**, 063512 (2011).
- 19) T. Ju, Rebekah L. Graham, G. Zhai, Y. W. Rodriguez, A. J. Breeze, L. Yang, G. B. Alers, and S. A. Carter, *Phys. Lett.* **97**, 043106 (2010).
- 20) Y. Zhou, H. Itoh, T. Uemura, K. Naka, and Y. Chujo, *Langmuir* **18**, 5287 (2002).
- 21) I. Moreels, K. Lambert, D. Smeets, D. De Muynck, T. Nollet, J. C. Martins, F. Vanhaecke, A. Vantomme, C. Delerue, G. Allan, and Z. Hens, *ACS Nano* **3** (10), 3023 (2009).
- 22) A.C. Arango, L. R. Johnson, V. N. Bliznyuk, Z. Schlesinger, S. A. Carter, and H.-H. Hoerhold, *Adv. Mater.* **12**, 1689 (2000).
- 23) E. J. D. Klem, H. Shukla, S. Hinds, D. D. MacNeil, L. Levina, and E. H. Sargent, *Appl. Phys. Lett.* **92**, 222105 (2008).
- 24) H. Zarghami, Y. Liu, M. Gibbs, E. Gebremichael, C. Webster, and M. Law, *ACS Nano* **4**, 2475 (2010).
- 25) K. S. Leschkies, M. S. Kang, E. S. Aydil, and D. J. Norris *J. Phys. Chem. C* **114**, 9988 (2010).
- 26) N. Zhao, T. P. Osedach, L.-Y. Chang, S. M. Geyer, D. Wanger, M. T. Binda, A. C. Arango, M. G. Bawendi, and V. Bulovic, *ACS Nano* **4**, 3743 (2010).
- 27) R. Ihly, J. Tolentino, Y. Liu, M. Gibbs, and M. Law, *ACS Nano* **5** (10), 8175–8186 (2011).

# **CHAPTER 5:**

## **ORGANIC POLYMERS**

### **SOLAR CELLS**



The majority of this chapter will be published in a recent paper in 2012.

## **5.1. Introduction to Organic Photovoltaics**

Rapid evolution in the field of organic, hybrid and dye sensitized solar cells took place in the last couple decades. Although efficiencies reported are still too low to compete with Si and CdTe solar cells, the polymer and organic solar cells present the greatest potential in terms of cost, scalability, low-weight, environmental impact, and easy-to-produce solar cells. A fundamental difference between solar cells based on organic materials and conventional inorganic photovoltaic cells is that light absorption results in the formation of excitons in molecular materials, rather than in free electrons and holes. An exciton in an organic semiconductor can be considered as a tightly coulombically bound electron hole pair. Due to its electrical neutrality and the strong binding energy between the hole and the electron it can be regarded as a mobile excited state.

Compare to other thin technology organic photovoltaics also present the most complex selection of degradation phenomena. The active layer component in the organic solar cell is the part of the device that is very prone to degradation and since it is integral to the device functionality this translates directly into a degradation of the power conversion efficiency. Several types of degradation of organic photovoltaic devices typically occur:

- photo-oxidation and photo-bleaching of the organic solid, leading to loss in conjugation and irreversible deterioration of the light-absorbing or charge-transporting properties (photocurrent);
- degradation of the conductive properties of the interfaces of the organic device;
- physical degradation / mechanical disintegration, for example, by the segregation over time of the donor and acceptor components in a bulk heterojunction structure.

One of the most important reactions is photo-degradation with or without oxygen. In this work PDS is primarily used to characterize organic thin films and to quantify degradation due to light, air and temperature exposure. We investigate the sub-bandgap absorption spectra of 3 different polymers: P3HT Poly(3-hexylthiophenes), MEH-PPV Poly[2-methoxy-5-(2-ethylhexyloxy)-1,4-phenylenevinylene, PF Red polyfluorene Dow Red F, which are primarily used in solar cells, light emitting diodes (LED), and field-effect transistors. These small changes in the sub-bandgap absorption coefficients could improve the understanding of possible charge transfer processes, charge carrier generation mechanisms, transport processes and how they are influenced by the presence of defects that can act as possible trapping or recombination centers and lead to degradation of cells.

## **5.2. Sample Preparation and Experimental Setup**

Three polymer solutions in 1,2-dichlorobenzene were mixed and stirred over night: a 1.5% by wt. of P3HT (Poly(3-hexylthiophenes)), a 1% of MEH-PPV( [2-

methoxy-5-(2-ethylhexyloxy)-1,4-phenylenevinylene), and a 1-2.5% of polyfluorene PF Red (polymer red spr-001-L010 from Merck). Their molecular structure is shown in Figure 5.1. The polymers films were prepared by spin casting solution on to a glass substrate in air and annealing in a vacuum oven for 1 hour to remove oxygen. The P3HT and MEH-PPV samples were annealed at 110-115°C and the PF Red sample was annealed at 90°C.

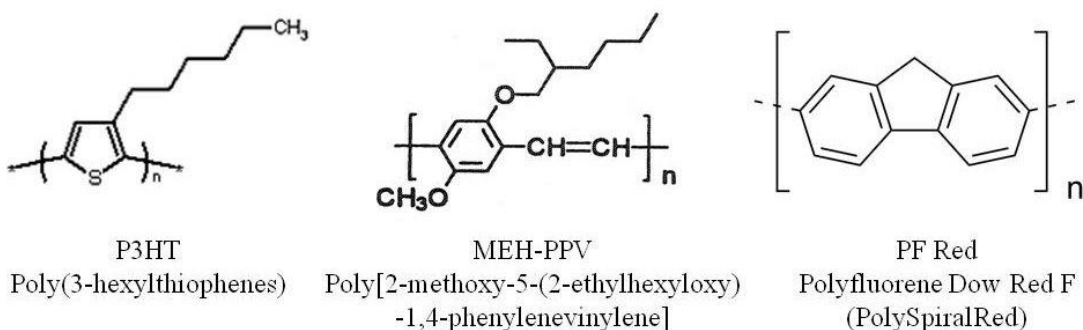


**Figure 5.1: Molecular structure of P3HT, MEH-PPV, and PF Red (PSR) materials.**

The average thickness of the MEH-PPV film is 350nm, the P3HT thickness is 150nm, and the PF Red thickness is 250nm, which were measured by an Atomic Force Microscope (AFM) after optical measurements. After annealing the films were covered with a foil and moved to a vacuum chamber for 20-30 minutes and then to a glove box for 1 hour to eliminate water, air, and light exposure. It has been observed that the doping effect of oxygen and air without light present was reversible in a vacuum chamber [1-4]. So keeping the films in the vacuum chamber should reduce any effect of air exposure during transport of the samples from a vacuum oven to the glove box, where they are sealed. The films for PDS measurements were broken on

pieces 5mm\*15mm, vacuum sealed inside conflate flanges in pairs for future PDS and transmission spectrometer measurements, and covered with an aluminum foil to eliminate light exposure between the measurements.

During setup for PDS measurements, the film is exposed to air for approximately 5 minutes before immersing in a quartz container with an electrolyte liquid ( $C_6F_{14}$ ). For organic samples perfluorohexane  $C_6F_{14}$  is used as a deflection medium in PDS instead of  $CCl_4$ , which is commonly used for amorphous Si and nanoparticle based thin films.  $C_6F_{14}$  does not dissolve the polymer films and is less toxic, but it also dissolves oxygen from the air to a higher concentration than is found in other liquids [5]. We cannot neglect possible effects of dissolved oxygen in  $C_6F_{14}$  on polymers' degradation measurements and should take it in consideration. However, each polymer film is exposed to similar levels of contamination from the test procedure; we can safely assume that the contamination is less than our lowest measurement.

### **5.3. Spectral Absorption Analysis of Three Polymers**

The spectral dependence of the absorption coefficient  $\alpha(E)$  of polymers measured by PDS is shown on a logarithmic scale in Figure 5.2. By using PDS, we were able to measure  $\alpha$  over 5 decades, revealing sub-bandgap features of P3HT, MEH-PPV, and polyfluorene PF Red and identifying their spectral regions.

*Band gap absorption region:* Absorption above the bandgap, measured by transmission spectrometer, determines the portions of the solar spectrum that is converted to electron-hole pairs.

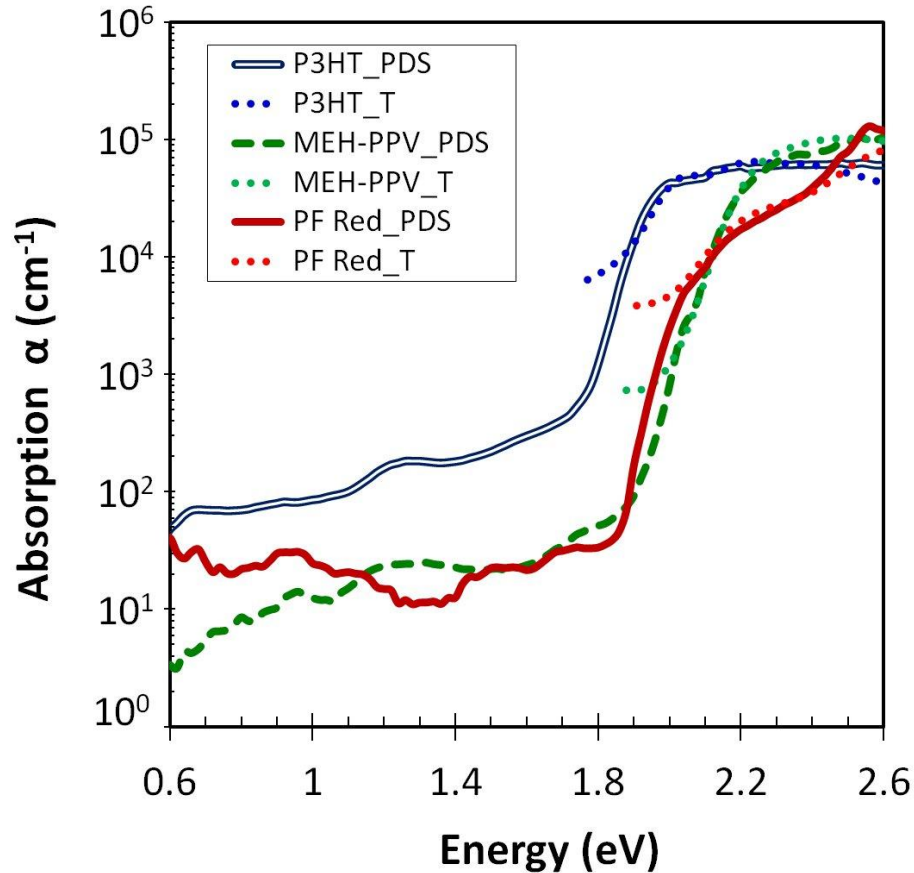


**Figure 5.2:** Absorption vs. energy of P3HT, MEH-PPV, and polyfluorene PF Red (solid line: PDS spectrum; dot line: Transmission spectrum).

*Exponential absorption region:* The region just below the optical band gap absorption determines mid-gap transitions of materials. Similar to thin films, a polymer's structural disorder is quantified by using the Urbach energy from equation (2.11). The polymer's exponential slope coefficient doesn't define crystallinity and

lattice order in a same way as silicon, but for a classification purpose of the polymer's structural order we use the same terminology. P3HT has a bandgap of 1.9 eV and an Urbach energy of 43meV, and polyfluorene PF Red has a bandgap of 2.05eV and an Urbach energy of 44meV, and MEH-PPV has a bandgap absorption of 2.15eV and an Urbach energy of 35meV.

*Band tail region (1.35 eV–1.7eV for P3HT, 1.5eV-1.9eV for MEH-PPV, and 1.1eV-1.9eV for PF Red):* The polymers have an absorption tail, due to transitions originating from the tail of localized states of the DOS distribution that can contribute to carrier recombination and reduced carrier lifetime. The exponential slopes of the tail are 360meV for P3HT and 280meV for MEH-PPV, which results from the band tail contributions from the valence and the conduction band of the polymers. By looking on changes in absorption in the sub-bandgap region, we inspect deep defect transitions inside the energy gap and the trap states responsible for the long-term degradation.

Several experimental and theoretical studies have been made before, which discuss the mechanism of photo-generation of free charge carriers in organic semiconductors. The Goris paper [6] indicates that excitons are the primary photo-excitations in conjugated polymers and that, subsequent to their formation, excitons exhibit a random walk within an energetically and spatially disordered array of hopping sites to eventually dissociate into pairs of free charge carriers at a charge transfer state, an impurity or a defect.

*Sub-bandgap shoulder region at 1.25 eV (1.05eV-1.4eV):* P3HT and MEH-PPV have a broad sub-bandgap absorption shoulder, which is due to polaronic species present in the material, which originate from a residual doping of the polymer attributed to its synthesis and the storage history [6]. Polyfluorene doesn't have the sub-bandgap absorption shoulder.

*0.6–1.05eV region:* In our work we don't see any strong characteristics' spectral peaks for MEH-PPV and P3HT at this region, which correspond to vibrational overtones of C-H stretching and bending vibrations and which we observed in previous PDS-studies of PPV of organic materials [6,7]. However, PF Red has several peaks at 0.65eV and 0.95eV. This difference between our PDS results and previous results [6,7] is surprising since our PDS setup has the same or even better sensitivity in absorption measurements. This discrepancy may come from few reasons: polymers' storage history before spin-casting on films, the films preparation methods, usage of different electrolyte liquids for PDS experiments ( $C_6F_{14}$  instead of Fluorinert FC75), and bubbling through the Fluorinert with He or Ar to reduce oxygen concentration.

#### **5.4. P3HT Thermal and Photo-Degradation**

P3HT is a common polymer which has high carrier mobility, mechanical strength, thermal stability and compatibility with fabrication process and which is commonly used in heterojunction solar cells. However, P3HT photovoltaic devices' performance degrades when exposed to air and high humidity: decrease of mobility

and on/off ratio, degradation of saturation behavior, positive threshold–voltage shift and increase of sub threshold swing are typical [8].

In the process of annealing, the P3HT crystallinity and the P3HT crystallite size changes with a maximum for the annealing temperature at 125C. Further increase of the annealing temperature leads to decrease of the P3HT crystallinity, which results in melting of the P3HT crystallites and therefore in reduced the P3HT crystallinity [9]. To investigate the mid-gap trap states changes in the process of annealing and crystallization of P3HT, the absorption with PDS spectrometer was measured for a fresh not annealed P3HT film, and then annealed in a glove box for 25 min at 115C, and then again annealed for 10min at 140C as shown in a Figure 5.3. With annealing the mid-gap trap states decrease drastically by a factor of 2, which is illustrated by reducing the absorption in a characteristic energy between 1.2-1.8eV in the Figure 5.3. This decrease in the trap states is due to a structural change and removing water in the process of annealing in the glove box, which effects can't be distinguished in our experiment. These measurements support an idea of increasing charge mobility due to decrease of traps states since during annealing P3HT forms crystalline fibrils, which may result in an increase of both the quantum yield of charge carrier pair formation and the total charge carrier mobility [10]. Due to formation, it could be argued that crystallization of the P3HT chains enhances the exciton diffusion length, resulting in an increase of the total charge carrier mobility. This increase in the mobility of the charge carriers may be the cause of the increased photoconductivity of P3HT [10].

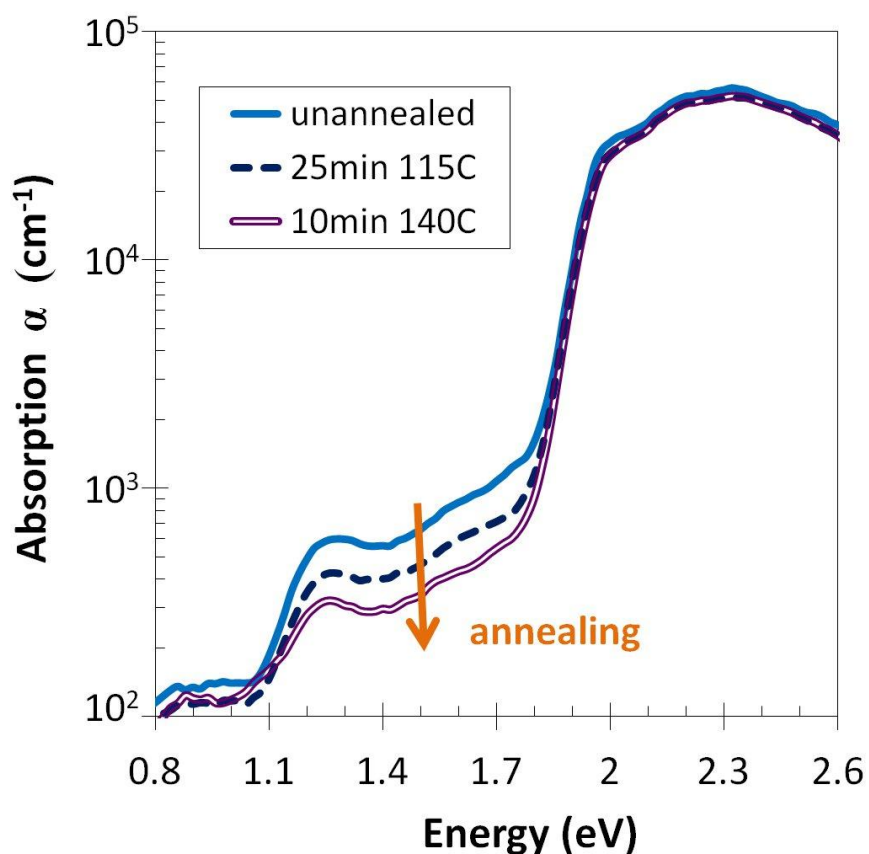
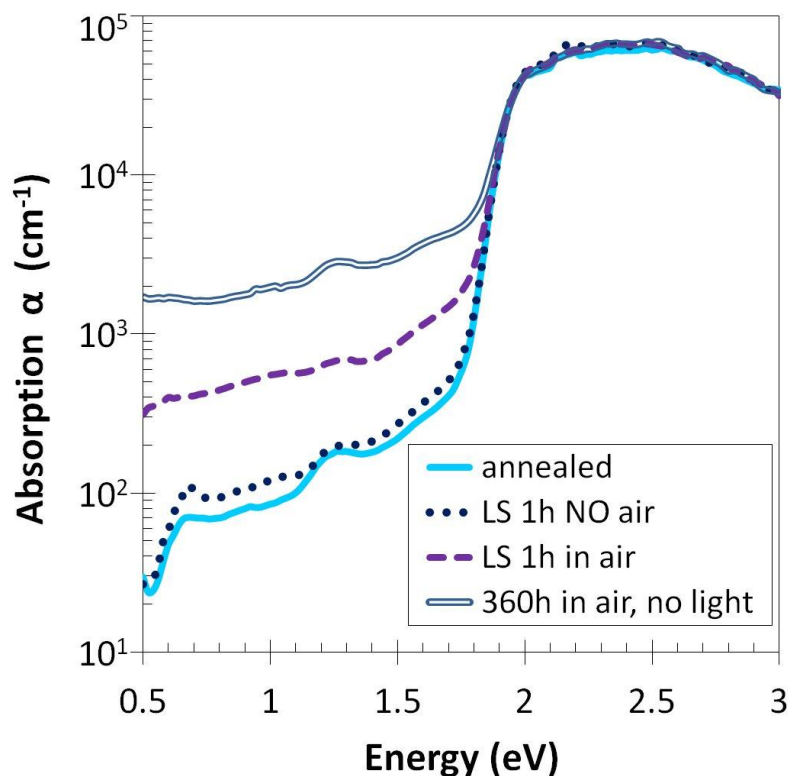


Figure 5.3: PDS measurement of absorption vs. energy for P3HT thin film in the process of annealing. Not annealed fresh film (blue line), annealed for 25 minutes at 115C (dark blue dash line), additional annealing of the film for 10 min at 140C (violet double line).

To investigate the effect of air and light on the degradation of P3HT, films were annealed for 1 hour in a vacuum oven at 110°C P3HT, then measured with the PDS system before and after light soaking for 1 hour under 100W/cm<sup>2</sup> illumination from a metal-halide light with high UVA content at 35°C inside and outside of a vacuum sealed conflate flange. (Figure 5.4) Without air exposure the mid-gap trap states of P3HT are not significantly impacted after 1 hour of light soaking. The band tail region 0.6eV-1.1eV of P3HT is slightly affected more than absorption at 1.1eV-

1.7eV region which is due to induced structural changes in the polymer itself and alters its properties, thereby causing the degradation of the device. However, when the P3HT film was exposed to light with air for only 1 hour, the mid-gap states increased more than 3 times. After exposing the P3HT thin film to air without light illumination for 360 hours, the mid-gap trap states increased only 4 times more than after exposure to air under 1 sun ( $100\text{W}/\text{cm}^2$ ) for an hour, as shown in the Figure 5.4.

Combination of air and light destroyed the P3HT films permanently, which supports Chang hypothesis [1]. In his paper Chang [1] argued that when P3HT is exposed to light in atmosphere, a charge interaction between P3HT molecules and oxygen (or water) molecules would have a good chance to be triggered and then followed by the formation of stable dopants. However, when P3HT is processed in an atmosphere without exposure to white light, the oxygen molecules could only diffuse and form a weak  $\text{P3HT}^+-\text{O}_2^-$  complex, which in turn can be removed by placing P3HT film in a vacuum chamber [1]. So air by itself degrades P3HT films less rapidly and degradation can be reversed by placing them in vacuum. The initial reversibility of the formation of charge transfer complexes between oxygen and P3HT in the dark was also demonstrated by ESR studies, which showed that after illumination with oxygen P3HT:PCBM buildup charges which can be reversed in vacuum [11].



**Figure 5.4: Absorption vs. energy of annealed P3HT film in process of exposure to light and air. Fresh annealed film (light blue line), light soaked for 1 hour without air film (dark blue dot line), light soaked for 1 hour in air film (violet dash line), exposed to air for 360 hours in dark film (dark blue dot line).**

Manceau in his papers [12,13] reports a dual chemical mechanism which account for the solid state photodegradation of P3HT. By the first mechanism, oxidation of the thiophene ring has been proposed to be induced by singlet oxygen  $O_2(1Dg)$  (referred to as  $^1O_2$ ), as shown in Figure 5.5 [14]. By energy transfer from the triplet excited state of P3HT,  $^1O_2$  can be obtained, then it can undergo a 1,4 Diels–Alder addition to the thienyl units and eventually can form an unstable endoperoxide. This species would then decompose into carbonyl, olefinic and sulfine

derivatives, while breaking the macromolecular backbone. This disturbs the p-conjugation and hence decreases the UV-visible absorbance. Moreover, the reaction of P3HT with  $^1\text{O}_2$  causes polymer photobleaching; however, the presence of a quencher, such as anthracene, reduces the rate of P3HT degradation [12]. The second mechanism involves a side chain oxidation by ground state oxygen starting with a hydroperoxide formation at the benzylic position, as shown in Figure 5.5 [11]. The oxidation proceeds via a free-radical chain reaction route, thus forming carbonyl and hydroxyl adducts, and may include cross-linking [12]. Ljungqvist [15] suggested that the thermooxidation degradation of poly(3-octylthiophene) (P3OT) involves an identical radical mechanism, supporting the idea that  $^1\text{O}_2$  is not involved in the side-chain oxidation.

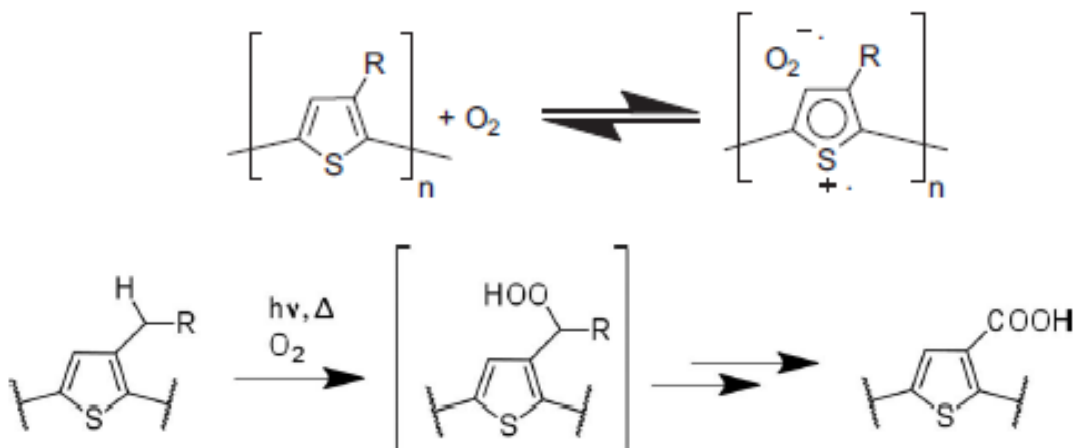


**Figure 5.5: Photo-oxidation mechanism according to Manceau paper.**

So the simple illumination of a material with light, especially with the UV light component, leads to the breaking of chemical bonds with the removal of one or

more electrons. The process can also occur by reacting polymer with a reactive oxygen species such as a hydroxyl radical (-OH), ozone or hydrogen. Water enhances carrier conduction in the active-layer surface caused by the relatively large dipole momentum of water molecules, rather than the p-type doping effect of O<sub>2</sub> [8]. Ozone forms a complex with polythiophene and shallow acceptor [16]. In these PDS measurements sources of the P3HT performance degradation by exposing to air and light are not distinguished separately between effects of oxygen, water, or ozone in air. So our PDS results most likely have combination of several effects.

## **5.5. Polyfluorene Red Degradation**

Polyfluorene is a very attractive conjugated polymer for organic light emitting diodes (LED), field-effect transistors, and plastic solar cells due to its high photoluminescence and electroluminescence efficiencies, low stimulated emission thresholds and exceptionally high fluorescence quantum yields (0.6–0.8) in thin solid films. [17,18] Polyfluorene has high thermal, chemical, and oxidative stability.

In our experiment we use PolySpiralRed is a red-emitting polyfluorene (Dow Red F polyfluorene). Fresh PF Red thin films were kept in a dark and measured after 2 hours and 1 week of air exposure. The air exposure of PF Red thin film without light does not significantly impact the mid-gap states (Figure 5.6(a)). PDS graphs of absorption have slight variation of trap density and band gap of PF Red polymer, which is due to a variation of concentration of PF Red in a spin-cast solution. With increasing the concentration of the PF Red solution from 1% to 2.5%, the band gap

has a red shift by 0.1eV and the trap states decreased by ~20%. Fresh and exposed for 1 week to air the PF Red thin films have exactly same preparation and thickness and exhibits almost no changes in the trap density and the Urbach energy values; however, the total absorption drops after exposing the PF Red film to air.

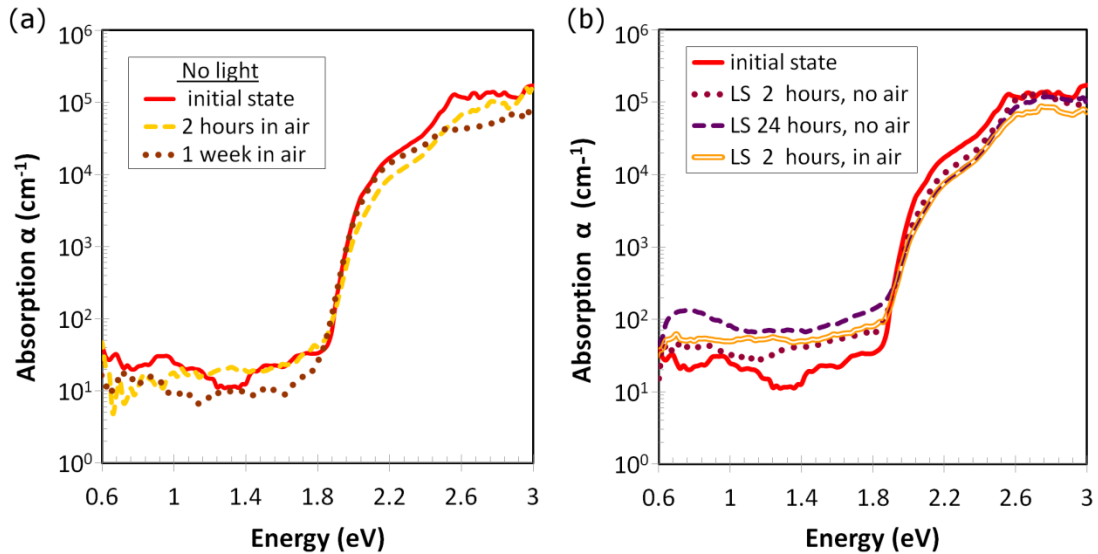


**Figure 5.6: (a) Absorption vs. energy of PF Red in the process of exposure to air without light: initial state (red line), 2 hours in air (yellow dash line), 1 week in air (brown dot line). (b) Absorption vs. energy of PF Red in the process of light soaking under 100W/cm<sup>2</sup> from a metal-halide light with and without air exposure: initial state (red line), light soaked for 2 hours without air (claret dot line), light soaked for 24 hours without air (purple dash line), light soaked for 2 hours in air (orange double line).**

In the presence of oxygen and light, polyfluorene undergo decomposition, which is characterized by a reduction of both an excitonic (isolated chromophore) and an excimer (aggregate) emission bands. The exciton band decreases more rapidly so that the exciton to excimer ratio decreases in time [19]. To investigate degradation of dyes in polyfluorene, the PF Red thin films were light soaked under 1 sun of a metal-

halide light with and without air exposure and measured with the PDS system. After 2 hours of light soaking the PF Red film in a conflate flange without air exposure the mid-gap trap states doubles, and after 24 hours of light soaking without air the trap states increases by a factor of 4, as shown in Figure 5.6 (b). Upon longer exposure, the excimer band decreases faster and the ratio of exciton to excimer emission increases [19]. However, after exposure the PF Red thin film to air and light together for 2 hour, the mid-gap trap states increase by a factor of 2.5 and then the photobleaching effect start to dominate in the thin film (Figure 5.6(b)). Polyfluorene films undergo photoinduced degradation, the amount of the dye chromophores decrease and the total absorption of the film is reduced. Predominantly, the absorption is observed by the fluorene units, as might be expected for materials containing only low amounts of the dye chromophores in the absence of energy transfer from the fluorenes to the dyes [20]. After 24 hours of light soaking in air the PF Red thin film becomes transparent. The polyfluorene PF Red degrades much faster in combination of air and light and this degradation is irreversible.

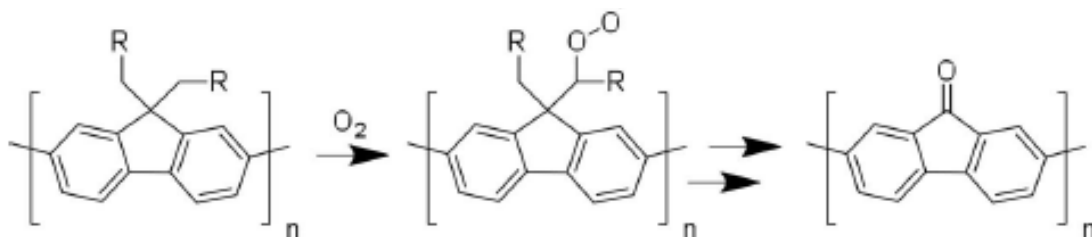


**Figure 5.7: Proposed general degradation mechanism for fluorene containing polymers.**

Grisorio [21] studied the mechanism of degradation in more detail and proposed a stepwise process starting with the side chain oxidation adjacent to the 9-position in the substituted fluorene, as shown in Figure 5.7 [11]. According to his study the fluorenone formation is so energetically favored that no matter what kind of substitution is chosen for polymers, this degradation route will predominate for fluorene containing polymers.

## **5.6. Air Stability of MEH-PPV, P3HT, and Polyfluorene Red**

Finally we compare stability of three polymers (MEH-PPV, P3HT, PF Red). By previous work light stability of these materials and chemical degradation was mostly understood. The earlier popular PPV type polymers such as MEH-PPV especially prone to chemical and light attack due the presence of a lone C=C bond and devices are typically degraded significantly in a matter of minutes to hours under  $1000\text{W/m}^2$  illumination in ambient atmosphere [14]. Poly-3-hexylthiophene (P3HT) is significantly more stable to light and can sustained up to several days, but devices based on this material are also susceptible to chemical degradation [14]. Polyfluorene Red is one of the most common stable polymer commercial materials with the slowest photo-degradation and photo-bleaching effect.

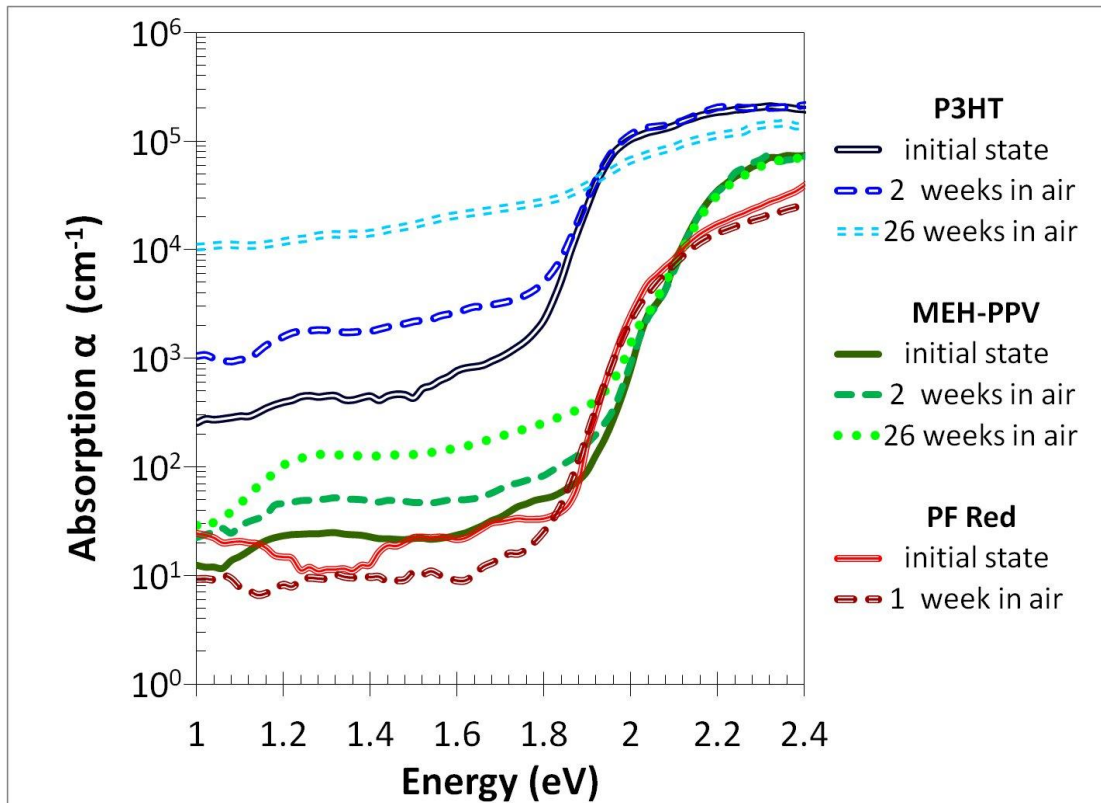


**Figure 5.8: Absorption vs. energy of P3HT (blue lines), MEH-PPV (green lines), and PF Red (red lines) in process of degradation in air without light exposure.**

However, comparison of these three polymers vulnerability to air degradation shows slightly different picture. When oxygen and water are present, their diffusion into the photovoltaic device is generally regarded as the dominant source of degradation. It is thus essential to gain more detailed knowledge of the mechanisms of oxygen effect into the PV devices. In the Figure 5.8 we compare degradation of MEH-PPV, P3HT, and PF Red in air at dark. Freshly annealed P3HT and MEH-PPV thin films were kept in the dark and measured by the PDS system before and after 2 weeks and 26 weeks of an air exposure. PF Red thin films were measured only after 1

week of the air exposure for evaluation purpose. The air exposure on its own causes significant increase in the trap density and no impact on the band gap energy of MEH-PPV. The origin of these traps is likely due to oxygen, which is known to be one of the main sources of MEH-PPV device degradation. Oxidation of the polymer leads to the formation of aromatic aldehyde, i.e., carbonyl which quenches the fluorescence and the concomitant chain scission results in reduced carrier mobility [22, 23]. Surprisingly, the P3HT film has the highest trap states level and is more sensitive to the oxygen than the MEH-PPV film. The reason to this air sensitivity is “crystalline order” of the materials. The two noncrystalline polymers, (MEH-PPV and PF Red) have intrinsically low trap states that are only weakly impacted by air. P3HT is regioregular polymer with more crystalline structure. As a result, P3HT has lower band gap, which makes it highly conjugated polymer, and higher trap states, which are more sensitive to air.

## **5.7. Conclusion**

Polymer solar cells are complicated multilayer structures where each component may fail for different reasons and layers may even interact chemically and physically in ways that may cause degradation. In our research the light, air, temperature contributors to the degradation mechanisms have been pin pointed. Oxygen from the atmosphere oxidizes the organic layer, especially when the device is illuminated.

During photo-oxidation in polymers deep traps are created, which causes slowed down of recombination. Air exposure alone degrades polymer films slowly, for many polymers this process is reversible by putting films back to vacuum. However, exposure to air and light together changes molecular structure of polymers, causes photobleaching, and increases the mid-gap trap states permanently. Encapsulation impedes the degradation process, but the currently available materials used for encapsulation of polymers do not remove the process completely. Even more complex encapsulation schemes, such as a sealed glass container or a high vacuum chamber, are employed the overall polymer device degradation is not eliminated completely [14].

## 5.8. References

- 1) C. Chang, M. Chen, and C. Chien, *J. Electrochem. Soc.* **158**, H854 (2011).
- 2) M. S. A. Abdou, F. P. Orfino, Z. W. Xie, M. J. Deen, and S. Holdcroft, *Adv. Mater.* **6**, 838 (1994).
- 3) M. S. A. Abdou, F. P. Orfino, Y. Son, and S. Holdcroft, *J. Am. Chem. Soc.* **119**, 4518 (1997).
- 4) E. J. Meijer, C. Detcheverry, P. J. Baesjou, E. van Veenendaal, D. M. de Leeuw, and T. M. Klapwijk, *J. Appl. Phys.* **93**, 4831 (2003).
- 5) A. M. A. Dias, R. P. Bonifarcio, I. M. Marrucho, y A. A. H. Pardua and M. F. Costa Gomes, *Phys. Chem. Chem. Phys.* **5**, 543 (2003).

- 6) L. Goris, K. Haenen, M. Nesládek, P. Wagner, D. Vanderzande, L. De Schepper, J. D'Haen, L. Lutsen, and J. V. Manca, *J. Mater. Sci.* **40**, 1413 (2005).
- 7) C. H. Seager, M. Sinclair, D. McBranch, A. J. Heeger, and G. L. Baker, *Synth. Metals* **49**, 91 (1992).
- 8) Y. Liu, L. Wu, P. T. Lai, and Q. Zuo, *Semicond. Sci. Tech.* **24**, 095013(2009).
- 9) U. Zhokhavets, T. Erb, G. Gobsch, M. Al-Ibrahim, and O. Ambacher, *Chem. Phys. Lett.* **418**, 347 (2006).
- 10) T. J. Savenije, J. E. Kroeze, X. Yang, and J. Loos, *Thin Solid Films* **511**, 2 (2006).
- 11) M. Jørgensen, K. Norrman, S. A. Gevorgyan, T. Tromholt, B. Andreasen, and F. C. Krebs, *Adv. Mater.* **24**, 580–612 (2012).
- 12) M. Manceau, A. Rivaton, J.-L. Gardette, S. Guillerez, N. Lemaitre, *Polym. Degrad. Stab.* **94** 898 (2009).
- 13) M. Manceau, S. Chambon, A. Rivaton, J.-L. Gardette, S. Guillerez, N. Lemaitre, *Sol. Energ. Mat. Sol. C.* **94** 1572 (2010).
- 14) M. Jørgensen, K. Norrman, F. C. Krebs, *Sol. Energ. Mat. Sol. C.* **92**, 686 (2008).
- 15) N. Ljungqvist, T. Hjertberg, *Macromol.* **28**, 5993 (1995).
- 16) M. L. Chabiny, R. A. Street, and J. E. Northrup, *Appl. Phys. Lett.* **90**, 123508 (2007).
- 17) R. Xia, G. Heliotis, and D. D. C. Bradley, *Synth. Metals* **140**, 117 (2004).
- 18) Q. Hou, Y. Xu, W. Yang, M. Yuan, J. Peng and Y. Cao, *J. Mater. Chem.* **12**, 2887 (2002).

- 19) V. N. Bliznyuk, S. A. Carter, J. C. Scott, G. Klairner, R. D. Miller, and D. C. Miller, *Macromolecules* **32**, 361 (1999).
- 20) C. Ego, D. Marsitzky, S. Becker, J. Zhang, A. C. Grimsdale, K. Mullen, J. D. MacKenzie, C. Silva, and R. H. Friend, *J. Am. Chem. Soc.* **125**, 437 (2003).
- 21) R. Grisorio, G. Allegretta, P. Mastrorilli, G. P. Suranna, *Macromol.* **44**, 7977 (2011).
- 22) J. C. Scott, J. H. Kaufman, P. J. Brock, R. DiPietro, J. Salem, and J. A. Goitia, *J. Appl. Phys.* **79**, 2745 (1996).
- 23) V. Kažukauskas, *Semicond. Sci. Tech.* **19** 1373 (2004).

# CHAPTER 6:

## CONCLUSION AND FINAL THOUGHTS



Figure 6.1: Solar energy cartoon by HSB-Cartoon.

The investigations presented in this dissertation have expanded the understanding of mid gap trap states effect in thin films. We have used the Photothermal Deflection Spectroscopy to measure and to analyze small changes in the band gap and the band tail absorption in three different types of thin films in the process of degradation.

We have discussed absorption changes in silicon thin films, the most common solar cell material. Crystallinity impact on microcrystalline silicon ( $\mu\text{c-Si}$ ) and micromorph films have been quantified as a percentage ratio of amorphous (a-Si) and pure crystalline silicon (c-Si). PDS measurements have confirmed that the Staebler-Wronski effect (SWE), the light-induced metastable changes in the properties of silicon, predominantly affected bulk states rather than surface states of a-Si films.

We have examined the effect of ligands and nanoparticle (NP) size on mid-gap trap states in NP thin films as it impacted on the performance during degradation. Thin film solar cells comprised of quantum-confined CdTe nanoparticles had a low intrinsic density of mid-gap trap states relative to their equivalent bulk film indicating that the ligands were effective at electrically passivating surface states. PbS quantum dots solar cells passivated with EDT ligands did not show any strong correlation between trap state density and the performance of the photovoltaics.

We have measured and analyzed several organic thin films degradation of mid-gap trap states in the process of photo-degradation and photo-oxidation. Air exposure degraded more crystalline P3HT films faster than noncrystalline polymers (MEH-PPV and polyfluorene Red), but this process were reversible by putting films

back to vacuum. During photo-oxidation, changes to the molecular structure of polymers and the increase of traps were permanent.

Finally, all three groups of the different solar cells have shown contradiction of the crucial importance of trap states in a device failure. We have demonstrated that the higher amount of trap states in the material do not necessarily mean poorer performance and stability of a solar cell. Typically during degradation the trap states increase and the photovoltaic efficiency decreases; however, for some materials, like NPs, the performance may decay or improve without any changes on the traps' level. In conclusion, we cannot blame traps as a main source of degradation of solar cells, since a material structure, crystallinity, a particle's deformation, and a polymer's decomposition may have much higher effect on the solar cell's stability and performance.